# REPUBLIC OF TURKEY YILDIZ TECHNICAL UNIVERSITY GRADUATE SCHOOL OF NATURAL AND APPLIED SCIENCES

# CROP CLASSIFICATION WITH POLARIMETRIC SYNTHETIC APERTURE RADAR IMAGES: COMPARATIVE ANALYSIS

# Mustafa ÜSTÜNER

DOCTOR OF PHILOSOPHY THESIS

Department of Geomatic Engineering

Program of Remote Sensing and GIS

Advisor Prof. Dr. Füsun BALIK ŞANLI

Co-Advisor Assoc. Prof. Dr. Gökhan BİLGİN

January, 2020

# REPUBLIC OF TURKEY YILDIZ TECHNICAL UNIVERSITY GRADUATE SCHOOL OF NATURAL AND APPLIED SCIENCES

# CROP CLASSIFICATION WITH POLARIMETRIC SYNTHETIC APERTURE RADAR IMAGES: COMPARATIVE ANALYSIS

A thesis submitted by Mustafa ÜSTÜNER in partial fulfillment of the requirements for the degree of **DOCTOR OF PHILOSOPHY** is approved by the committee on 13.01.2020 in Department of Geomatic Engineering, Program of Remote Sensing and GIS.

Prof. Dr. Füsun BALIK ŞANLI Yildiz Technical University Advisor Assoc. Prof. Dr. Gökhan BİLGİN Yildiz Technical University Co-Advisor

# Approved By the Examining Committee Prof. Dr. Füsun BALIK ŞANLI, Advisor Yildiz Technical University Assoc. Prof. Dr. Esra ERTEN, Member Istanbul Technical University Prof. Dr. Melih BAŞARANER, Member Yildiz Technical University Assoc. Prof. Dr. Saygın ABDİKAN, Member Zonguldak Bülent Ecevit University Prof. Dr. Naci YASTIKLI, Member Yıldız Technical University

I hereby declare that I have obtained the required legal permissions during data collection and exploitation procedures, that I have made the in-text citations and cited the references properly, that I haven't falsified and/or fabricated research data and results of the study and that I have abided by the principles of the scientific research and ethics during my Thesis Study under the title of Crop Classification with Polarimetric Synthetic Aperture Radar Images: Comparative Analysis supervised by my supervisor, Prof. Dr. Füsun BALIK ŞANLI. In the case of a discovery of false statement, I am to acknowledge any legal consequence.

Mustafa ÜSTÜNER

Signature





# **ACKNOWLEDGEMENTS**

This thesis would not have been possible without the help and support of countless individuals, to whom I am immensely grateful even if I can not name everyone here. First and foremost, I would like to express my deepest gratitude to my supervisors, Prof. Dr. Füsun Balık Şanlı, and my co-supervisor Assoc. Prof. Dr. Gökhan Bilgin for their constant help and long-standing support during my PhD.

Besides my advisors, I would like to thank to the rest of my thesis committee: Assoc. Prof. Dr. Esra Erten and Prof. Dr. Melih Başaraner, for their insightful comments.

My special thanks go to Assoc. Prof. Dr. Saygın Abdikan who always helped and supported my research, not just only for my PhD thesis but also for my MSc thesis.

Friends have a special place during this PhD journey. As expected, there are ups and downs in PhD and when something goes wrong, the first thing I did was to talk to my friends and got some advices from them. What more amazing is that they are always ready to listen you without any expectation or any personal benefits. I think this is one of greatest personal gains in my life. I would really appreciate to my friends Günsu Yılma Sakalar and Alper Sakalar for their close friendship and long-standing support. I also would like to thank Fatih Yavuz for becoming a true friend.

So many thanks to my friends and colleagues from the Department of Geomatic Engineering of Yildiz Technical University, who have a special place in this journey. At first, I would like thank to Dr. Mahmut Oguz Selbesoglu and Dr. Tolga Bakırman for their great friendship as well as long-standing support during my PhD. My special thanks also go to Yalçın Yılmaz, Seda Özarpacı and Muharrem Hilmi Erkoc for their great friendship as well as spending time with me especially in the writing period of my thesis. Your text message "tea is ready, come downstairs here!" was so motivating. I also would like to thank Ali Hasan Doğan, Dr. Utkan Mustafa Durdağ and Batuhan Kılıç for their friendship. The times we spent together motivated me to come to the end of this journey.

I got an opportunity to be a visiting scholar in Friedrich Schiller University of Jena (FSU Jena), Germany in 2018 with the support of TUBITAK 2214-A International Doctoral

Research Fellowship Programme. I was so lucky to meet friendly people and colleagues in FSU Jena. I would like to thank to whole team members of the Department of Earth observation (Lehrstuhl für Fernerkundung) in FSU, particularly Prof. Dr. Christiane Schmullius, Dr. Nesrin Salepci, Dr. Christian Berger, Dr. Felix Cremer, Dr. John Truckenbrodt and Martyna Stelmaszczuk-Gorska for their support and making my stay in Jena great. Also special thanks go to Zlatomir Dimitrov and Franziska Zander for their friendship during my stay in Jena. We should revisit the "Fritz Mitte" in Jena and eat "pommes" together.

Also during my PhD, I received the great help and recommendations from my friends and colleagues especially from the academic point of view. Special thanks go to Dr. Vahid Akbari (Norwegian Institute of Bioeconomy Research) and Dr. Shaunak De (Orbital Sight) for being so kind to answer my questions about SAR Polarimetry. Also I would like to thank Dr. Carlos Lopez Martinez (Universitat Politecnica de Catalunya), Dr. Pedram Ghamisi (Helmholtz-Zentrum Dresden-Rossendorf) and Dr. Saeid Homayouni (INRS-Quebec) for their helps and support.

Becoming a member of the professional societies as well as serving for them helped me to expand my academic network and environment. In the last two years of my PhD, I got an opportunity to join the IEEE Geoscience and Remote Sensing Society (IEEE GRSS). My special thanks go to Dr. Mariko S. Burgin (NASA JPL), Dr. Sidharth Misra (NASA JPL) and Prof. Dr. Steven C. Reising (Colorado State University) for introducing me the IEEE GRSS and allowing me to serve as the social media ambassador for the society. I have been also serving as the social media coordinator for ISPRS (International Society for Photogrammetry and Remote Sensing) Student Consortium. I would like to thank ISPRS for allowing me an opportunity for serving the society, particularly Sheryl Rose Reyes (United Nations University) and Prof. Dr. Charles Toth (Ohio State University).

Last but not least, I would like to express my deepest gratitude to my family (my parents and brother) and friends. This thesis would not have been possible without their warm love, continued patience, and endless support.

Mustafa ÜSTÜNER

# TABLE OF CONTENTS

LI	ST O	F SYME	BOLS	ix
LI	ST O	F ABBR	REVIATIONS	xi
LI	ST O	F FIGU	RES	xiii
LI	ST O	F TABL	ES	xv
Αŀ	3STR	ACT		xvi
Ö	ZET			xviii
1	Intr	oductio	on	1
	1.1	Litera	ture Review	2
	1.2	Object	tive of the Thesis	6
	1.3	-	hesis	7
	1.4		ture of the Thesis	8
2	RAD	OAR Re	mote Sensing	9
	2.1	SAR R	Remote Sensing	11
	2.2	Polari	metric SAR	15
	2.3	Polari	metric Target Decompositions	17
		2.3.1	Eigenvector based decomposition	18
		2.3.2	Model based decomposition	21
3	Clas		ion and Accuracy Metrics	24
	3.1	Image	Classification	24
		3.1.1	Support Vector Machines	27
		3.1.2	Random Forest	29
		3.1.3	Light Gradient Boosting Machines	30
	3.2	Accur	acy Measures	32
		3.2.1	Overall Accuracy and Kappa Coefficient	32
		3.2.2	McNemar's test	33
		3 2 3	K-Fold Cross Validation	34

4	Exp	erimental Design	35
	4.1	Study Area and Data set	35
	4.2	Experimental Design and Data Analysis	37
		4.2.1 Data Pre-Processing	37
		4.2.2 Data Classification	38
		4.2.3 Parameter Tuning for Classification Models	39
5	Rest	ılts And Discussion	42
	5.1	Temporal Analysis of Features for Crop	42
	5.2	Classification Results	49
	5.3	Evaluation of Computational Costs	54
	5.4	F-scores for per model	55
	5.5	Class-based Accuracy Assessment	56
		5.5.1 Alfalfa	56
		5.5.2 Maize	58
		5.5.3 Potato	58
		5.5.4 Sunflower	59
		5.5.5 Wheat	61
	5.6	Conclusion	62
Re	feren	aces	64
Α	App	endix 1	72
В	App	endix 2	80
D <sub>11</sub>	hlica	tions From the Thesis	ጸጸ

# LIST OF SYMBOLS

Alpha Angle  $\alpha_{i}$  $\delta_a$ **Azimuth Resolution** Α Anisotropy Bragg Scattering Coefficients Perpendicular to the incident plane  $R_s$ Bragg Scattering Coefficients Parallel to the incident plane  $R_p$ Class label  $\mathbf{X}_{i}$ Т **Coherency Matrix Complex Basis Matrices** Ψ **Complex Scattering Matrix** S C **Covariance Matrix Depression Angle**  $\theta_d$ Diagonal Eigenvalue Matrix with Elements of Nonnegative Λ Eigenvalues **Dihedral Scattering**  $f_d$ b Distance of hyperplane from the origin point Eigenvalue  $\lambda_i$ Eigenvector  $\vec{\epsilon}_i$ Η Entropy  $R_r$ **Ground-Range Resolution** Н Higher Dimensional Feature Space  $R_{sh}$ Horizontal Fresnel coefficients for the soil Horizontal Fresnel coefficients for the trunk  $R_{th}$ K Kennaugh Matrix  $\mathbf{K}(x_i, x_j)$ **Kernel Function** 

γ	Kernel Width
$d_a$	Length of Antenna
$oldsymbol{\Psi}_L$	Lexicographic Vectorization
α	Mean Alpha Angle
Φ	Nonlinear Mapping Functions
q	Number of Classes
N	Number of Samples
T	Number of Trees
$R^n$	n-dimensional vector
$oldsymbol{\Psi}_{P}$	Pauli Vectorization
τ	Pulse Duration
b	Real Ratio
$f_d$	Scattering Amplitude in Dihedral Scattering
$P_d$	Scattering Power for Dihedral Scattering
$P_s$	Scattering Power for Surface Scattering
$P_{ u}$	Scattering Power for Volume Scattering
ξ	Slack Variable
c	Speed of Light
$f_s$	Surface Scattering
k	Target Vector
$\mathbf{x}_i$	Training Sample
$\mathbf{k}_{\!\scriptscriptstyle L}$	Target Vector in Lexicographic Basis
$\mathbf{k}_{p}$	Target Vector in Pauli Basis
m	Total Number of Reference Pixels
[U]	Unitary Eigenvector Matrix
$R_{sv}$	Vertical Fresnel coefficients for the soil
$R_{tv}$	Vertical Fresnel coefficients for the trunk
$f_{ u}$	Volume Scattering

# LIST OF ABBREVIATIONS

ANN Artificial Neural Network

BBCH Biologische Bundesanstalt, Bundessortenamt, and CHemische

CCF Canonical Correlation Forest

DT Decision Trees

EFB Exclusive Feature Bundling

ESA European Space Agency

GBDT Gradient Boosting Decision Tree

GOSS Gradient-based One-Side Sampling

HH Horizontal Horizontal

HV Horizontal Vertical

LightGBM Light Gradient Boosting Machine

MLC Maximum Likelihood Classification

MLP Multilayer Perceptron

NASA National Aeronautics and Space Administration

NNED Non-negative Eigenvalue Decomposition

PA Producer's Accuracy

PolSAR Polarimetric Synthetic Aperture Radar

RBF Radial Basis Function

RF Random Forest

RoF Rotation Forest

SAR Synthetic Aperture Radar

SLAR Side-looking Airborne Radar

SNAP Sentinels Application Platform

SRTM Shuttle Radar Topography Mission

SVM Support Vector Machine

UA User's Accuracy

UAVSAR Uninhabited Aerial Vehicle Synthetic Aperture Radar

VH Vertical Horizontal

VV Vertical Vertical

XGBoost Extreme Gradient Boosting

# LIST OF FIGURES

Figure 2.1	How radar systems works [28]	10
Figure 2.2	Side-looking airborne SAR geometry [29]	10
Figure 2.3	Ground and Slant Range [27]	12
Figure 2.4	Vertical and Horizontal Polarizations [34]	15
Figure 3.1	5-Fold cross validation	34
Figure 4.1	Study Area	36
Figure 4.2	Multi-temporal Images	36
Figure 4.3	Data Pre-Processing	37
Figure 4.4	Ground Truth Data	38
Figure 4.5	Data Processing	41
Figure 5.1	Temporal Changes in Entropy	42
Figure 5.2	Temporal Changes in Anisotropy	43
Figure 5.3	Temporal Changes in Alpha Angle	44
Figure 5.4	Temporal Changes in HH Polarization	45
Figure 5.5	Temporal Changes in HV Polarization	45
Figure 5.6	Temporal Changes in VV Polarization	46
Figure 5.7	Temporal Changes in Surface Scattering	47
Figure 5.8	Temporal Changes in Double Bounce Scattering	48
Figure 5.9	Temporal Changes in Volume Scattering	49
Figure 5.10	Overall Accuracy	50
Figure 5.11	Accuracies with Standart Deviation	51
Figure 5.12	Kappa Coefficients	52
Figure 5.13	Kappa Coefficients with Standart Deviations	53
Figure 5.14	F-scores for LightGBM	55
Figure 5.15	F-scores for RF	55
Figure 5.16	F-scores for SVM	56
Figure 5.17	'F-scores for Alfalfa	57
Figure 5.18	F-scores for Maize	59
Figure 5.19	F-scores for Potato	60
Figure 5.20	F-scores for Sunflower	60
Figure 5.21	F-scores for Wheat	61

Figure	B.1	Classified Image of Cloude-Pottier and LightGBM	80
Figure	<b>B.2</b>	Classified Image of Cloude-Pottier and RF	81
Figure	B.3	Classified Image of Cloude-Pottier and SVM	81
Figure	B.4	Classified Image of Coherency Matrix and LightGBM	82
Figure	B.5	Classified Image of Coherency Matrix and RF	82
Figure	B.6	Classified Image of Coherency Matrix and SVM	83
Figure	B.7	Classified Image of Freeman-Durden Decomposition and LightGBM	83
Figure	B.8	Classified Image of Freeman-Durden Decomposition and RF	84
Figure	B.9	Classified Image of Freeman-Durden Decomposition and SVM	84
Figure	B.10	Classified Image of Linear Polarizations and LightGBM	85
Figure	B.11	Classified Image of Linear Polarizations and RF	85
Figure	B.12	Classified Image of Linear Polarizations and SVM	86
Figure	B.13	Classified Image of Van Zyl Decomposition and LightGBM	86
Figure	B.14	Classified Image of Van Zyl Decomposition and RF	87
Figure	B.15	Classified Image of Van Zyl Decomposition and SVM	87

# LIST OF TABLES

Table 1.1	Research Studies that use of L-Band	3
Table 1.2	Research Studies that use of C-Band	5
Table 2.1	Common bands and their wavelength ranges	13
Table 3.1	LightGBM Parameters	31
Table 3.2	An error matrix with four classes	32
Table 3.3	$2 \times 2$ confusion matrix and elements in equation 3.16	33
Table 4.1	Specification of RADARSAT-2 image	35
Table 4.2	Ground Truth (Reference) Data	38
Table 4.3	Ground Truth (Reference) Data	39
Table 4.4	LightGBM Parameters	39
Table 5.1	McNemar's Test ( $\chi^2$ ) values	50
Table 5.2	McNemar's Test ( $\chi^2$ ) values	52
Table 5.3	Computer Specifications	54
Table 5.4	CPU running times for training process (in seconds)	54
Table A.1	Normalized Confusion Matrices for LightGBM	73
Table A.2	Normalized Confusion Matrices for RF	74
Table A.3	Normalized Confusion Matrices for SVM	75
Table A.4	McNemar's test results for Coherency Matrix	76
Table A.5	McNemar's test results for Linear Polarizations	76
Table A.6	McNemar's test results for Cloude-Pottier Decomposition	76
Table A.7	McNemar's test results for Freeman-Durden Decomposition	76
Table A.8	McNemar's test results for Van Zyl Decomposition	76
Table A.9	Overall accuracy with standart deviation	77
Table A.10	Kappa Coefficients with standart deviation	77
Table A.11	F-scores for Alfalfa	78
Table A.12	Pr-scores for Maize	78
Table A.13	F-scores for Potato	78
Table A.14	F-scores for Sunflower	79
Table A 15	F-scores for Wheat	79

# **Crop Classification with Polarimetric Synthetic Aperture Radar Images: Comparative Analysis**

Mustafa ÜSTÜNER

Department of Geomatic Engineering

Doctor of Philosophy Thesis

Advisor: Prof. Dr. Füsun BALIK ŞANLI Co-advisor: Assoc. Prof. Dr. Gökhan BİLGİN

Polarimetric Synthetic Aperture Radar (PolSAR) images could provide beneficial information regarding the complete scattering about the objects or targets and this could be advantageous to derive the physical and geometrical structure. Due to the benefits of the imaging capability day/night and weather-independent, Synthetic Aperture Radar (SAR) sensors are of vital importance for time-critical practices, especially in agricultural applications. In specific to agricultural practices, multi-temporal or time series data is a pre-requisite for timely monitoring or identification of crop pattern. This is because crops have a dynamically changing structure in temporal domain. Each crop has different structural and physical changes in temporal domain and the use of multi-temporal data leads to better separation of crops.

The PolSAR data by itself (2×2 complex Sinclair scattering matrix) do not explicitly/directly provide the "ready-to-use" information about the three elementary scattering (surface, double bounce and volume scattering) for natural targets and the data needs to be converted to second order statistical formalism (3×3 complex matrices) for extracting the scattering properties. In such a case, polarimetric decomposition methods can be used to extract the three elementary scattering for the targets precisely.

In this thesis, the comparative performance of the original features (linear polarizations and coherency matrix) and polarimetric features (incoherent

polarimetric decompositions) from multi-temporal PolSAR data was investigated for crop pattern identification through three different machine learning algorithms (Light Gradient Boosting Machine, Support Vector Machine and Random Forest). In order to create the polarimetric features, three different incoherent polarimetric decompositions were utilized as follows: Cloude-Pottier decomposition (eigenvector-based), Freeman-Durden decomposition (model-based) and Van Zyl (hybrid) decomposition. Among these machine learning algorithms, Light Gradient Boosting Machines was recently introduced to machine learning community and have not been much explored in remote sensing for classification purposes.

The experimental results demonstrated that highest classification accuracy (0.96) were received by Van Zyl decomposition as well as Freeman-Durden through LightGBM. The results also addressed that LightGBM is much faster (almost ten times) than RF and SVM for linear polarizations, coherency matrix and Cloude-Pottier decomposition.

This thesis also highlights the benefits of model-based and hybrid decompositions about obtaining the higher performance in comparison to original features for crop pattern classification.

**Keywords:** Polarimetric decompositions, PolSAR, Light gradient boosting machines, crop classification, machine learning

# Polarimetrik Sentetik Açıklıklı Radar Görüntüleri ile Ürün Deseni Sınıflandırması: Karşılaştırmalı Analiz

Mustafa ÜSTÜNER

Harita Mühendisliği Anabilim Dalı Doktora Tezi

Danışman: Prof. Dr. Füsun BALIK ŞANLI Eş-Danışman: Doç. Dr. Gökhan Bilgin

Polarimetrik SAR görüntüleri, hedef objelerin tam saçılımlarına ilişkin faydalı bilgiler içermektedir ve bu bilgiler de hedef objelerin fiziksel ve geometric yapılarına ilişkin bilgi elde etme noktasında önemli avantajlar sağlamaktadır. İklim koşullarından bağımsız ve gece/gündüz olarak yeryüzünü görüntüleyebilme özelliği nedeniyle SAR görüntüleri, özellikle zamansal izlemenin kritik derecede önemli olduğu çalışmalarda büyük öneme sahiptir. Tarım uygulamaları özelinde bakıldığında ise, ürün dokusunun/deseninin belirlenmesinde çok zamanlı görüntülerin kullanımı zorunlu olmaktadır. Bu zorunluluğun nedeni ise, tarımsal ürünlerin kısa zaman aralığında dinamik bir yapısal değişiklik göstermesidir. Her bir tarım ürünü aynı zaman frekansında farklı büyüme göstereceğinden bu farklılık ürünlerin birbirinden daha iyi ayrılmasını sağlayacaktır.

PolSAR datasının 2×2 lik saçılım matrisi, doğal kaynaklara ilişkin üç temel saçılım bilgisini direkt olarak sunmamaktadır ve PolSAR verisi ikinci dereceden istatistiksel dönüşüm aracılığı ile elde edilen 3×3 lük koherens yada kovaryans matrislerine dönüştürülmelidir. Böyle bir durumda, üç temel saçılımın elde edilmesinde polarimetrik ayrıştırma teknikleri kullanılmaktadır.

Bu tez çalışmasında, çok zamanlı PolSAR verisinden üretilen orijinal ve polarimetrik özelliklerin ürün dokusu tespitindeki karşılaştırmalı performans analizi üç farklı makine öğrenme algoritmasından faydalanarak yapılmıştır. Polarimetrik özelliklerin üretilmesi aşamasında, üç farklı koherent olmayan polarimetrik ayrıştırma tekniği

kullanılmıştır (Cloude-Pottier decomposition, Freeman-Durden ve Van Zyl (hybrid) ayrıştırma teknikleri). Çalışma kapsamında kullanılan LightGBM yöntemi ise, yeni bir yöntem olup uzaktan algılama çalışmalarındaki kullanımı az sayıdadır.

Deneysel sonuçlar, en yüksek sınıflandırma doğruluğunun (0.96) LightGBM sınıflandırma yönteminden faydalanarak Van Zyl ve aynı zamanda Freeman-Durden polarimetrik ayrıştırma teknikleri ile elde edildiğini göstermiştir. İşlem süresi açısından ise, LightGBM yönteminin doğrusal polarizasyon, koherens matrisi ve Cloude-Pottier polarimetrik ayrıştırma tekniklerinin sınıflandırılması işlemlerinde, DVM ve RO algoritmalarına kıyasla 10 kat daha hızlı olduğu görülmüştür.

Bu tez çalışması, ürün dokusunun sınıflandırılmasında model tabanlı ve hybrid ayrıştırma teknikleri ile, PolSAR verisinin orijinal özelliklerine kıyasla daha yüksek sınıflandırma doğruluğu elde edilebileceği sonucuna varmıştır.

**Anahtar Kelimeler:** Polarimetrik ayrıştırma, PolSAR, Hafif gradyan hızlandırma makineleri, tarımsal ürün sınıflandırma, makine öğrenmesi

YILDIZ TEKNİK ÜNİVERSİTESİ FEN BİLİMLERİ ENSTİTÜSÜ

# 1 Introduction

Remote sensing has a great capability of observing the land in a wide-range coverage along with a short temporal scale [1]. The mapping and monitoring of the cropland play an essential role for many agricultural and economical practices in the regional and global activities. Crops have spatially and temporally dynamic changes in a short time period and therefore the systematic and timely monitoring is required to obtain proper information [2, 3]. In this particular case, optical sensors might be of not practical because it is not always possible to obtain "cloud-free" images therefore it can not be of useful for time-critical agricultural practices. In this case, the use of synthetic aperture radar (SAR) images could be a solution for such time-critical agricultural applications with the advantage of day/night and weather-independent imaging [2, 4–6]. Radar signal (radar backscatter) is sensitive to the crop dielectric properties, structural attributes (shape, size and orientation) and the phenological changes [7– 9]. When it's considered from that point, Polarimetric SAR (PolSAR) images provide richer and more detailed information compared to single or dual polarization as radar backscatter is polarization dependent[7, 9, 10]. With this purpose, full polarimetric space-borne SAR sensor are widely used such as RADARSAT-2 (C band), ALOS-2 (L band) and GF-3 (C band) for crop mapping and monitoring.

Natural targets such as forest, crops and vegetation are considered as distributed or incoherent scatterers and have a random scattering. Such targets can be modelled through second-order formalism [7, 11, 12]. For seperating the complex scattering mechanism for incoherent scatterers into several scattering elements, polarimetric target decompositions are widely used [12, 13]. In the case of crop classification, incoherent target decompositions were employed since agricultural lands have random scattering. Incoherent target decomposition can be separated into two parts: eigenvector-based (mathematical) decompositions and model-based (physical) decompositions [7, 10]. More details about the polarimetric target decompositions (Cloude-Pottier, Freeman-Durden and Van Zyl) are provided in Chapter 2.

The multi-temporal datasets for crop classification are usually preferred in order to

improve the classification performance since the phenological changes of each crop in temporal domain are different than others, especially in their growing season. These temporal changes lead to better discrimination of crop types. Therefore, multi-temporal datasets are more powerful than single-date images to discriminate the crop types [2, 4, 5]. This undisputed outperformance of multitemporal versus monotemporal within PolSAR data for crop classification was proven in many studies such as [2], [14] and [5].

In this thesis, the original and polarimetric features from multitemporal RADARSAT-2 data were evaluated in crop classification using three supervised machine learning algorithms, namely LightGBM, RF and SVM. The classification results were obtained through k-fold cross validation. Also, the significance test was utilized to analyse the differences between two classifier accuracy through McNemar's test. The following subsections present the literature review, the objective of the thesis, hypothesis and, lastly the structure of the thesis.

### 1.1 Literature Review

In this section, the research studies employing at least one polarimetric target decompositions along with original or polarimetric features for the crop (crop dominated classes) classification from PolSAR data are only reviewed. The most common used bands for crop classification in PolSAR are C or L bands, therefore only research studies that employed of L (Table 1.1) and C (Table 1.2) band were reviewed here.

McNairn et al.(2009) tested the classification performances of Cloude-Pottier, Freeman-Durden and Krogager target decomposition in addition to linear polarizations from L-band ALOS PALSAR data for the classification of crops. In their experimental results addressed the outperformance of target decomposition in comparison with linear polarizations within overall classification accuracy [15].

Tamiminia et al.(2017) used the multi-temporal L-band UAVSAR data for the classification of crops by the kernel based C-means clustering algorithm. In terms of the polarimetric features, they utilize linear polarizations and three different model-based target decompositions which are Cloude-Pottier, Freeman-Durden and Yamaguchi. Their results proved that polarimetric features help in better discrimination and classification of the crops [8].

Whelen and Siqueira (2017) investigated the potential of linear backscatters and Cloude-Pottier decompositions for crop classification from the time series of L-band UAVSAR data. Based on their experimental results, two of the polarimetric features of Cloude-Pottier decomposition (alpha and entropy) achieved higher accuracy in comparison to linear polarization for time-series classification [16].

Hariharan et al.(2018) analysed the polarimetric features of the covariance matrix and two different polarimetric decompositions (Cloude-Pottier and Touzi decompositions) extracted from the L-band AgriSAR-2006 campaign data. They proposed a new feature selection method. They concluded that the polarimetric parameters obtained from the target decomposition is vital for the discrimination of crops [17].

Khosravi and Alavipanah (2019) employed the textural, polarimetric and spectral features from optical (RapidEye) and PolSAR (L-band UAVSAR) data for crop mapping using random forest classification. As the polarimetric as well as original features from PolSAR data, they utilized the linear and circular polarizations, the eigenvalues of coherency matrix, coherent (Pauli and Krogager) and incoherent (Freeman-Durden and Yamaguchi) decompositions [18].

**Table 1.1** Research Studies that use of L-Band

	Input Features		Classifier	
Study	Original Features	Polarimetric Features	Method	
		Freeman-Durden	MLC,	
McNairn et al.(2009)	Linear Polarizations	Cloude-Pottier	ANN,	
		Krogager	DT	
		Freeman-Durden	Kernel	
Tamiminia et al.(2017)	Linear Polarizations	Cloude-Pottier	based	
		Yamaguchi	clustering	
Whelen & Siqueira (2017)	Linear Polarizations	Cloude-Pottier		
Hariharan et al.(2018)	Linear Polarizations	Cloude-Pottier	RF	
Translati et al.(2016)	Covariance Matrix	Touzi		
	Linear Polarizations	Freeman-Durden		
Whospari & Alazinanah (2010)	Circular Polarizations	Yamaguchi	RF	
Khosravi & Alavipanah(2019)		Pauli		
	Coherency Matrix	Krogager		
Li et al.(2019)	Linear Polarizations	Freeman-Durden	SVM,	
Li et ai.(2019)	Linear Foldrizations	Cloude-Pottier	MLP(ANN)	

Li et al.(2019) evaluated the linear polarizations and the polarimetric features of Cloude-Pottier and Freeman-Durden target decompositions for the classification and monitoring of crops using multitemporal L-band UAVSAR. Their results suggest that decomposed parameters produced higher accuracy compared to linear polarizations [19].

When Table 1.1 was examined, only Khosravi & Alavipanah (2019) used both linear polarizations and coherency matrix as the original features along with polarimetric features for crop classification from PolSAR data. However they did not explore the potential of Van Zyl and Cloude-Pottier decompositions for crop classification from PolSAR data and did not compare the classification performance of RF with other machine learning classifier

Li et al.(2012) employed Freeman Durden, Cloude Pottier, and Touzi decompositions for rice mapping and monitoring by using multitemporal RADARSAT-2 PolSAR images. Their results concluded that Touzi decomposition produced the highest accuracy for the classification of rice [20].

Ma et al.(2013) used the polarimetric parameters derived from three different target decomposition (Pauli, Freeman-Durden, and H/Alpha/Anisotropy) from RADARSAT-2 data for classification of crops. They concluded that multi-temporal RADARSAT-2 PolSAR Data is suitable for accurate mapping of crops [21].

Jiao et al.(2014) assessed the potential of linear intensity backscatters and polarimetric parameters extracted from Freeman-Durden and Cloude-Pottier decompositions for crop mapping and monitoring by using an object-oriented classification. Their results demonstrated that using the polarimetric parameters of Cloude–Pottier decomposition provided higher accuracy than linear backscatters and Freeman-Durden decomposition parameters [5].

Zeyada et al.(2016) tested the single-date PolSAR imagery for the classification of four different crops by three different supervised classification models. They used the polarimetric parameters obtained from Pauli, Cloude–Pottier, and Freeman–Durden decompositions along with linear backscatter coefficients. They founded that highest classification accuracy is obtained by SVM and stacking all the polarimetric parameters generated in their experiment [22].

Srikanth et al.(2016) compared the polarimetric decompositions (Pauli, Krogager, Freeman-Durden, Yamaguchi and Van Zyl) for crop classification by using three Radarsat-2 PolSAR data. In their experimental results, Krogager polarimetric decomposition receives higher accuracy than other decomposition methods [23].

Liao et al.(2018) explored the a total of 15 RADARSAT-2 images for crop classification using random forest and polarimetric features. In their experiment, linear

polarizations (HH, HV and VV) and polarimetric features from Pauli, Cloude–Pottier and Freeman–Durden decompositions were extracted and used in classification step as input data. Their results demonstrated that the highest classification accuracy was obtained by the coherency matrix, followed by the covariance matrix [14].

Shuai et al.(2019) used the polarimetric features from the polarimetric decomposition methods (Pauli and Cloude-Pottier) for maize mapping using the optical imagery-based segmentation [24].

Table 1.2 Research Studies that use of C-Band

	Input Features		Classifier
Study	Original Features	Polarimetric Features	Method
Li et al.(2012)	Linear Polarizations	Freeman-Durden Cloude-Pottier Touzi	SVM
Ma et al.(2013)	Coherency Matrix	Freeman-Durden Cloude-Pottier Pauli	MLC
Jiao et al.(2014)	Linear Polarizations	Freeman-Durden Cloude-Pottier	Object-based classification
Zeyada et al.(2016)	Linear Polarizations	Freeman-Durden Cloude-Pottier Pauli	SVM, MLP(ANN), DT
Srikanth et al.(2016)		Freeman-Durden Krogager Van Zyl Yamaguchi	Supervised parallelepiped minimum distance classification
Liao et al.(2018)	Linear Polarizations Coherency Matrix Covariance Matrix	Freeman-Durden Cloude-Pottier Pauli	RF
Shuai et al.(2019)	Linear Polarizations	Cloude-Pottier Pauli	Object-based SVM
Xie et al.(2019)		Neumann Cloude-Pottier	RF
This thesis	Linear Polarizations Coherency Matrix	Freeman-Durden Cloude-Pottier Van Zyl	LightGBM, RF, SVM

Xie et al.(2019) compared the classification performance of Neumann decomposition and Cloude–Pottier decomposition for crop classification using a time series of RADARSAT-2 SAR images. They used random forest classification for the classification of crops. Their experimental research concluded that Neumann decomposition demonstrated better classification performance compared to Cloude–Pottier decomposition [9].

When Table 1.2 was examined, only Liao et al.(2018) used both linear polarizations and coherency matrix together as the original features along with polarimetric features for crop classification from RADARSAT-2 data. However they did not investigate the potential of Van Zyl decomposition for crop classification from PolSAR data and did not compare the classification performance of RF with other machine learning classifier.

What distinguish this thesis work from those exists in the literature listed above mainly three issues:

- LightGBM was used first time for crop classification except [25].
- Van Zyl decomposition (a hybrid decomposition) was compared with Cloude-Pottier decomposition and Coherency matrix in terms of classification performance.
- LightGBM was compared with SVM and RF in terms of accuracy and computational cost for crop classification.

## 1.2 Objective of the Thesis

Full PolSAR sensors, by their characteristics, are able to record complete scattering for the objects and these complete scattering have a complex mechanism. The original features of PolSAR images could provide backscatter information about the objects however cannot fully provide the proper or categorized information regarding their scattering types. The natural or man-made objects could have different types of scattering such as surface scattering or dihedral scattering.

In order to comprehensive understanding and simpler interpretation for scattering of the target, polarimetric target decompositions are utilized for PolSAR images. Among these polarimetric decompositions, there are several approaches available to explore the hidden information in terms of different scattering for the object. Some of these approaches are mathematical-based (i.e. eigenvector-eigenvalue analysis) and some others are physical based (i.e. model based). Either method has various functionalities and therefore provides different information for the clearer understanding of the complex scattering mechanism regarding objects.

Specific to agricultural practices, crops have dynamic growing structure and different physical/dielectric properties in the temporal domain. These dynamics hence lead to have them different scattering since crops grow and change. In such cases, the use of multi-temporal data is a requisite to fully model and understand the crop structure and their scattering characteristics.

In this thesis work, original features (linear polarizations and coherency matrix) and polarimetric features (three incoherent decompositions) were exploited for crop classification and the use of PolSAR data for crop classification was investigated through three different machine learning algorithms (LightGBM, RF and SVM).

The objectives of the thesis could be listed as following:

- To compare the performance of original features vs polarimetric features for crop classification in terms of overall accuracy and computational efficiency.
- To assess the polarimetric decomposition techniques and intercompare their performance for crop classification (eigenvector-based vs model-based decomposition).
- To assess the original features and intercompare their performance for crop classification (linear polarizations vs coherency matrix).
- To explore/understand the LightGBM, the new ensemble learning method, for the classification of PolSAR data and compare their performance with two well-known and widely used machine learning algorithms in terms of classification accuracy and computational costs.
- To analyze how one crop type behaves in temporal domain and how much be distinguished from others based on the selection of features (class-based accuracy analysis).

# 1.3 Hypothesis

Crops have complex scattering mechanism and dynamic structural changes in temporal domain therefore it needs to be properly analyzed in terms of what type of polarimetric information need to be extracted for proper analysis. Polarimetric target decomposition can be of help in that case for better understanding the scattering of crops and this might lead to more accurate classification for crops in terms of accuracy and computation time. In this sense, polarimetric decomposition (i.e. polarimetric features) might produce higher accuracy than original features of PolSAR data for crop classification.

From the point of data classification in machine learning, there are several techniques that have been explored so far in remote sensing however still there is not any "commonly-held" single method or approach that could always outperform others, which is known as no free lunch theorem in machine learning. This is because the

data classification in remote sensing is a complex decision making process and rely on several factors such as training/testing data distribution, proper representativeness of land covers in signature data, resolution of imagery and the landscape heterogeneity. Ensemble learning algorithms fuse the decisions of single classifiers to produce the more accurate classification through majority voting approach.

Recently, the novel ensemble learning algorithms (i.e. multiple classifiers) such as LightGBM, XGBoost or canonical correlation forest (CCF) were introduced into the machine learning/data science community with new ideas to overcome the problems raised by single classifiers as well as to produce higher classification accuracy. LightGBM among the recently proposed ensemble learning algorithms attracted many researcher in machine learning because it's lower memory usage and fast training speed. When we consider these functionalities of LightGBM, this new ensemble learning algorithms could be a promising method for crop classification and could show greater performance compared to RF and SVM in terms of classification accuracy and computational cost.

### 1.4 Structure of the Thesis

This thesis is structured as follows:

- The basic introduction to SAR and PolSAR is given in Chapter 2 and subsequently the general overview for the polarimetric decompositions (target decomposition) are introduced.
- In Chapter 3, an overview for the classification algorithms used in remote sensing is provided. The recently developed ensemble learning algorithms are reviewed for the studies in remote sensing and subsequently the summary for the classification methods employed in thesis are provided in the subsections of Chapter 3. Furthermore, the accuracy measures are introduced.
- Chapter 4 presents the study area, data set and experimental design for data processing and analysis.
- And finally, Chapter 5 contains experimental results and corresponding discussions of this thesis.

# 2

# **RADAR Remote Sensing**

There are two types of sensing systems available in remote sensing, which are passive and active remote sensing systems. Passive remote sensing systems need sun's energy to record the electromagnetic energy reflected (e.g., visible spectrum) or emitted (thermal infrared) from the object. Passive remote sensing systems could only operate and provide imagery of earth surface when sun illuminate the Earth surface. Active remote sensing systems work independent of any external energy source (e.g., sun's energy) as these sensors provide their own source of energy (or electromagnetic energy) to measure the objects. In terms of remote sensing, most commonly used active sensors include: 1) radar, 2) lidar and 3) sonar as these terms are the acronyms for "radio detection and ranging", "light detection and ranging" and "sound navigation and ranging", respectively. Among of these three active sensors, radars are the most widely used for observing the Earth. Lidar and sonar could be particularly useful for mapping applications (i.e., topographic and bathymetric mapping) as compared to radars [26]

As it can be understood from the acronyms of radar, it was primarily designed for detecting the objects and determine their distance by using radio waves. Radar signals penetrate the cloud/rain under all weather conditions and hence radar systems provide the all-weather and day or night images of earth surface. Radar system transmits the electromagnetic (radio) signals (short bursts or pulses) towards to the target and receives the echoes from the object to measure the distance (or range) to an object [27, 28]. An example of how radar signal returns (echoes) from a house and a tree can be represented in Figure 2.1

The fundamental principles of the image acquisition for a radar system and an optical sensor are quite different. The main differences are the imaging geometry and electrical/physical properties (i.e., permittivity, roughness) of the object depending on the electromagnetic energy. Radars have the side-looking imaging geometry while optical sensors have nadir-viewing geometry to acquire images. In the side-looking imaging geometry, flight direction (or along-track) is defined as "azimuth direction"

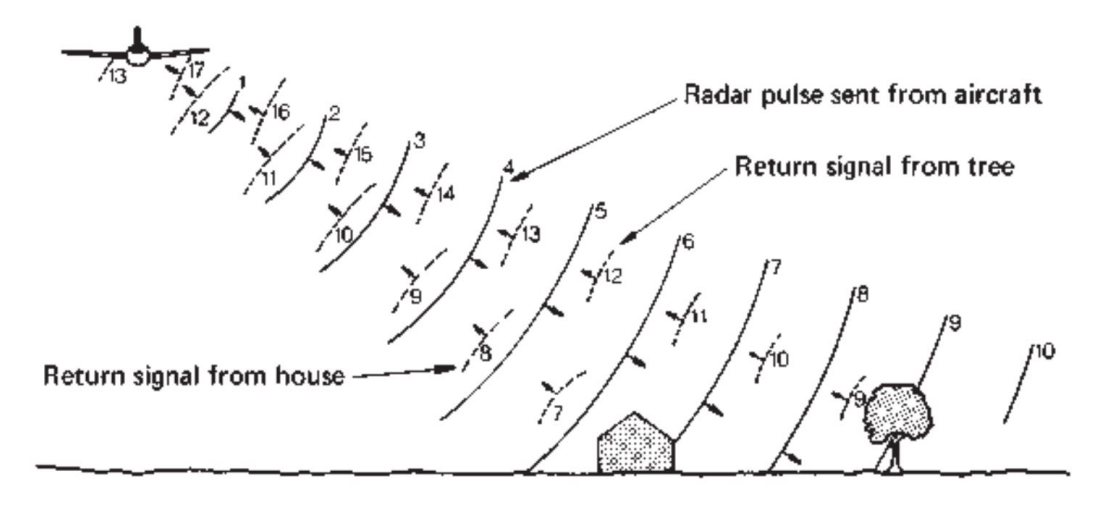


**Figure 2.1** How radar systems works [28]

and cross-track direction which is perpendicular to the moving imaging platform (azimuth direction) is defined as "range or look direction" (Figure 2.2). In order to determine the spatial resolution for any radar or SAR images, it's necessary to compute the resolutions in two directions: range and azimuth direction [27, 28].

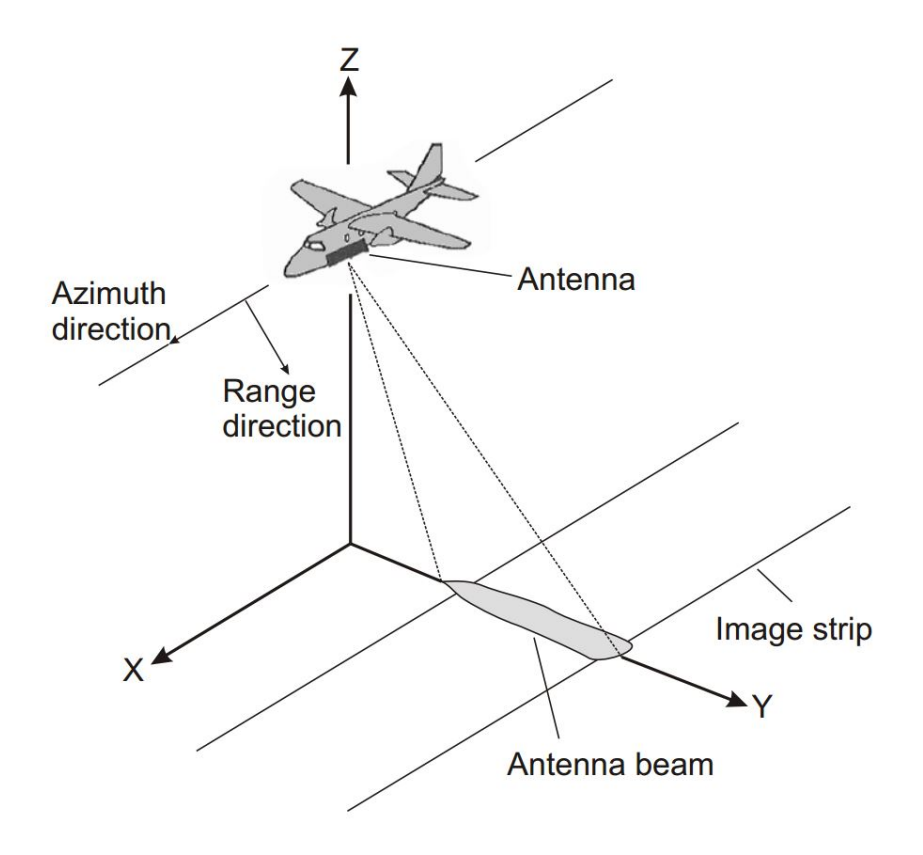


Figure 2.2 Side-looking airborne SAR geometry [29]

In terms of earth observation, airborne and spaceborne radar systems are referred to "imaging radar". The imaging radars for the first time were used in World War II in

order to detect aircrafts and ships. In the 1950s, SLAR (side-looking airborne radar) was developed and primarily used for military terrain reconnaissance. In mid-1960s, some of SLAR systems were declassified and started to be operated for the civilian mapping purposes. The use of SLAR systems in public-domain led to the development of space-borne SAR missions. The main limitation of SLAR systems has been the low or moderate azimuth resolution which is based upon antenna length in SLAR. This limitation was achieved by using coherent radar and Doppler beam sharpening, which were later extended to the principle of synthetic aperture radars (SAR)[26, 28].

As of today, imaging radar systems use SAR technology to observe the earth surface in high resolution. The first civilian satellite SEASAT was launched in 1978 by NASA (National Aeronautics and Space Administration) to collect oceanographic information in L-band and 25 meter spatial resolution. After this launch, the era for SAR remote sensing began in early 1990s and has been developing every year with new satellite missions [26, 28].

# 2.1 SAR Remote Sensing

Synthetic Aperture Radar systems have been actively used for remote sensing in the past decades because of providing high resolution and all-weather images. The principle of synthetic aperture is based upon Doppler beam sharpening and the use of a coherent radar, which was invented by Carl Wiley of the Goodyear Aircraft Corporation in 1951. SAR systems employ the short physical antenna however operate as if they have a very long antenna through the principle of synthetic aperture. This operation can be broadly and simply explained as follows: a single antenna is transformed into an array of antennas through the principle of the sensor motion on along track and such successive positions of antenna behave as if a long synthetic antenna (mathematically) [27, 28].

The main difference between synthetic aperture and real aperture is along-track (azimuth) resolution that was improved by synthetic aperture systems. In SAR systems, the azimuth resolution is equal to the half physical antenna length and independent from the range distance (distance between sensor and object). Before defining the range resolution, it is necessary to understand the term "range" in terms of radar imaging as two types of range are available as the slant-range and the ground-range. Accordingly, two types of range resolution are available in radar/SAR imaging. The slant-range resolution is equal to the half pulse length and not dependent to the distance from the aircraft. However, the ground-range resolution is depending upon the slant-range distance and depression angle. The depression angle

is complement of the look angle that is the angle between nadir (vertical direction) and radar beam [27, 28].

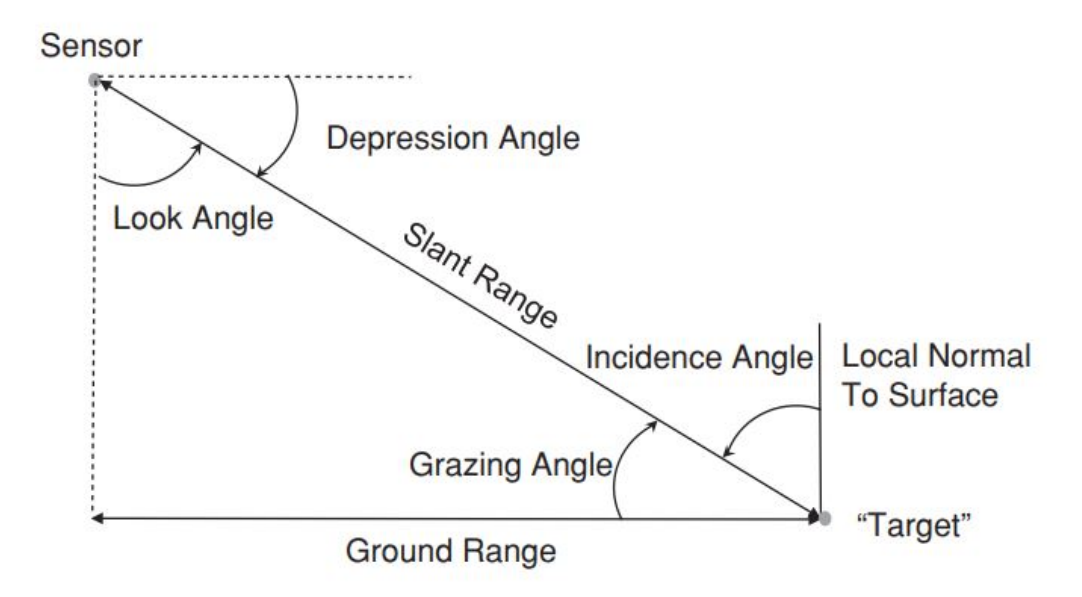


Figure 2.3 Ground and Slant Range [27]

The ground-range resolution  $(R_r)$  is defined as

$$R_r = \frac{c\tau}{2\cos\theta_d} \tag{2.1}$$

where c is the speed of light,  $\tau$  is the pulse duration and  $\theta_d$  is the depression angle [27, 28]. The azimuth resolution ( $\delta_a$ ) is

$$\delta_a = \frac{d_a}{2} \tag{2.2}$$

where  $d_a$  is the length of antenna [10, 27].

Synthetic Aperture Radar systems provide two-dimensional reflectivity images as these two dimensions correspond to range and azimuth direction. The visualizing of raw SAR data, unlike optical images, does not provide any useful information in terms of remote sensing interpretation however could only provide an image after signal processing steps that are simply the two separate matched filter (convolution) operations in range and azimuth dimensions [10]. In SAR imaging, backscattered signal is structured as a two-dimensional complex sample where each resolution cell (pixel) has an amplitude and a phase value. In this case, amplitude (correspondingly intensity) represents the value of the reflectivity and phase include the information distance between sensor and target. The amplitude and phase values of the

backscattered signal is heavily based on the electrical and physical properties of the target as well as the frequency and wavelength ranges of electromagnetic wave. Depending on the frequency and wavelength range, the penetration level for the target object varies. The most common used bands and their wavelength ranges are listed in Table 1 [10].

Table 2.1 Common bands and their wavelength ranges

Band	Frequency [GHz]	Wavelength [cm]
Ka	40–25	0.75–1.2
Ku	17.6–12	1.7–2.5
X	12–7.5	2.5–4
С	7.5–3.75	4–8
S	3.75–2	8–15
L	2–1	15–30
P	0.5-0.25	60–120

SAR images are display by using intensity (backscatter) values after calibration and geocoding [10]. These intensity values are depending on how SAR signal interacts with the surface, which is a function of several parameters such as surface roughness, permittivity, radar frequency, polarization, topography as well as radar viewing geometry [1, 30, 31]. In terms of the interaction between the SAR signal and target, three type of scattering happens. These three types of scattering include surface (single bounce) scattering, dihedral (double bounce) scattering, and volume scattering [7, 10].

In surface scattering, the intensity value of the backscatter signal varies based on the roughness level of the surface. If the height of the surface is much smaller than radar wavelength, the surface is considered as "smooth surface". Such smooth surfaces lead to specular reflection where only a small portion of energy backscatter to the sensor. However, a significant amount of energy returns to the radar for rough surfaces (diffuse reflection) and hence high backscattered areas (rough surfaces) appear brighter than smooth surfaces in SAR images. Incidence angle also plays a significant role in this case. When incidence angle increases, the surface appears smoother and accordingly in a brighter tone in SAR image [1, 31, 32].

Dihedral (double bounce) scattering mostly shows up on the features such as buildings and other types of man-made structures that might cause corner reflection. The surfaces at right angles lead to corner reflection that might also come out for natural targets like upright vegetation or cliff faces. Such targets directly send the radar energy back (backscattered signal) to antenna due to the corner reflectors and therefore appear very bright in SAR image[1, 31, 32].

Depending on the moisture level of the target (accordingly electrical properties of the target) and the wavelength of the radar signal, the scattering type can vary from surface scattering to volume scattering. For moist/wet targets, surface scattering (from specular to diffuse reflection) takes place in most cases based on surface characteristics (either smooth or rough) however for dry targets, radar signal is able to penetrate through the upper surface or canopy. In that type of penetration to the target (e.g. soil, forest or vegetation), the volume scattering occurs. In SAR imaging, the wet surfaces look brighter than dry surfaces (such as soil or vegetation) since the moisture content influence the electrical properties of the target and correspondingly the reflectivity[1, 31, 32].

Volume scattering happens if penetration takes places through the surface and usually is composed of multiple scattering (single and multiple scattering) from different layers of vegetation. The amount of how much energy backscattered to the radar within a volume can change depending on how radar signal interacts with the target either from the canopy (top surface) or from the ground. The volume scattering is also affected by the moisture content, surface roughness and the complex structure of the target[1, 31, 32].

Another important parameter for determining the radar backscatter is the polarization of the electromagnetic waves. Polarization plays an important role for understanding the target characteristics and structures since the targets provide different backscatter information based upon the selection polarization state of radar signal. Many radar systems are designed to transmit and receive the radar signal either horizontal (H) or vertical (V) polarization. In particular, polarimetric radars (full polarimetric or quad polarimetric) are managed to receive and transmit in both vertical and horizontal polarization. In this way, they provide the four combination of polarization as following: HH, HV, VH and VV, where first letter represents the polarization transmitted and the second one represents the polarization received back. and VV polarizations are entitled "like-polarization" while HV and VH polarizations are entitled "cross-polarization". Polarimetric radars can provide different and complementary information for the target by offering the full polarization regarding the scattering mechanism. Each polarization provides various information contents, which could help for easier interpretation of the complex surface characteristics [7, 31, 33].

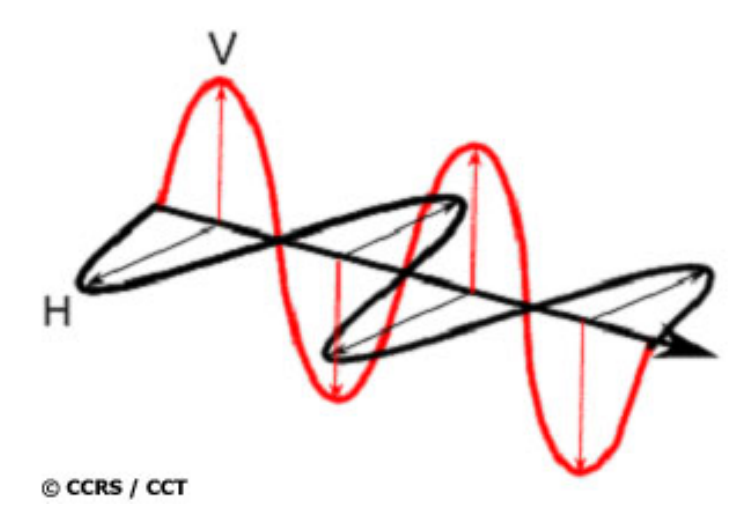


Figure 2.4 Vertical and Horizontal Polarizations [34]

Unlike optical images, radar images have an image characteristic called speckle that inherently exists in radar images and degrades the image quality. Speckle is a granular disturbance that can be modelled as multiplicative noise and the presence of speckle makes the interpretation difficult. Therefore it's recommended to reduce the speckle effect (a.k.a despeckling) in image for better analysis and easier interpretation. Speckle seems like a "salt and pepper" noise in image and can be reduced by two ways: multi-looking process or spatial filtering (or called speckle filtering). There is a trade-off between speckle reduction and spatial resolution since either way smooth the image while reducing the speckle therefore it should be carefully considered of how despeckling will be implemented to the image [7, 35, 36].

### 2.2 Polarimetric SAR

Full polarimetric SAR (PolSAR) sensors measure the full scattering for each resolution cell and these measurements are represented by  $2 \times 2$  scattering matrix, which referred as Sinclair matrix. For the horizontal (h) and vertical (v) polarizations in linear polarization basis, this  $2 \times 2$  scattering matrix **S** is given by

$$\mathbf{S} = \begin{bmatrix} S_{\text{hh}} & S_{\text{hv}} \\ S_{\text{vh}} & S_{\text{vv}} \end{bmatrix} \tag{2.3}$$

For the monostatic SAR systems, according to the reciprocity theorem, the transmitting and receiving antennas are located in the same position. In monostatic backscattering case, the diagonal terms of the measured scattering matrix are equal  $(S_{hv} = S_{vh})$ .

When SAR sensor illuminate a point (i.e. deterministic) target, the scattered wave is

completely polarized and the complete scattering can be represented by **S**. However this scattering matrix is not able to characterize the scattering process if a distributed target is illuminated by SAR sensor. Distributed targets (i.e. natural targets such as vegetation, forest or sea surface) are comprised of randomly distributed point targets and in that case, the scattered wave is partially polarized. Partial polarization refers to any case between two extreme cases of completely polarized and unpolarized waves. Distributed targets can be characterized by second-order scattering matrices (**T** or **C**).

The scattering matrix  ${\bf S}$  can be expressed in a vector format by defining the target vector  ${\bf k}$  as given below

$$\mathbf{k} = \frac{1}{2} Trace(\mathbf{S}\Psi) \tag{2.4}$$

where Trace(.) represent the sum of the diagonal elements of a matrix and  $\Psi$  denotes a set of  $2 \times 2$  complex basis matrices. In this vectorization process, the Lexicographic  $\Psi_L$  the Pauli  $\Psi_P$  basis sets are often used. The mathematical definitions of the target vector  $\mathbf{k}$  in the Pauli and lexicographic basis are provided below.

$$\mathbf{k}_{L} = \begin{bmatrix} S_{\text{hh}} & \sqrt{2}S_{\text{hv}} & S_{\text{vv}} \end{bmatrix}^{T} \tag{2.5}$$

$$\mathbf{k}_{p} = \frac{1}{\sqrt{2}} \begin{bmatrix} S_{\mathbf{h}\mathbf{h}} + S_{\mathbf{v}\mathbf{v}} & S_{\mathbf{h}\mathbf{h}} - S_{\mathbf{v}\mathbf{v}} & 2S_{\mathbf{h}\mathbf{v}} \end{bmatrix}^{T}$$
 (2.6)

where  $\mathbf{k}_P$  and  $\mathbf{k}_L$  denotes the target vector in Pauli and lexicographic basis, respectively. In terms of the interpretation of scattering process, Pauli formulation is more advantageous than lexicographic formulation [10, 37]

In order to describe the polarimetric scattering process for distributed targets, a stochastic process and second-order statistical formalism are required. In this case,  $3 \times 3$  covariance **C** or coherency **T** matrices are derived from the target vectors  $\mathbf{k}_L$  and  $\mathbf{k}_P$ , respectively.

The  $3 \times 3$  complex covariance matrix is defined as

$$\mathbf{C} = \left\langle \mathbf{k}_{t} \cdot \mathbf{k}_{t}^{\dagger} \right\rangle \tag{2.7}$$

which extends to

$$\mathbf{C} = \begin{bmatrix} \langle |S_{hh}|^2 \rangle & \sqrt{2} \langle S_{hh} S_{h\nu}^* \rangle & \langle S_{hh} S_{\nu\nu}^* \rangle \\ \sqrt{2} \langle S_{h\nu} S_{hh}^* \rangle & 2 \langle |S_{h\nu}||^2 \rangle & \sqrt{2} \langle S_{h\nu} S_{\nu\nu}^* \rangle \\ \langle S_{\nu\nu} S_{hh}^* \rangle & \sqrt{2} \langle S_{\nu\nu} S_{h\nu}^* \rangle & \langle |S_{\nu\nu}|^2 \rangle \end{bmatrix}$$
(2.8)

And the  $3 \times 3$  complex coherency matrix is given by

$$\mathbf{T} = \left\langle \mathbf{k}_p \cdot \mathbf{k}_p^{\dagger} \right\rangle \tag{2.9}$$

which extends to

$$\mathbf{T} = \frac{1}{2} \begin{bmatrix} \langle |S_{hh} + S_{\nu\nu}|^{2} \rangle & \langle (S_{hh} + S_{\nu\nu})(S_{hh} + S_{\nu\nu})^{*} \rangle & 2 \langle (S_{hh} + S_{\nu\nu})S_{h\nu}^{*} \rangle \\ \langle (S_{hh} - S_{\nu\nu})(S_{hh} + S_{\nu\nu})^{*} \rangle & \langle |S_{hh} - S_{\nu\nu}|^{2} \rangle & 2 \langle (S_{hh} - S_{\nu\nu})S_{h\nu}^{*} \rangle \\ 2 \langle S_{h\nu}(S_{hh} + S_{\nu\nu})^{*} \rangle & 2 \langle S_{h\nu}(S_{hh} - S_{\nu\nu})^{*} \rangle & 4 \langle |S_{h\nu}|^{2} \rangle \end{bmatrix}$$
(2.10)

In above equations,  $^{\dagger}$  and  $^{*}$  denote the conjugate transpose and the complex conjugate, respectively.

Both matrices are Hermitian semi positive definite and have the same eigenvalues. The conversion between **C** and **T** matrices is possible by means of a unitary similarity transformation [7, 37].

$$\mathbf{C} = \frac{1}{2} \begin{bmatrix} 1 & 1 & 0 \\ 0 & 0 & \sqrt{2} \\ 1 & -1 & 0 \end{bmatrix} \mathbf{T} \begin{bmatrix} 1 & 0 & 1 \\ 1 & 0 & -1 \\ 0 & \sqrt{2} & 0 \end{bmatrix}$$
 (2.11)

# 2.3 Polarimetric Target Decompositions

Polarimetric target decompositions (also referred as target decompositions in radar polarimetry) are primarily aimed to separate the complex scattering contributions in a resolution cell into a sum of elementary scattering elements to provide the simple interpretation of complex scattering by means of mathematical and physical based models [10, 13]. For this reason, these are widely used for the classification/segmentation or parameter inversion. The elemantary scattering mechanisms include the surface, double bounce (dihedral) and volume scattering. Another important objective of the polarimetric target decompositions is to provide accurate inference to the geophysical parameters of complex scattering [13]. The

target decompositions were first formalized by Huynen [38] and other target decomposition theorems have been proposed afterwards such as Cloude and Pottier [39], Freeman and Durden [40], and Van Zyl [41].

Target decompositions can be categorized into four main groups [7].

- Dichotomy of the Kennaugh matrix **K** (Huynen [38], Holm and Barnes [42], Yang [43])
- Eigenvector-based decompositions (Cloude [44], Holm [42], van Zyl [45], Cloude and Pottier [39, 46])
- Model-based decompositions (Freeman and Durden [40], Yamaguchi [47], Dong [48])
- Coherent decompositions (Krogager [49], Cameron [50], Touzi [51])

Coherent decompositions are based on the decomposition of [S] matrix and can only be used for coherent scatterers. The main disadvantage of coherent decompositions is that they ignore the high speckle noise effects in single look complex SAR data, which can be limiting factor for the physical interpretation of the coherent targets (i.e. point or pure target) [7]. For distributed scatterers, the incoherent decompositions that employ the second-order scattering matrices (T or C) are used [7, 11, 33]. The incoherent decompositions are divided into two categories: eigenvector-based decompositions and model-based decompositions. Eigenvector-based decompositions are based on the eigenvector or eigenvalues analysis of the T or C matrices, which could be referred as mathematical based decompositions. Model-based decompositions are based on the decomposition of the T or C matrices [7, 8].

In this thesis, incoherent target decompositions were implemented and therefore only the basic details for eigenvector-based and model-based decomposition are provided in the following subsections. More detailed information for polarimetric target decompositions can be found in [7] and [33].

### 2.3.1 Eigenvector based decomposition

Eigenvector-based decompositions are based on the eigenvector/eigenvalue analysis of the  $3\times3$  T or C matrices. An important example of eigenvector-based decompositions is the Cloude-Pottier decomposition which decompose the  $3\times3$  Hermitian coherency

**T** matrix. Since being Hermitian and semi-definite positive, the coherency **T** matrix can be diagonalized as given by

$$\mathbf{T} = \left[\mathbf{U}\right] \left[\mathbf{\Lambda}\right] \left[\mathbf{U}\right]^{-1} \tag{2.12}$$

where

$$\mathbf{\Lambda} = \begin{bmatrix} \lambda_1 & 0 & 0 \\ 0 & \lambda_2 & 0 \\ 0 & 0 & \lambda_3 \end{bmatrix} \tag{2.13}$$

$$\begin{bmatrix} \mathbf{U} \end{bmatrix} = \begin{bmatrix} \epsilon_{11} & \epsilon_{12} & \epsilon_{13} \\ \epsilon_{21} & \epsilon_{22} & \epsilon_{23} \\ \epsilon_{31} & \epsilon_{32} & \epsilon_{33} \end{bmatrix}$$
 (2.14)

The equation 2.12  $\Lambda$  denotes the diagonal eigenvalue matrix with elements of nonnegative eigenvalues,  $\lambda_1 \geq \lambda_2 \geq \lambda_3 \geq 0$  and  $\begin{bmatrix} \mathbf{U} \end{bmatrix}$  is the unitary eigenvector matrix with three orthogonal eigenvectors of  $\vec{\epsilon_1}, \vec{\epsilon_2}$  and  $\vec{\epsilon_3}$ , as provided below

$$\begin{bmatrix} \mathbf{U} \end{bmatrix} = \begin{bmatrix} \vec{\epsilon_1} & \vec{\epsilon_2} & \vec{\epsilon_3} \end{bmatrix} \tag{2.15}$$

The main idea of eigenvector approach is to decompose  $3 \times 3$  T matrix into a sum of three independent (orthogonal) coherency matrices  $T_i$ .

$$\mathbf{T} = \mathbf{T}_1 + \mathbf{T}_2 + \mathbf{T}_3$$

$$= \lambda_1 \cdot (\vec{\epsilon}_1 \cdot \vec{\epsilon}_1^{\dagger}) + \lambda_2 \cdot (\vec{\epsilon}_2 \cdot \vec{\epsilon}_2^{\dagger}) + \lambda_3 \cdot (\vec{\epsilon}_3 \cdot \vec{\epsilon}_3^{\dagger})$$
(2.16)

In this decomposition, the polarimetric features are provided which are entropy  $\mathbf{H}$ , anisotropy  $\mathbf{A}$  and mean alpha angle  $\alpha$ . The entropy  $\mathbf{H}$  and anisotropy  $\mathbf{A}$  are derived from the eigenvalues while mean alpha angle  $\alpha$  is calculated by using corresponding eigenvectors [7, 8, 39]. The definitions of each parameters as well as their mathematical expressions are given in following paragraphs.

The first parameter is the entropy H, which is defined as the logarithmic sum of the

eigenvalues.

$$\mathbf{H} = -\sum_{i=1}^{3} p_i \log_3 p_i \tag{2.17}$$

$$p_i = \frac{\lambda_i}{\sum_{k=1}^3 \lambda_k} \tag{2.18}$$

where  $p_i$  is the probability of the eigenvalue  $\lambda_i$ 

Entropy measures the degree of randomness of the scattering and ranges from 0 to 1. When entropy is equal to zero ( $\lambda_2 = \lambda_3 = 0$ ), there is one non-zero eigenvalue is present and the scattering process is described by single scattering. However, the entropy is mostly assigned a value between 0 and 1 for distributed (incoherent) scatterers.

The second parameter is the anisotropy **A**, which also ranges between 0 and 1. It is defined as the normalized difference of the second and third eigenvalues, by taking into account that  $\lambda_1 \geq \lambda_2 \geq \lambda_3 \geq 0$ 

$$\mathbf{A} = \frac{\lambda_2 - \lambda_3}{\lambda_2 + \lambda_3} \tag{2.19}$$

Anisotropy provide the complementary information to the entropy and can play an important role to distinguish the different types of scattering when entropy reaches to a high value (when H > 0.7). This is because second and third eigenvalues are highly affected by noise in low entropy values. Accordingly, the anisotropy becomes also noisy. Anisotropy expresses the relative importance of third eigenvalue with respect to second eigenvalue[7, 8, 39].

The third parameter is the mean alpha angle  $\alpha$  and alpha angle  $\alpha_i$  defines the scattering types. For each eigenvector  $(\vec{e_i})$ , the alpha angle  $\alpha_i$  is calculated as following and ranges from 0 to 90 degrees.

$$\alpha_i = \arccos(|\epsilon_{1i}|) \tag{2.20}$$

And following, the mean alpha angle  $\alpha$  is given by

$$\alpha = p_1 \alpha_1 + p_2 \alpha_2 + p_3 \alpha_3 \tag{2.21}$$

The scattering types are defined based on the ranges of alpha angle  $\alpha_i$  as follows [7, 8, 10].

- Surface scattering if  $0^{\circ} \le \alpha_i \le 30^{\circ}$
- Dipole scattering if  $40^{\circ} \le \alpha_i \le 50^{\circ}$
- Dihedral scattering if  $60^{\circ} \le \alpha_i \le 90^{\circ}$

The Van Zyl decomposition is also an eigenvector-based decomposition and referred as non-negative eigenvalue decomposition (NNED). Van Zyl decomposition is the modified version of the Freeman and Durden decomposition and combines model-based decomposition and eigenvector decomposition [7, 13, 41].

The fundamental idea of Van Zyl decomposition is to avoid negative eigenvalues that might occur for the pixels in the vegetated areas once the scattering from the vegetation is subtracted. This target decomposition is classified as a hybrid (model-based with eigen-based) decomposition because the polarimetric features of this method are very similar to those obtained from model-based decomposition (i.e. surface, double-bounce and volume scattering) [7, 41, 52].

### 2.3.2 Model based decomposition

Eigenvector-based decompositions provide the unique mathematical outputs that have to be interpreted in terms of known polarimetric scattering. These mathematical results can not be directly related to the physical scattering models such as surface or volume scattering. For this case, model based decompositions are more straightforward and easier to implement on PolSAR data for clearer understanding and easier interpretation of the complex scattering process [13, 53].

Model based decompositions aim to decompose the complex scattering into elementary contributions and model the scattering as the linear sum of the different scattering mechanism [13, 41]. Freeman and Durden decomposition (also knows as Three-Component Decomposition), one of the first model-based decomposition techniques, decomposes the coherency **T** matrix into three physical scattering mechanism [7, 40]:

- Surface or single-bounce scattering (a first-order Bragg surface scattering)
- Dihedral or double-bounce scattering (a dihedral reflection)
- Volume scattering ( a volume of randomly oriented dipole scattering)

$$\mathbf{T} = f_{s} \begin{bmatrix} 1 & b^{*} & 0 \\ b & |b|^{2} & 0 \\ 0 & 0 & 0 \end{bmatrix} + f_{d} \begin{bmatrix} |a|^{2} & a & 0 \\ a^{*} & 1 & 0 \\ 0 & 0 & 0 \end{bmatrix} + \underbrace{f_{\nu}}_{4} \begin{bmatrix} 2 & 0 & 0 \\ 0 & 1 & 0 \\ 0 & 0 & 1 \end{bmatrix}$$
Surface Scattering
Dihedral Scattering
Volume Scattering
(2.22)

In surface scattering, there are two parameters are describing the scattering process: the real ratio b and the backscatter contribution  $f_s$  as follows

$$b = \frac{\left(R_s + R_p\right)}{\left(R_s - R_p\right)} \tag{2.23}$$

and

$$f_s = \left| R_s - R_p \right|^2 \tag{2.24}$$

where  $R_s$  and  $R_p$  represent the Bragg scattering coefficients perpendicular and parallel to the incident plane.

There are two parameters to describe the dihedral scattering which are the scattering amplitude  $f_d$  and the ratio a. Their definitions are provided below

$$f_d = \frac{1}{2} |R_{sh}R_{th} + R_{sv}R_{tv} \exp(i\phi)|^2$$
 (2.25)

and

$$a = \frac{R_{sh}R_{th} - R_{s\nu}R_{t\nu} \exp(i\phi)}{R_{sh}R_{th} + R_{s\nu}R_{t\nu} \exp(i\phi)}$$
(2.26)

where  $R_{sh}$  and  $R_{sv}$  represent the horizontal and vertical Fresnel coefficients for the soil and  $R_{th}$  and  $R_{tv}$  are the horizontal and vertical Fresnel coefficients for the trunk. The Fresnel coefficients  $R_h$  and  $R_v$  are depending on the local incidence angle  $\theta$  and relative dielectric constant  $\varepsilon_r$  as follows [10, 33, 54].

$$R_h = \frac{\cos \theta - \sqrt{\varepsilon_r - \sin^2 \theta}}{\cos \theta + \sqrt{\varepsilon_r - \sin^2 \theta}}$$
 (2.27)

$$R_{\nu} = \frac{\varepsilon_r \cos \theta - \sqrt{\varepsilon_r - \sin^2 \theta}}{\varepsilon_r \cos \theta + \sqrt{\varepsilon_r - \sin^2 \theta}}$$
 (2.28)

The volume scattering is described by the scattering amplitude  $f_{\nu}$  (vegetation component) which is often approximated by a cloud of ellipsoids [7, 10].

The scattering power for the surface  $P_s$ , dihedral  $P_d$  and volume  $P_v$  components are given by

$$P_{s} = f_{s} \cdot (1 + |b|^{2}) \tag{2.29}$$

$$P_d = f_d \cdot (1 + |a|^2) \tag{2.30}$$

$$P_{\nu} = f_{\nu} \tag{2.31}$$

And following, the total power (Span) is obtained as follows [7, 10]

$$P_{total} = P_s + P_d + P_v$$
  
=  $f_s \cdot (1 + |b|^2) + f_d \cdot (1 + |a|^2) + f_v$  (2.32)

# **Classification and Accuracy Metrics**

# 3.1 Image Classification

Image classification is still a challenging task because of some uncertainties such as proper representativeness of training samples and the adaptation between classification model and training data. The extraction of the land use/cover information from the remotely sensed images is typically performed by using classification algorithms. Image classification is the process of assigning pixels into one of pre-defined classes in the classification scheme based on their spectral ranges. Based on the availability of training data (the sample pixels of pre-defined classes), the classification algorithms are grouped as two categories: supervised and unsupervised. In most cases, supervised ones are more robust and obtain higher accuracy compared to unsupervised methods [55, 56].

With respect to consideration for the distribution assumptions of the sample pixels, the classification algorithms can be split into parametric and nonparametric methods. Parametric methods assume that the distribution of sample data (also known as probability density function) for each class follow a normal distribution while nonparametric methods do not have any constrain by any assumption regarding the distribution of sample data [55, 57]. In remote sensing, machine learning algorithms are widely used and accepted for image classification. The majority of advanced machine learning algorithms are nonparametric such as SVM, RF and DT [58, 59].

In supervised learning, the learning stage is based upon a number of factors, such as design (purity and set size) of training samples, data dimensionality, resolution of input imagery, and selection of proper features. The uncertainty in the training stage of supervised learning causes to implement different type of classification model to achieve the higher accuracy [57, 60]. There are several approaches are available in machine learning for classification purposes such as margin based classifiers, ensemble classifiers, instance-based classifiers and neural-network based classification approaches. Each model has different functionalities and constrain based upon the

data type and training samples [59, 61].

Ensemble learning algorithms (multiple classifiers) have attracted many researchers in the areas of machine learning and remote sensing as it may achieve higher accuracy compared to single (based) classifiers. The most common ensemble learning algorithm for remote sensing is Random forest [62, 63]. Relatively newer ensemble learning algorithms such as rotation forest [64], random M5 model forest [65], extratrees [66], extreme gradient boosting [67], canonical correlation forest [68], ForestPA [69] and Light gradient boosting machine [70] have been investigated in remote sensing, however have not yet been fully explored for the "crop classification" with SAR/PolSAR data.

Xia et al.(2014) applied the rotation forest for the classification of hyperspectral images first time in remote sensing and compared the performance of rotation forest with RF, AdaBoost and bagging. Their research deduced that rotation forest obtained higher accuracy than RF, AdaBoost and bagging. [64]

Du et al.(2015) assessed the impact of polarimetric and spatial features on the classification of PolSAR data using RF, rotation forest, SVM and supervised Wishart classifier. For polarimetric features, they employed polarimetric decompositions. Their research pointed out that rotation forest can obtain higher accuracy in comparison to RF and SVM [71].

Samat et al.(2018) proposed a novel ensemble learning algorithm "random M5 model forest" to classify land cover types by using full polarimetric L-band ALOS 2 data to map halophyte plants. They analysed the performance of random M5 model forest in comparison to RF, rotation forest, SVM and MultiBoost. Their results decided that random M5 model forest could outperform other classifiers employed in their research study [65].

Mills and Fotopoulos (2015) exploited the extratrees for the classification of rock surface on the purpose of modelling the natural surface [72].

Samat et al.(2018) explored the ability of extratrees for the classification of very high resolution multispectral images and compared the performance with RF, SVM, rotation forest and bagging. In their experimental results, extratrees obtained better results than others [66].

Georganos et al. (2018) explored the XGBoost for the object based classification of urban land use and cover using very high resolution images. They compared the classification performance of CCF with SVM and RF. In their experimental results,

XGBoost ourperformed SVM and RF in terms of classification accuracy [73].

Dong et al. (2018) used XGBoost for the classification of Chinese Gaofen-3 (GF-3) PolSAR image and compared with SVM, RF and DT. They concluded that XGBoost showed comparable results but with less computation time [74].

Xia et al.(2017) compared the performance of CCF for the hyperspectral image classification with random forest (RF) and rotation forest (RoF) in terms of accuracy and computational complexity. Their experimental results demonstrated that CCF received greater performance than RF and RoF [75].

Likewise, Colkesen and Kavzoglu (2017) also tested CCF for land use/cover classification and compared with random forest (RF) and rotation forest (RoF). However, they used multispectral images (Sentinel-2 and Landsat-8) for land use and cover classification. Their results concluded that RoF and CCF produced similar results statistically [76].

Samat et al.(2019) investigated the performance of ForestPA for the first time in remote sensing for the classification of multispectral and hyperspectral images using spextral and morphological features. To evaluate the performance of ForestPA, they also exploited SVM and ensemble classifiers such as bagging, extratrees, RF and rotation forest. They concluded that ForestPA could only obtain better accuracy than bagging and found to be not proper forthe classification of high dimensional data [69].

Ustuner and Sanli (2019) compared the impacts of original features and polarimetric features (desomposed parameters) for the crop classification using LightGBM and multitemporal RADARSAT-2 images. Their results proved the benefits of the polarimetric decomposition parameters for classification of crops [25].

In this thesis work, one recently developed LightGBM and two well-known classifiers (SVM and RF) were used.

• Ensemble classifiers: LightGBM and RF

• Margin-based classifier: SVM

The brief summary of the classification methods are provided in following subsections. More details about the classification methods can be found in [70], [77] and [78] for LightGBM, SVM and RF, respectively

### 3.1.1 Support Vector Machines

Support vector machines are the kernel-based learning algorithms from statistical learning theory and have been widely used in remote sensing and pattern recognition for the classification and regression problems. SVMs were originally developed by Vapnik and Cortes [79] to define the optimal linearly-separating hyperplane (the class boundary) in a feature space in order to separate two classes with maximum margin. Here the term "margin" refers to the distance between two hyperplanes and classification errors are minimized by maximizing the margin. In order to maximize the margin, SVMs utilize the "support vectors" which are the closest training samples to the optimal separating hyperplane and lie on individual class hyperplane in feature space. In order to define the decision boundaries, support vectors are sufficient and these samples usually represent only a small portion of total training data [77, 80, 81].

SVMs are also popular in handling the classification problems of high dimensional data (e.g. hyperspectral data) with a limited number of training samples since only closest training samples (i.e. support vectors) are initially needed for placing the hyperplanes [61].

For the binary classification problem, consider a training dataset with k number of samples in a n-dimensional feature space is represented by:

$$\{\mathbf{x}_i, y_i\}, \qquad i = 1, ..., k$$
 (3.1)

where  $\mathbf{x}_i \in R^n$  represent the training samples in  $R^n$  which is an n-dimensional vector and  $y_i \in \{-1, +1\}$  is the class label.

The hyperplane separating for two classes in the linearly separable case given by

$$\mathbf{w} \cdot \mathbf{x}_i + b \ge 1$$
, for all  $y = +1$  (3.2)

$$\mathbf{w} \cdot \mathbf{x}_i + b \le -1, \quad \text{for all} \quad y = -1 \tag{3.3}$$

and these two inequalities can be combined into as follows

$$y_i(\mathbf{w} \cdot \mathbf{x}_i + b) - 1 \ge 0 \tag{3.4}$$

where  $\mathbf{w}$  denotes a vector which determines the orientation of the hyperplane, b is the distance of hyperplane from the origin point [77, 80, 81].

In this case, support vectors are defined by the functions  $\mathbf{w} \cdot \mathbf{x}_i + b = \pm 1$ .

In order to determine the optimal hyperplane in the linearly separable case, it is required to solve the optimization problem as follows:

$$\min\left[\frac{1}{2}\|\mathbf{w}\|^2\right] \tag{3.5}$$

$$y_i(\mathbf{w} \cdot \mathbf{x}_i + b) \ge 1$$
, and  $y_i \in \{-1, +1\}$  (3.6)

When it is not possible to separate the two classes with a linear function, the slack variable  $\xi$  is introduced. In this case, the optimization problem becomes,

$$\min\left[\frac{\|\mathbf{w}\|^2}{2} + \mathbf{C}\sum_{i=1}^r \xi_i\right] \tag{3.7}$$

$$y_i(\mathbf{w} \cdot \mathbf{x}_i + b) \ge 1 - \xi_i, \quad \xi_i \ge 0, \quad i = 1, ..., n$$
 (3.8)

where **C** is the penalty parameter and  $\xi$  is the slack variable. Both terms are deal with the incorrectly classified pixels for the linearly non-separable cases.

In some cases, defining the optimal hyperplane is not possible in linear feature space. For such cases, the training data can be projected into higher dimensional feature space (H) by using nonlinear mapping functions  $(\Phi)$ . Thus, the decision function for the classification is obtained as

$$f(x) = sign\left(\sum_{i}^{r} \lambda_{i} y_{i} \mathbf{K}(x_{i}, x_{j}) + b\right)$$
(3.9)

where  $\lambda_i$  is a Lagrance multiplier and  $y_i$  is a class label. A kernel function is defined as  $\mathbf{K}(x_i, x_i) = \mathbf{\Phi}(x_i) \cdot \mathbf{\Phi}(x_i)$  is the kernel function.

There are four types of kernel commonly used in SVM classification as follows: linear, polynomial, radial basis function (RBF) and sigmoid. In our experiment, the radial

basis function was employed as a kernel, as provided below

$$\mathbf{K}(x_i, x_j) = \exp\left(-\gamma \left\|x_i - x_j\right\|^2\right) \tag{3.10}$$

There are two parameters have to be determined for RBF kernel which are the kernel width ( $\gamma$ ) and penalty parameter **C** [77, 80, 81].

#### 3.1.2 Random Forest

Random forest (RF) is an ensemble-based learning algorithms which combine the results (i.e. predictions) of several individual classifiers through a voting process. The fundamental purpose of ensemble classifiers is to improve the classification performance as the underlying reason is a set of classifiers could outperform the single (base) classifiers in terms of performance [78, 82, 83]. There are several ensemble learning algorithms such as bagging [84] (bootstrap aggregating), boosting [85], random forest [86], rotation forest [87], extremely randomized trees [88], canonical correlation forest (CCF) [68], extreme gradient boosting (XgBoost)[67], and Light Gradient Boosting Machine (LightGBM) [70]. The most widely used ones are bagging (bootstrap aggregating), boosting, and random forest [62, 63, 83].

Bagging creates the training sample subsets by resampling the original dataset several times in a random selection (i.e. bootstrap sampling) and trains a (base) classifier with these bootstrapped samples. The final classifier is generated by combining all these individual outputs though majority voting. [62, 63, 83].

Boosting is an iterative training process and aims increasing the performance of weak learners. As a initial step, all training samples are weighted equally. During the boosting step, the training samples are re-weighted and the misclassified pixels are assigned the stronger weight than correctly-classified pixels. Thus, the classifier is forced to concentrate on misclassified samples to reduce the classification error. In other saying, boosting aims to improve the classification accuracy by increasing the weights of misclassified samples while decreasing the weights of correctly classified ones [62, 63, 83].

Random forest (RF) is the ensemble of tree-type (e.g. decision trees) classifiers and uses of the different subsets of training data generated through the bagging or bootstrap aggregating to build the ensemble therefore it can be considered as an improved version of bagging. RF uses the decision trees as base classifiers,  $\{h(\mathbf{x}, \theta_i), i = 1, ..., \}$ , where  $\mathbf{x}$  is the input vector and  $\theta_i$  denotes the independent and

identically distributed random vectors. Each tree is trained through a bootstrapped sample of training data and the split for each node is determined by using a randomly selected subset of input data. At the end of this process, several classification results are obtained. The final classification is constructed through the majority voting of the trees

There are two model parameters need to be tuned for RF classification, which are the number of trees (T) and the number of features (M). The computational time of RF is calculated through  $cT\sqrt{MN}\log(N)$ , where c is a constant and N denotes the number of samples. In terms of computational time, RF is faster than boosting and bagging since it uses of subsets of input data [62, 63, 83].

### 3.1.3 Light Gradient Boosting Machines

Gradient boosting decision tree (GBDT) [89] is one of the tree-based machine learning algorithm and has been preferred in classification and regression tasks because of its efficiency and interpretability. In the last few years, the increasing of the data size and feature dimension in earth observation data obliged researchers to develop more optimized and efficient solutions in terms of accuracy, time and efficiency [70]. The extended and modified versions of GBDT have been developed by the machine learning community in recent years such as XGBoost [67], LightGBM [70], mGBDTs [90] and CatBoost [91]. All these new algorithms have been developed for higher accuracy, faster training speed as well as lower memory usage compared to GBDT in handling big data [70].

In this thesis, we chose LightGBM among all these newly developed gradient boosting frameworks since it was placed the first ranking in many machine learning competition and outperformed other gradient boosting frameworks on public datasets in terms of efficiency, accuracy and lower memory consumption. [92]

LightGBM takes the advantages of using two novel techniques: Gradient-based One-Side Sampling (GOSS) and Exclusive Feature Bundling (EFB) which are deal with the number of data instances and features, respectively [70].

• Gradient-based One-Side Sampling (GOSS): GOSS primarily aims to reduce the number of data instances (or subsampling the data) while keeping the accuracy of learned decision trees. Conventional GBDT scans all data instances to calculate the information gain for each feature however GOSS only uses the significant data instances. In other words, GOSS keeps the instances with large gradients and randomly drop the instances with small gradients to retain the

accuracy of information gain while downsampling the data. By doing this, GOSS reduces the data instances without much effecting the data distribution [70, 93, 94].

• Exclusive Feature Bundling (EFB): EFB ultimately aims to reduce the number of features and accordingly improve the efficiency of model training without hurting the accuracy. EFB has two internal processing steps: constructing the bundles and merging the features into the same bundle. Many features in a sparse feature space are almost exclusive (i.e. rarely take nonzero values simultaneously) and these exclusive features can be bundled through a greedy algorithm (referred as greedy bundling). At the same time, it was aimed to merge such many exclusive features into a single (or same) bundle to reduce the training complexity. Through this way, EFB merges sparse features into fewer dense features and correspondingly leads to faster training process along with lower memory consumption [70, 93, 94].

By using these two novel functions, LightGBM could reduce the number of data instances and features, which improves the efficiency of training process as well as speed up the process. Apart from the other boosting frameworks, LightGBM uses histogram-based algorithms rather than presorted-based algorithms to find the optimal (i.e.best) split points. [70, 93, 94]

For the implementation of LightGBM, LightGBM Python Package v.2.2.2 that can be freely accessible at [95] was utilized. The main (core) parameters of LightGBM can be listed as following:

**Table 3.1** LightGBM Parameters

Classification

Number of leaves per tree

Learning rate

Maximum learning depth

Minimum number of data per in a leaf

Feature fraction

Bagging fraction

More details about the descriptions of the parameters of LightGBM can be found at [96].

# 3.2 Accuracy Measures

### 3.2.1 Overall Accuracy and Kappa Coefficient

In order to assess the performance of the classification model, there are several measures such as overall accuracy and kappa coefficient widely used in remote sensing. These measures are can be derived from a confusion or error matrix.

In this content, the 'accuracy' means the degree of the 'correctness' of the classified image. In other words, it represents of how much a classified image conform to the ground truth or reference map. Error matrix also provides the information about the class-confusion or the misclassified samples for a particular class [97].

An example of an error matrix with four classes are provided in Table 3.2 where the diagonal elements represent the correctly classified samples while off-diagonal elements demonstrate the misclassified samples or class confusion [97].

**Table 3.2** An error matrix with four classes

	Class a	Class b	Class c	Class d	$\sum$
Class a	$m_{aa}$	$m_{ab}$	$m_{ac}$	$m_{ad}$	$m_{a+}$
Class b	$m_{ba}$	$m_{bb}$	$m_{bc}$	$m_{bd}$	$m_{b+}$
Class c	$m_{ca}$	$m_{cb}$	$m_{cc}$	$m_{cd}$	$m_{c+}$
Class d	$m_{da}$	$m_{db}$	$m_{dc}$	$m_{dd}$	$m_{d+}$
$\sum$	$m_{+a}$	$m_{+b}$	$m_{+c}$	$m_{+d}$	m

For a given error matrix above, the overall accuracy and kappa coefficient, can be derived from a confusion matrix, are computed as given by

Overall Accuracy = 
$$\frac{\sum_{k=1}^{q} m_{kk}}{m} \times 100$$
 (3.11)

Kappa Coefficient = 
$$\frac{m\sum_{k=1}^{q}m_{kk} - \sum_{k=1}^{q}m_{k+}m_{+k}}{m^2 - \sum_{k=1}^{q}m_{k+}m_{+k}}$$
(3.12)

where q represent the number of classes and m is the total number of reference pixels [97].

Furthermore, a few number of measures (User's accuracy, Producer's accuracy and F1-score) are computed as following for the given error matrix:

User's accuracy (UA) = 
$$\frac{m_{ii}}{m_{i+}}$$
 (3.13)

Producer's accuracy (PA) = 
$$\frac{m_{ii}}{m_{+i}}$$
 (3.14)

F1-score = 
$$2 \times \frac{(PA \times UA)}{(PA + UA)}$$
 (3.15)

These three measures (PA, UA and F1-score) are used for the class-based accuracy assessment [97].

#### 3.2.2 McNemar's test

In order to analyse the differences between two classifier performance in terms of whether this difference is statistical significance or not significant, McNemar's test is utilized. This test is based upon  $2 \times 2$  confusion matrix.

McNemar's test is based on the standardized normal test statistic as given by:

$$z = \frac{f_{12} - f_{21}}{\sqrt{f_{12} + f_{21}}} \tag{3.16}$$

where  $f_{12}$  and  $f_{21}$  are defined in the given  $2 \times 2$  confusion matrix in Table 3.2.

**Table 3.3**  $2 \times 2$  confusion matrix and elements in equation 3.16

	Classification 2		
Allocation	Correct	Incorrect	
Classification 1			
Correct	$f_{11}$	$f_{12}$	
Incorrect	$f_{21}$	$f_{22}$	

The use of McNemar's test within remote sensing is based upon a chi-square ( $\chi^2$ ) distribution with one degree of freedom [63, 97, 98]. For such cases, McNemar's test is expressed as

$$\chi^2 = \frac{(f_{12} - f_{21})^2}{f_{12} + f_{21}} \tag{3.17}$$

The statistical significance is evaluated based on the  $(\chi^2)$  value. If the  $(\chi^2)$  value is greater than the critical table value  $(\chi^2=3.84$  at 95% confidence interval), it means that the difference in the accuracy between two classifiers is statistically significant [63, 99].

#### 3.2.3 K-Fold Cross Validation

K-Fold cross validation is commonly used in machine learning for estimating the model accuracy as well as for parameter optimization. In this method, the whole reference data was randomly split into equally sized k fold (or part). The model is trained using k-1 folds and is assessed using the withheld one part. Each time different partition is used as testing data, as illustrated in Figure 3.1 where k is equal to 5. The model is run k times and the model accuracy is the average of k different predictions. In our case, k is equal to 5 [100, 101].

The main advantage of K-Fold cross validation is that it ensures every sample of the reference data is used as training and testing, which leads to less biased and more fair estimates for model accuracy [102, 103]

Iteration 1	Test	Train	Train	Train	Train
Iteration 2	Train	Test	Train	Train	Train
Iteration 3	Train	Train	Test	Train	Train
Iteration 4	Train	Train	Train	Test	Train
Iteration 5	Train	Train	Train	Train	Test

Figure 3.1 5-Fold cross validation

# **Experimental Design**

This chapter will provide you with an overview of experimental design for data processing (Figure 4.5) and analysis (i.e. methodology) conducted in this thesis. Furthermore, the study area and data set are introduced in the first section.

# 4.1 Study Area and Data set

The study site is located in Konya province of Turkey and extending from 38°43′ to 38°53′ North latitudes and 32°43′ to 32°53′ East longitudes (approx.65 km north of Konya city center), as illustrated in Figure 4.1. The region has flat topography, productive soils and good weather condition (e.g. solar illumination, precipitation), thus such points make this region very ideal for agricultural operations. The major crops covering the study site are alfalfa, maize, potato, sunflower and wheat.

Multi-temporal RADARSAT-2 data was acquired on following dates: 13 June, 7 July, 31 July, and 24 August in 2016 (Figure 4.2). The specifications of the RADARSAT-2 images are presented in Table 4.1.

Table 4.1 Specification of RADARSAT-2 image

Sensor Type	RADARSAT-2
Wavelength	C Band- 5.6 cm
Resolution	4.7m x 5.1 m (range x azimuth)
Incidence angle	40
Pass direction	Descending
Acquisition type	Fine quad pol
Polarization	Full polarimetric
Nominal Scene Size	25 x 25 km
Product type	Single look complex

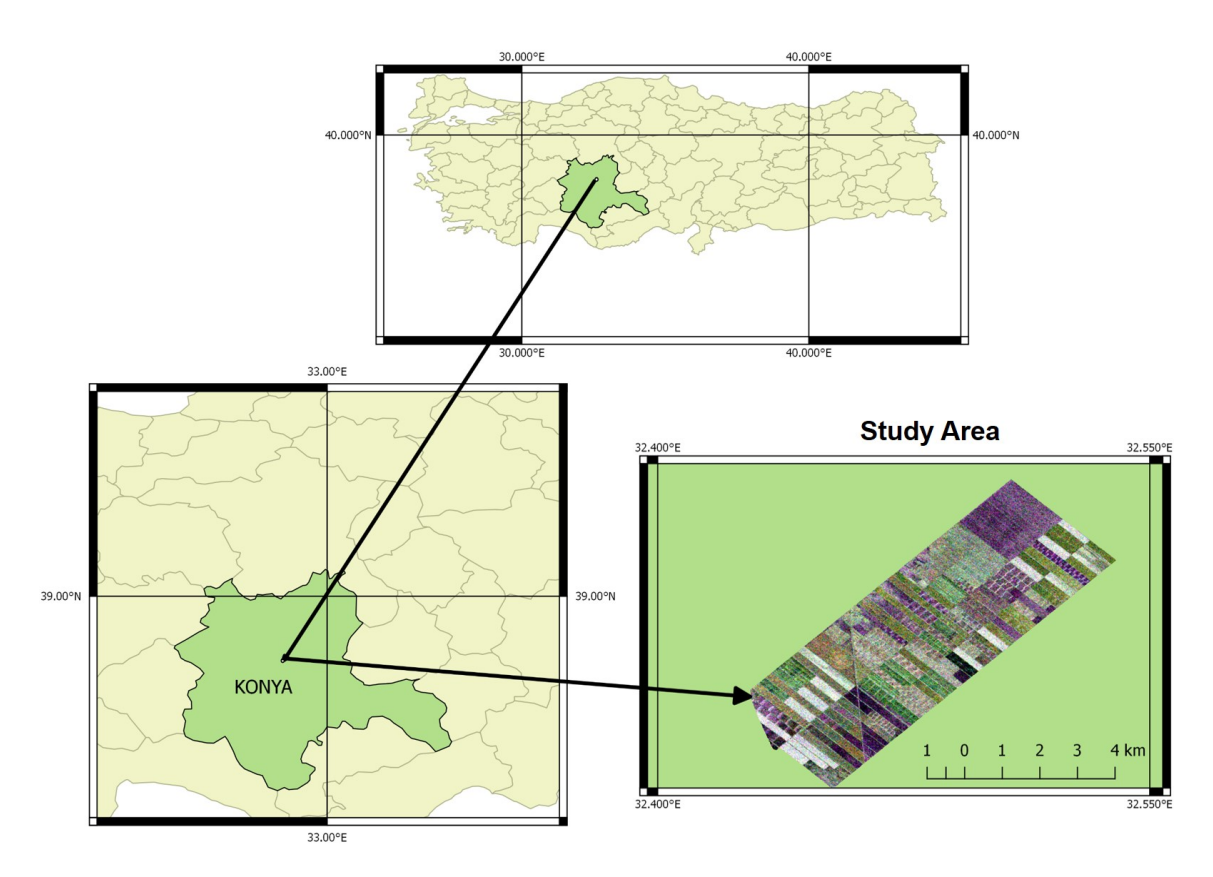


Figure 4.1 Study Area

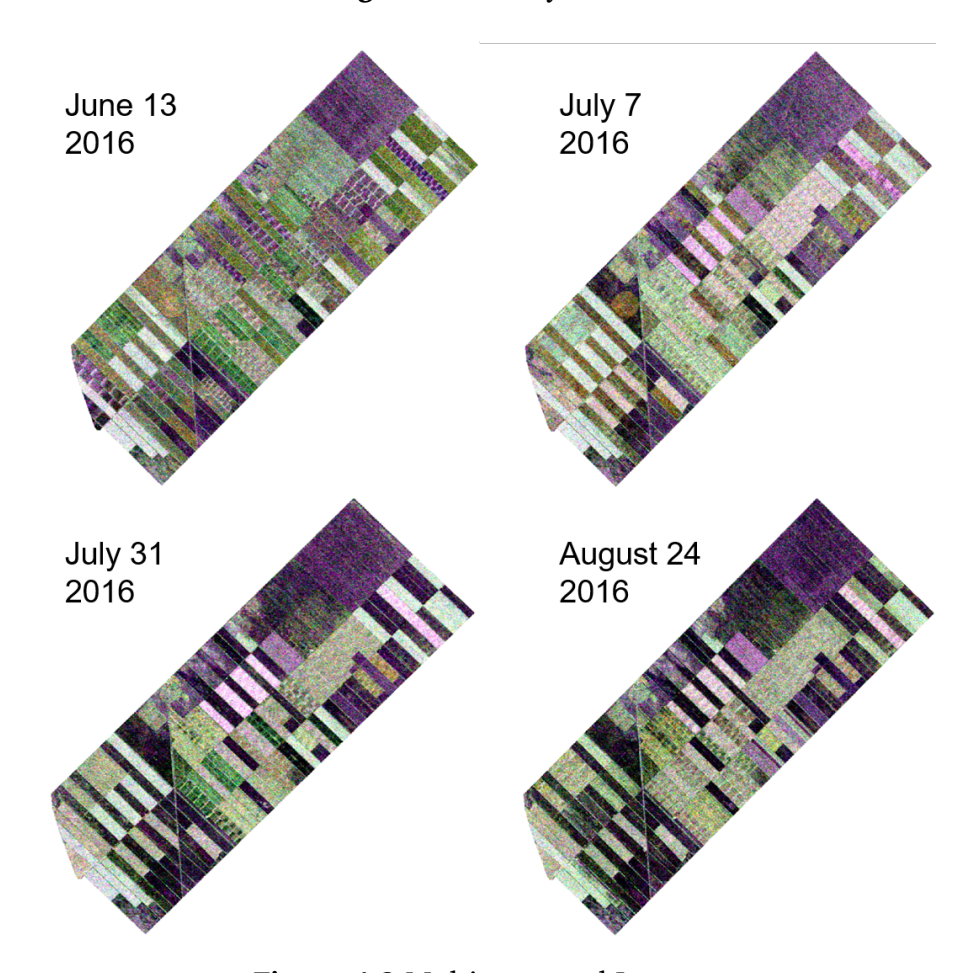


Figure 4.2 Multi-temporal Images

## 4.2 Experimental Design and Data Analysis

### 4.2.1 Data Pre-Processing

Typically, PolSAR images are served in a complex-valued data structure and need to be projected into the real domain (i.e. real-valued data) to be used as an input data for machine learning algorithm [104]. Within this thesis, the RADARSAT-2 data was pre-processed using the European Space Agency (ESA) Sentinels Application Platform (SNAP) software (v.6.0).

The workflow for the data pre-processing is illustrated in Figure 4.3.

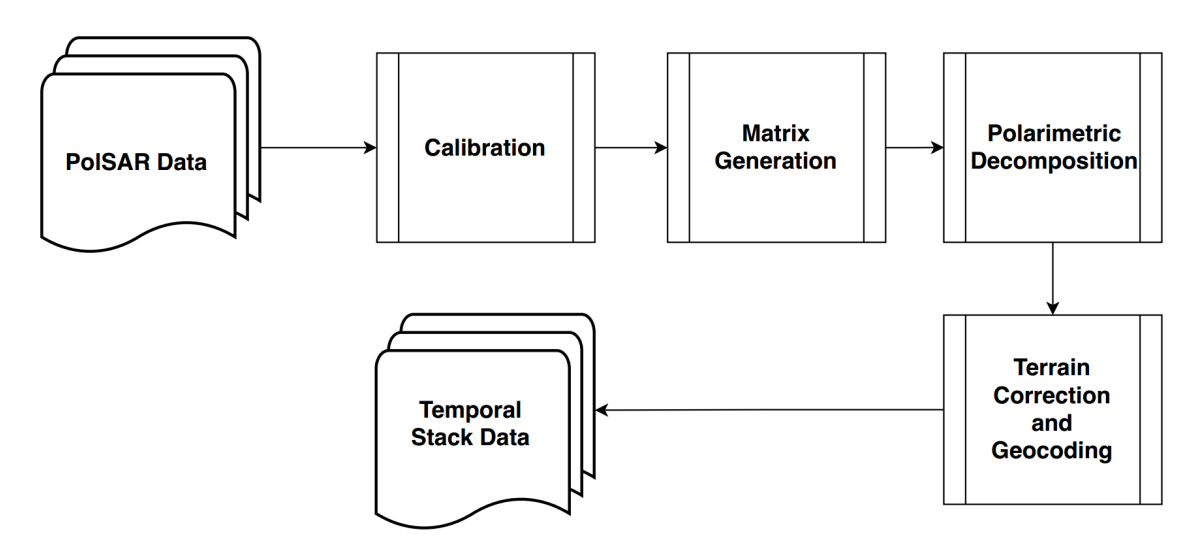


Figure 4.3 Data Pre-Processing

The data pre-processing steps were as follows:

- Radiometric calibration: Data calibration was performed using ESA SNAP software (v.6.0)
- Matrix generation: 3 × 3 coherency and covariance matrix were generated from 2 × 2 sinclair scattering matrix. In this formation, the window size was selected as 9.
- Extraction of polarimetric features: The incoherent polarimetric decompositions were generated from either coherency or covariance matrix. In this step, three polarimetric decomposition method were performed as follows: i) Cloude-Pottier, ii) Freeman-Durden and iii) Van Zyl
- Terrain correction and geocoding: Orthorectification was performed using the Range Doppler orthorectification method in SNAP. In this step, the Shuttle Radar Topography Mission (SRTM) data (~30 m resolution) was used as digital elevation model.

#### 4.2.2 Data Classification

In this thesis, three supervised machine learning algorithms (SVM, RF and LightGBM) have been used for classification of crops in the study area. SVM and RF are widely used in pattern recognition for classification and regression problems. Both method was implemented using an open-source Scikit-learn module in Python v3.6.4 [105–107]. LightGBM is a novel machine learning algorithm that has became popular in data science and computer vision. It has been the winning solutions in many machine learning competitions [92]. LightGBM was utilized via LightGBM Python Package v.2.2.2 [95].

There are five types of crops in the study area as follows: alfalfa, maize, potato, sunflower and wheat. The ground truth data (i.e. reference data) was collected on the acquisition date of per image and these data was recorded to be used in classification as well as accuracy assessment. The details of the reference data can be illustrated in Figure 4.4 and pixel information regarding the reference data is listed in Table 4.2.

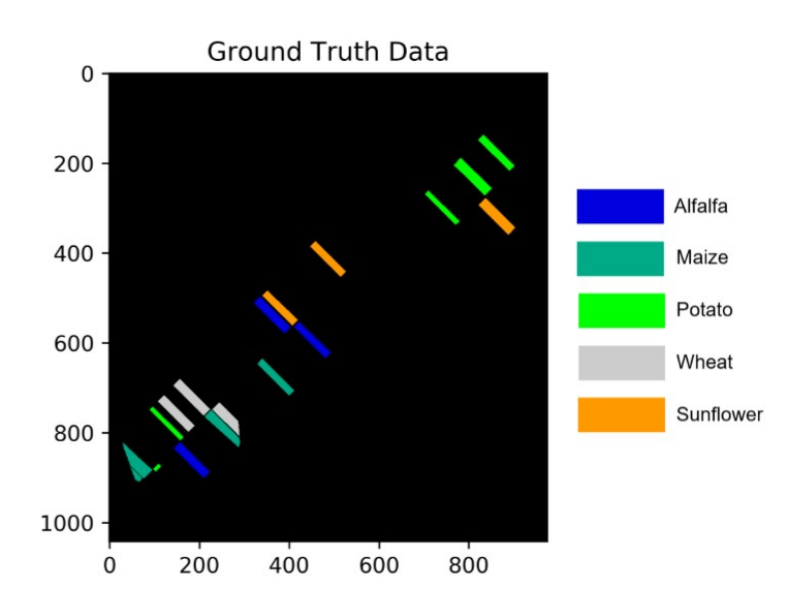


Figure 4.4 Ground Truth Data

Table 4.2 Ground Truth (Reference) Data

Class	Reference Data (pixel)
Alfalfa	5460
Maize	5581
Potato	6093
Sunflower	5361
Wheat	5481

The crop growth stages based on "Biologische Bundesanstalt, Bundessortenamt, and CHemische (BBCH)" scale was presented in Table 4.3.

Table 4.3 Ground Truth (Reference) Data

Dates	Crop Growth Stages
May 19 - June 12	leaf development
1 1 01 00	. 1
July 01-02	stem elongation
T 1 01	1 1.
July 31	heading
August 24 25	flaryanina
August 24-25	flowering

Data processing chart is provided in Figure 4.5.

## 4.2.3 Parameter Tuning for Classification Models

For all the classification models implemented in thesis, the parameter tuning is needed to maximize the capability of algorithm for classification in better accuracy. The main parameters of LightGBM, needed to be tuned, were set to the values as suggested on the parameter tuning (official) page of LightGBM [108] and the parameters were provided in Table 4.3.

For better accuracy in LightGBM model, it is suggested the use of bigger training data, small number of learning rate, large number of boosting iteration and large number of leaves in parameter tuning (official) page of LightGBM [108].

Table 4.4 LightGBM Parameters

Parameter	Value
Boosting type	GOSS
Number of leaves per tree	100
Learning rate	0.1
Maximum learning depth	5
Minimum number of data per in a leaf	20
Feature fraction	1.0
Bagging fraction	1.0
Number of boosting iteration	500

For RF, the number of trees and number for features were defined as 500 and 2, respectively.

In SVM classification, the RBF kernel was chosen and the parameters were optimized by using grid search. The two parameters needed to tuned for RBF kernel were regularization parameter (C) and kernel width ( $\gamma$ ). The optimum parameters were set to 500 and 3 for C and  $\gamma$ , respectively.

All experiments were performed on Python 3.6.4 through LightGBM Python Package [95] and an open-source Scikit-learn module [105–107].

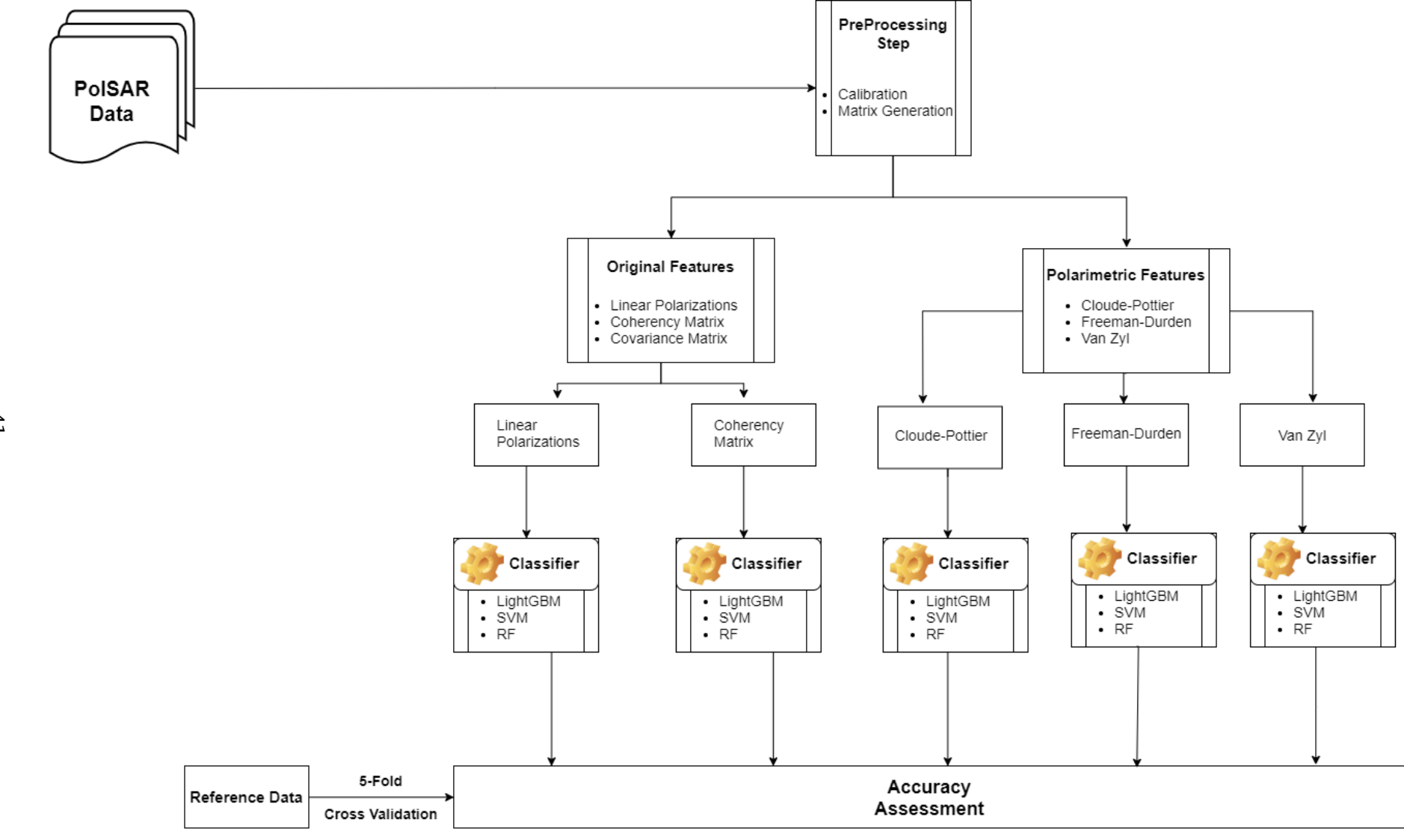


Figure 4.5 Data Processing

This section presents the experimental results, including overall accuracies (with standard deviation), kappa coefficients, class-based accuracy (based on F-scores). Before providing the classification results, the in-depth analysis of crops of how it characterizes or behaves in temporal domain was performed. To able to see the feature-based crop characterization in temporal domain would provide us the possible supporting (or underlying) reasons behind the classification results.

# 5.1 Temporal Analysis of Features for Crop

In this section, the in-depth analysis of crops of how it characterizes in temporal domain was performed. Within this scope, the following features were investigated for per crop type in temporal domain: Entropy/Anisotropy/Alpha Angle, linear polarizations(HH/HV/VV) and Surface/Double Bounce/Volume scattering

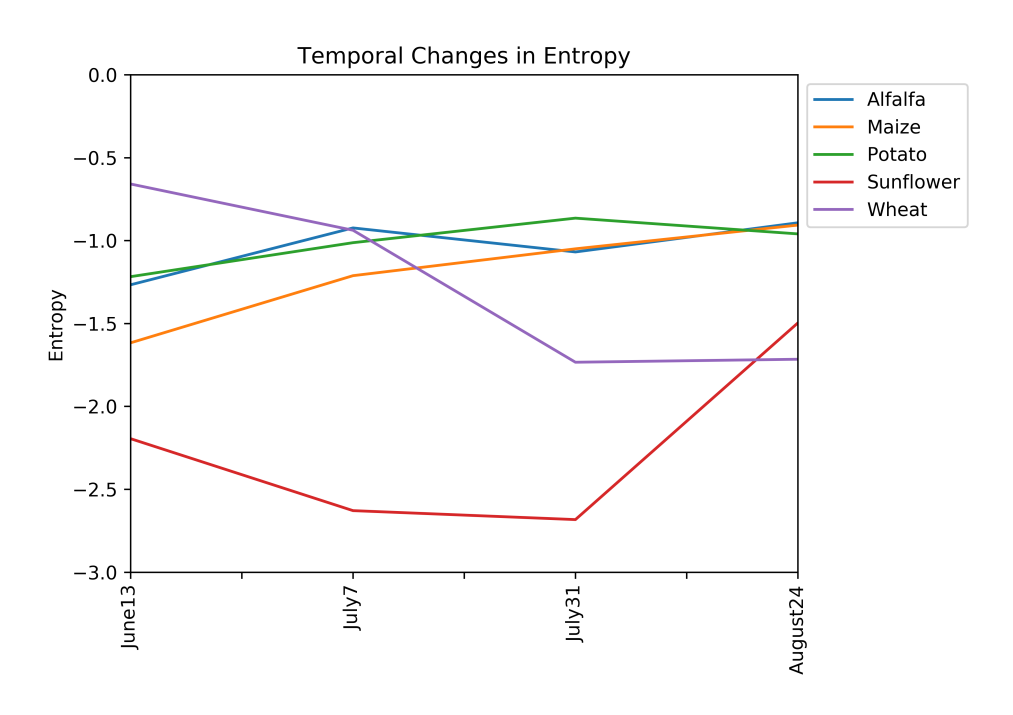


Figure 5.1 Temporal Changes in Entropy

The temporal crop characterization (i.e. changes in time) for Entropy can be seen in Figure 5.1. Entropy, which is obtained through Cloude-Pottier decomposition, provides the information for the degree of randomness for the scattering. It can be clearly seen that Sunflower and Wheat have different characteristic from other crops in temporal domain, which might lead to separation them from others in crop classification. It can also be seen that Maize and Potato have similar (very close) Entropy values to Alfalfa in flowering stage in August 24. Alfalfa also has close Entropy values to Potato in leaf development period in June. Such close values between Alfalfa and Maize/Potato might lead to class confusion in crop classifications. In this case, Alfalfa might not be distinguished from other crops in sufficient level in Entropy.

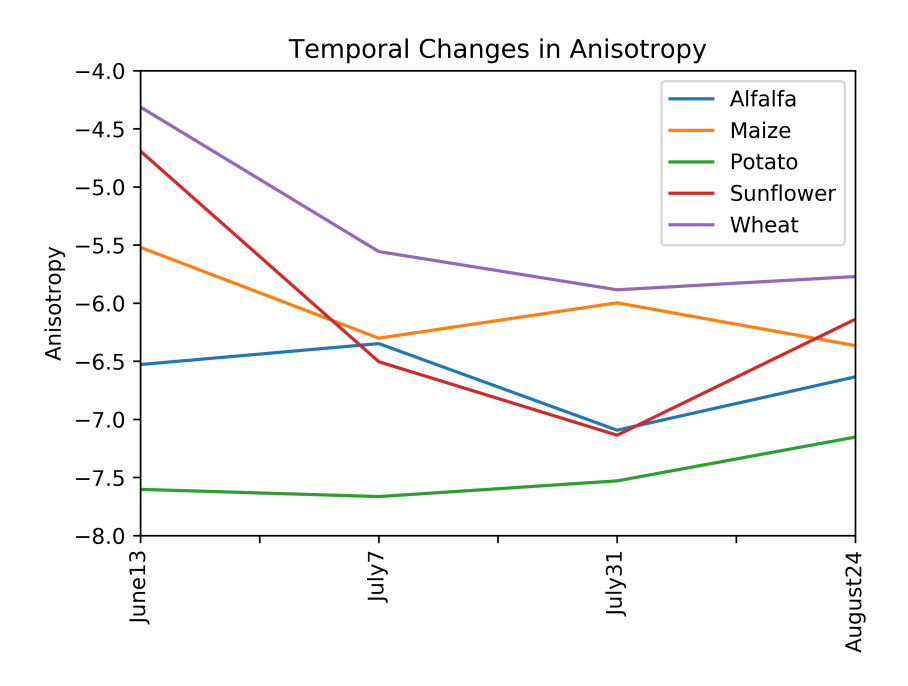


Figure 5.2 Temporal Changes in Anisotropy

In Figure 5.2, the temporal crop characteristics for Anisotropy was presented. Anisotropy provides the complementary information to the entropy and is an another feature obtained from Cloude-Pottier decomposition. When Figure 5.2 was examined, it is clearly seen that Wheat and Potato do not confuse with others and have completely different values than other three crop types. This might lead to accurate separation of these two crops from others in terms of crop classification.

As distinct from the Figure 5.1, Sunflower have similar values with Alfalfa in heading period (July 31) in Figure 5.2. Maize has also close values to Sunflower in the stem elongation period.

The temporal changes in crop characterization for alpha angle was provided in Figure 5.3. The alpha angle provides the information about the scattering types and in this case, all crops have surface scattering because all values are smaller than 30°. Maize, potato and alfalfa have very similar angles during the whole period while sunflower and wheat have different characteristics in temporal domain. Such different temporal characterization might lead to separation of sunflower and wheat from other three types of crops as well as confusion of maize and potato in terms of crop classification.

This graph also demonstrates that sunflower and wheat have different angles in their growth stages except flowering stage.

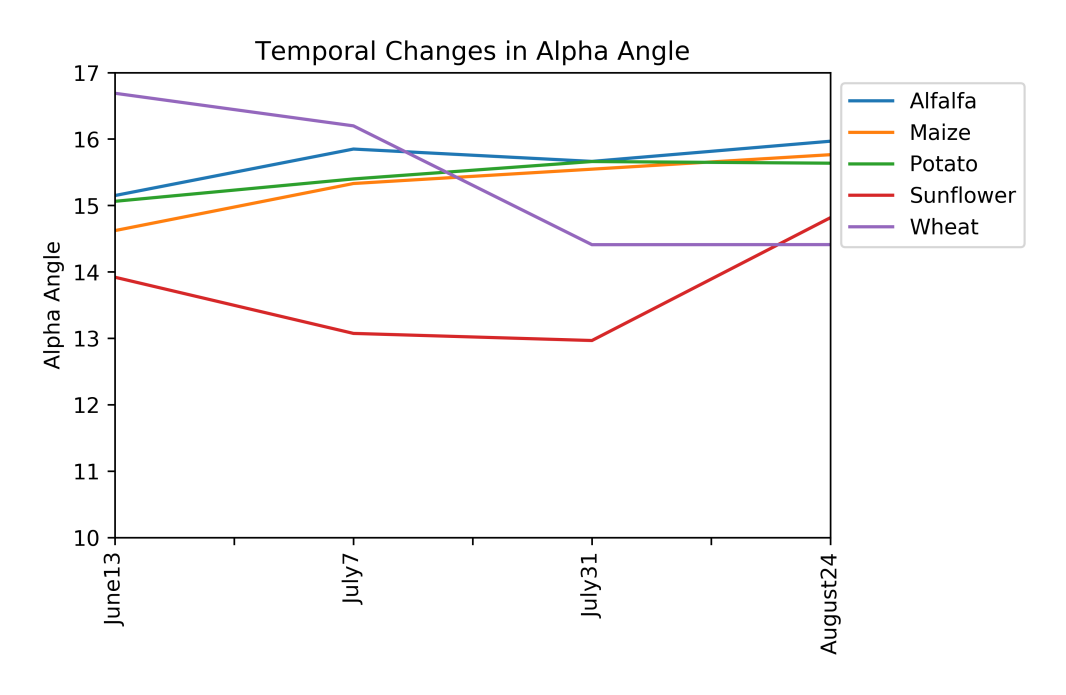


Figure 5.3 Temporal Changes in Alpha Angle

In Figure 5.4, the temporal crop characterization for HH polarization was presented. As similar to Figure 5.3, wheat and sunflower has different crop characteristics than other crop types especially in stem elongation and heading period, which might lead to greater separation of these two crop types than others. However, sunflower and wheat have same values in the leaf development stage (June 13), that might lead to class confusion and hence might be the reason of low classification accuracy.

Also the changes in backscatter values of sunflower and wheat in temporal domain are higher than other crops types, which is because of their behaviours (characteristics) from stem elongation to heading stage differ from others.

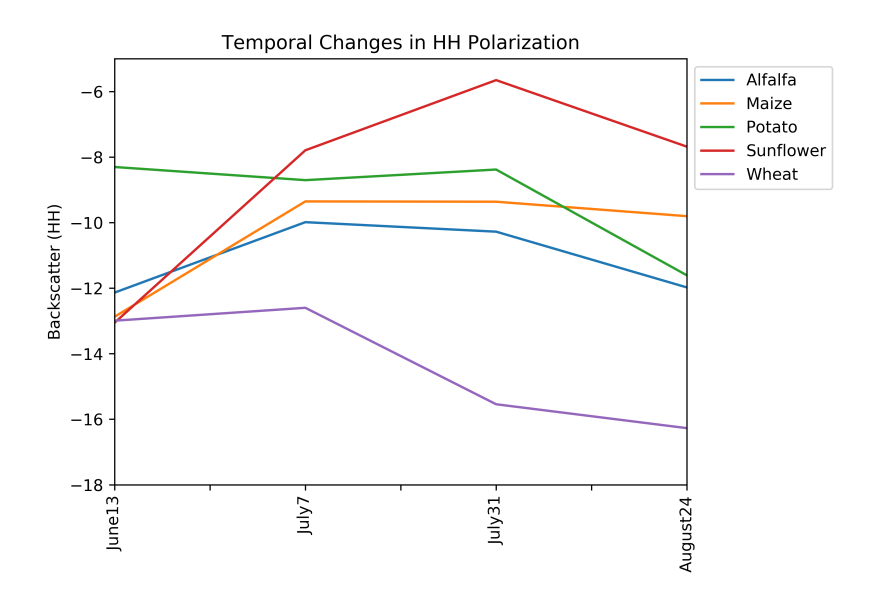


Figure 5.4 Temporal Changes in HH Polarization

The temporal changes of crops for HV polarization were demonstrated in Figure 5.5. For HV polarization, potato and wheat have very distinct behaviour in backscatter compared to other crop types, especially in stem elongation and heading stages. This distinct behaviour might help for the class separation of potato and wheat from each other as well as from other crop types.

Even though the temporal characteristics of maize and sunflower look different, they have similar backscatter values in growth stages like stem elongation and flowering, which might be the reason of the confusion between maize and potato.

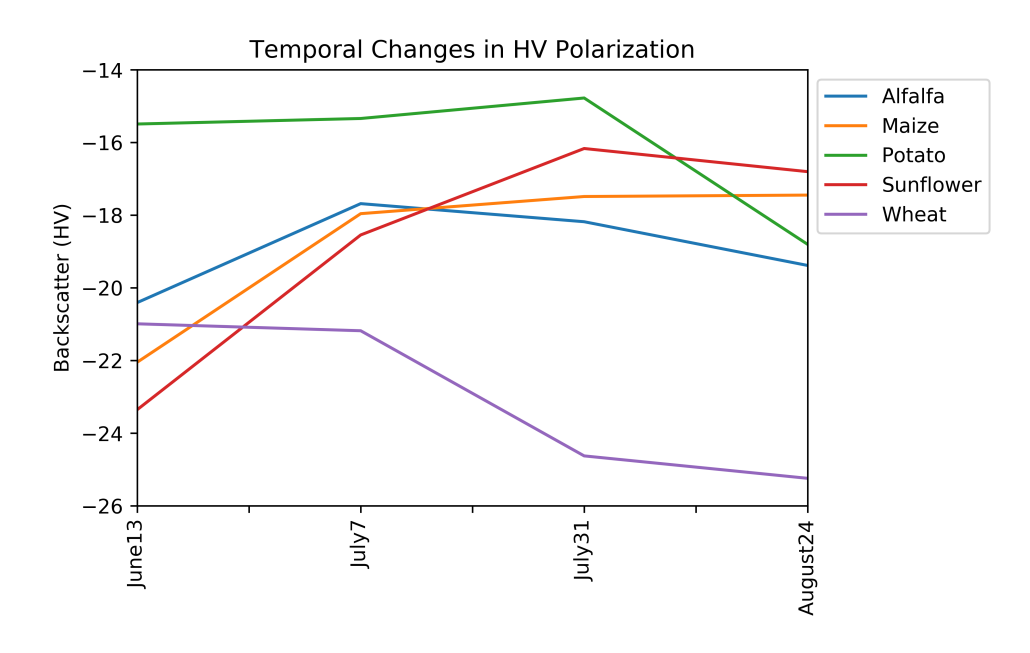


Figure 5.5 Temporal Changes in HV Polarization

In Figure 5.6, the temporal crop characterization for VV polarization was provided. VV polarization backscatter values almost provided similar trend like HH polarization for crops in temporal domain, especially for wheat, sunflower and potato. These three types of crops distinguish from each other in terms of their dynamics as well as backscatter values in VV polarization. Such different crop characterization might lead to obtain high accuracy in crop classification. However all crop types, except potato, have very close backscatter values in leaf development stage

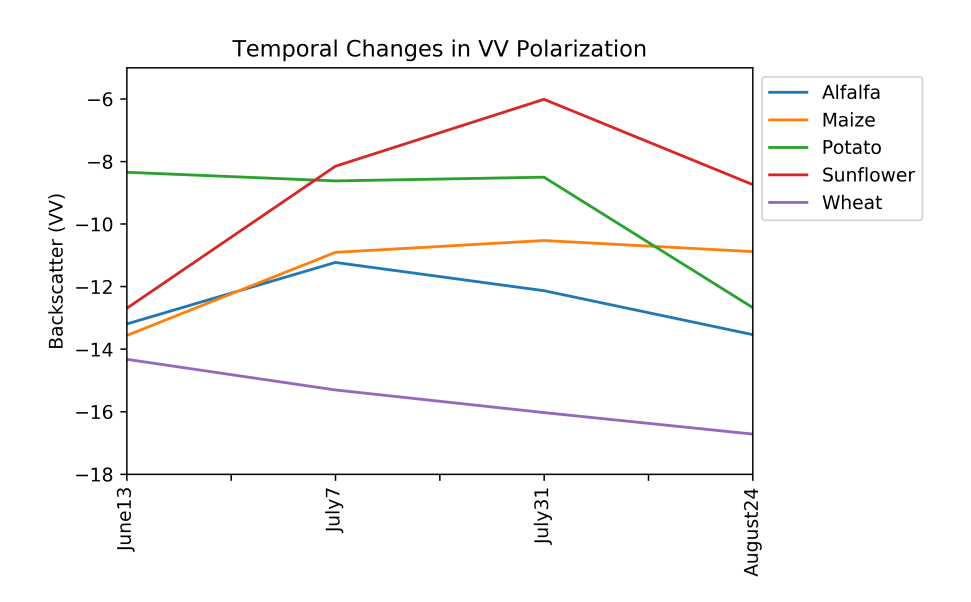


Figure 5.6 Temporal Changes in VV Polarization

Both Freeman-Durden decomposition and Van Zyl decomposition produce the same polarimetric outputs (surface, double bounce and volume scattering) and therefore each polarimetric feature for both decomposition was interpreted together with providing the important differences. The original values were multiplied by 100 for better visual comparison.

The temporal crop characterizations for surface scattering of Freeman-Durden and Van Zyl decomposition was provided in Figure 5.7. It can be simply seen that, crops have almost similar temporal characterization in both graph, except maize. For this exception, we can easily deduce that Van Zyl decomposition might differ from Freeman-Durden for some particular cases in surface scattering.

Sunflower has sharp increase in surface scattering in leaf development stage to heading stage, that might provide the good separation of sunflower from other classes. Also in temporal domain, each crop type has different dynamics that might lead to good separation in terms of crop classification.

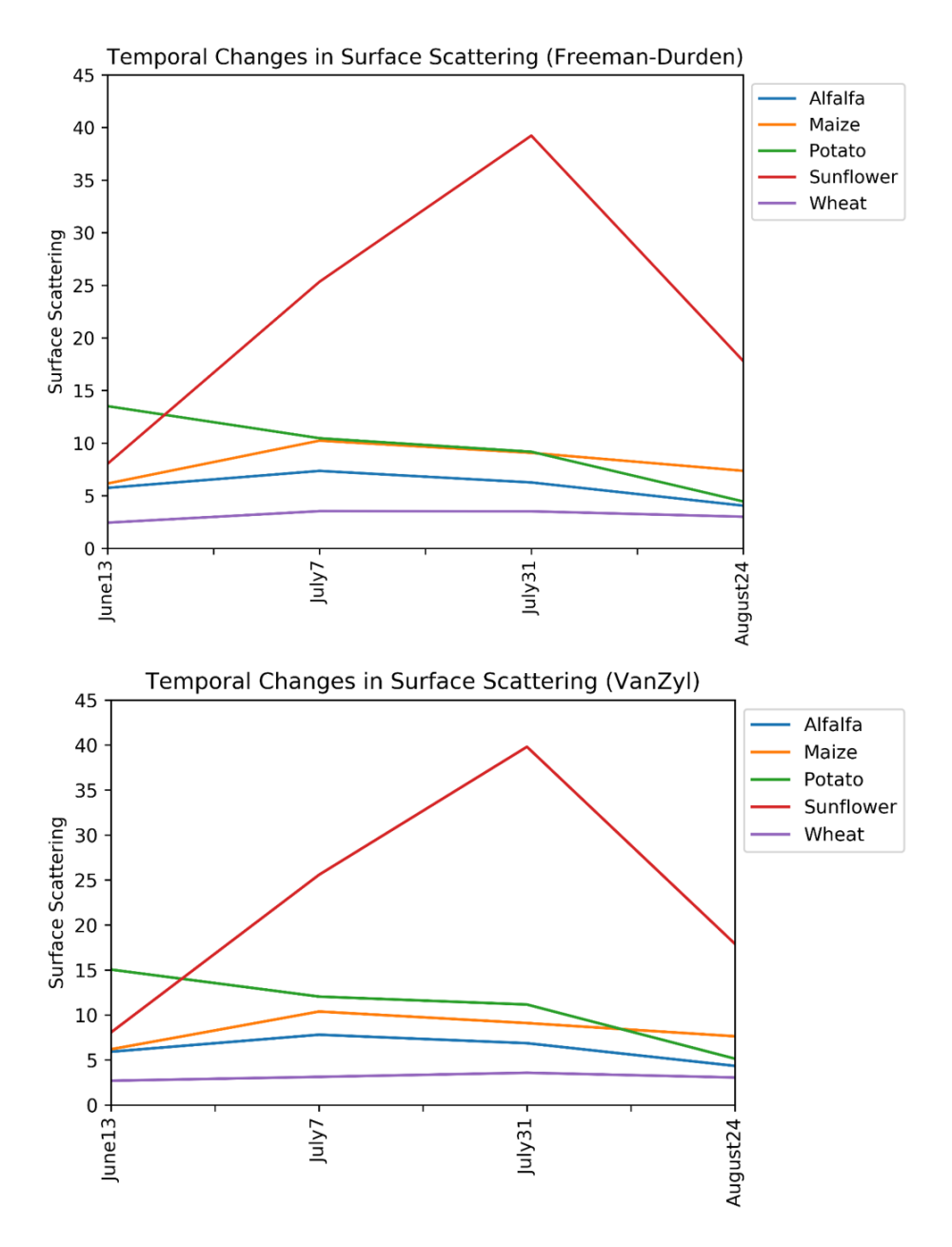


Figure 5.7 Temporal Changes in Surface Scattering

Figure 5.8 demonstrates the temporal changes in double-bounce scattering for per crop type. Except alfalfa which does not have any phenological stage, all crop type has similar temporal trend or dynamics in both Freeman-Durden or Van Zyl decomposition. Different from surface scattering, wheat has the critical changes (i.e sharp decline) in double-bounce scattering, that can help the good separation of wheat from other crops. Maize also might be easily distinguished from other classes in double-bounce scattering as it has a relatively sharp increase from stem elongation stage to heading stage in double-bounce.

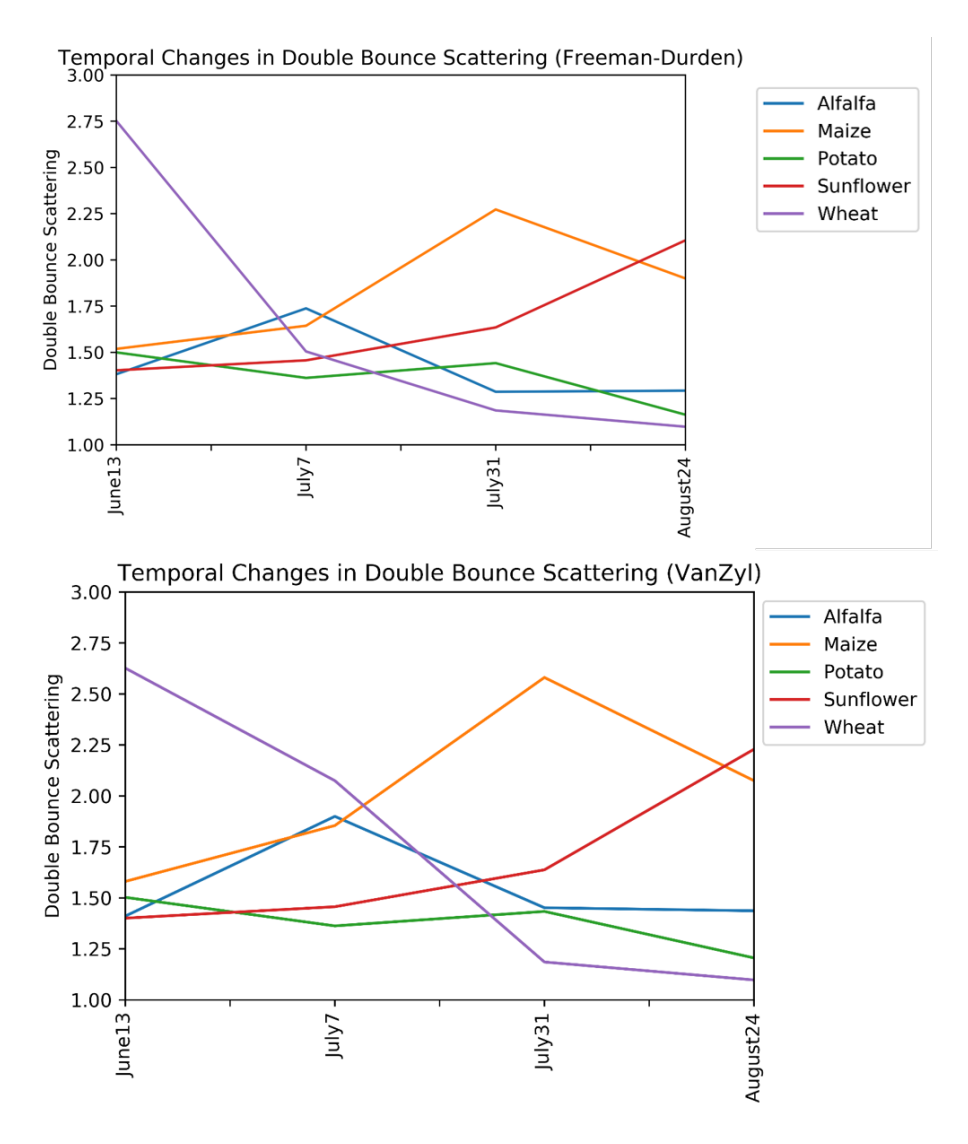


Figure 5.8 Temporal Changes in Double Bounce Scattering

Figure 5.9 illustrates the temporal changes in volume scattering for per crop type in both Freeman-Durden or Van Zyl decomposition. Different from the surface and volume scattering, potato has the critical changes (sharp decline) in volume scattering, that can help the good separation of potato from other crops. Sunflower might also be easily distinguished from other classes in volume scattering as it has a relatively sharp increase from stem elongation stage to heading stage. Wheat has also low volume scattering compared to other crops, which might lead to better discrimination of it from other classes.

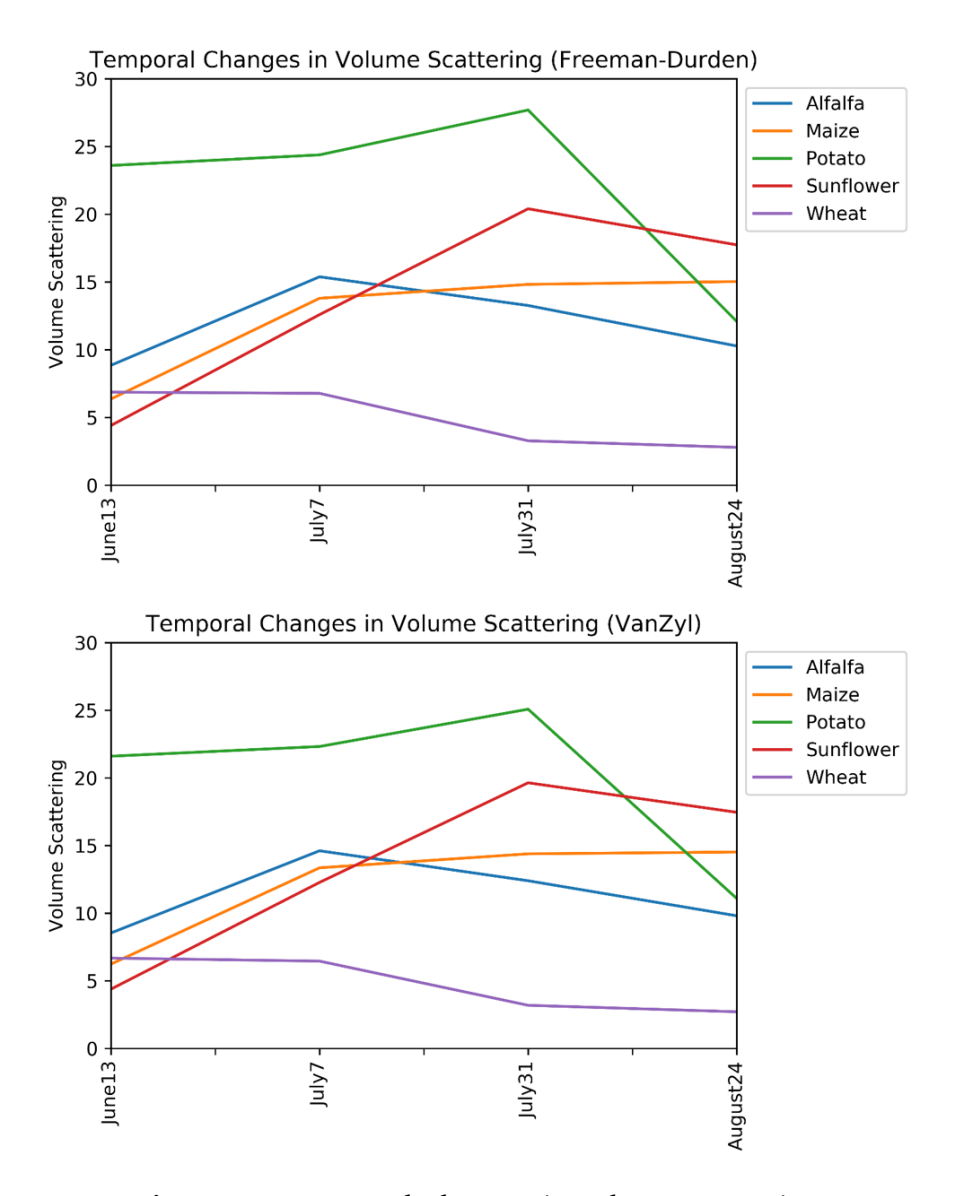


Figure 5.9 Temporal Changes in Volume Scattering

### 5.2 Classification Results

Figure 5.10 illustrates the overall accuracies (cross-validation scores) of five different features for per classification model from multi-temporal data. The highest classification accuracy was achieved by LightGBM with Van Zyl decomposition and Freeman-Durden decomposition while the lowest classification accuracy was produced by RF with Coherency matrix.

This is because sunflower, wheat and potato have sharp changes in temporal domain for surface (Figure 5.7), double-bounce (Figure 5.8) and volume scattering (Figure 5.9), respectively. Such critical changes lead to better crop discrimination and hence yielding the higher classification accuracy compared to other features. These three polarimetric features are the elements of both Freeman-Durden decomposition and

Van Zyl decomposition.

This mean value of overall accuracy is the results from the 5-fold cross validation.

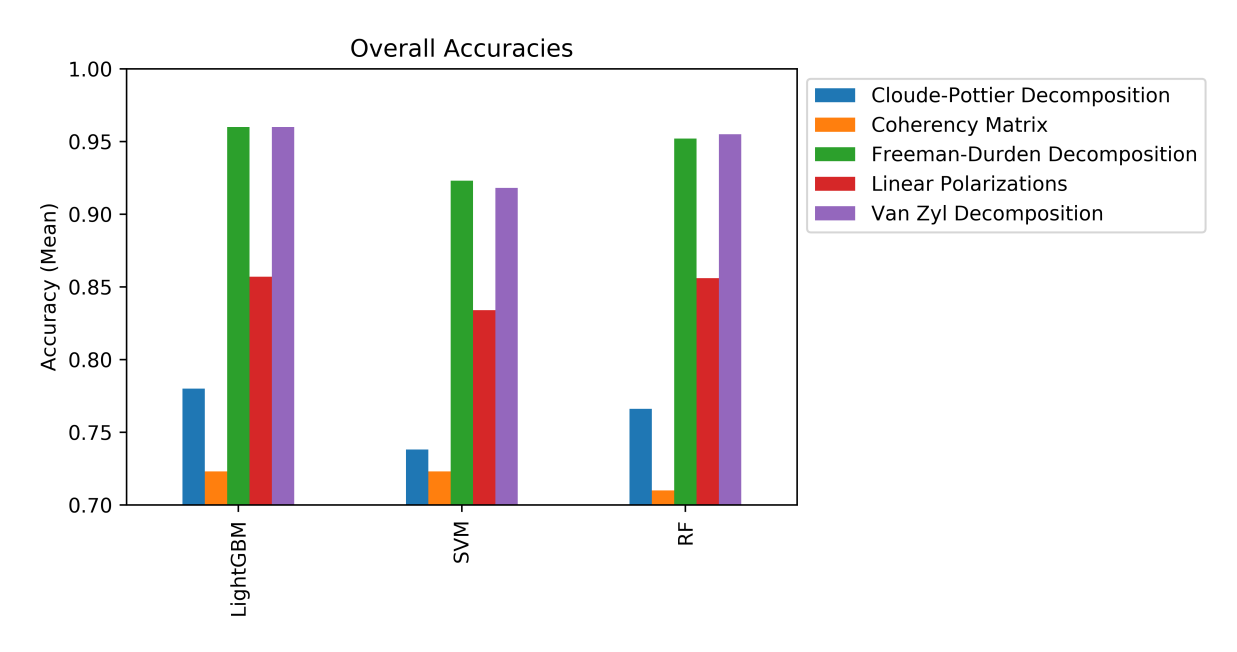


Figure 5.10 Overall Accuracy

Both Van Zyl decomposition and Freeman-Durden decomposition produced the highest overall classification accuracy (0.960) through LightGBM and followed by Van Zyl decomposition with RF (0.955), Freeman-Durden decomposition with RF (0.952) and Freeman-Durden decomposition with SVM (0.923). Though the same features and reference data are used, the classification accuracies differ from each other. This is because each classification model has different sensitivity to the data in supervised learning process as well as uses different decision rule.

The differences between two classification within statistical significance was evaluated by utilizing McNemar's test. All the differences between two competitive results were found statistically significant based on  $(\chi^2)$  value. The  $(\chi^2)$  values are presented in Table 5.1. The overall accuracies with standard deviation for per feature were illustrated in Figure 5.11. The black line on the bar denotes the range between maximum and minimum value within overall accuracy in cross validation scores.

**Table 5.1** McNemar's Test  $(\chi^2)$  values

Classification	$\chi^2$ value
Van Zyl (LightGBM-RF)	30.37
Freeman-Durden (LightGBM-RF)	66.45
Freeman-Durden (RF-SVM)	385.27

When overall accuracies with standard deviation in Figure 5.11 were examined, it can be concluded that LightGBM is the most robust classification model with an exception

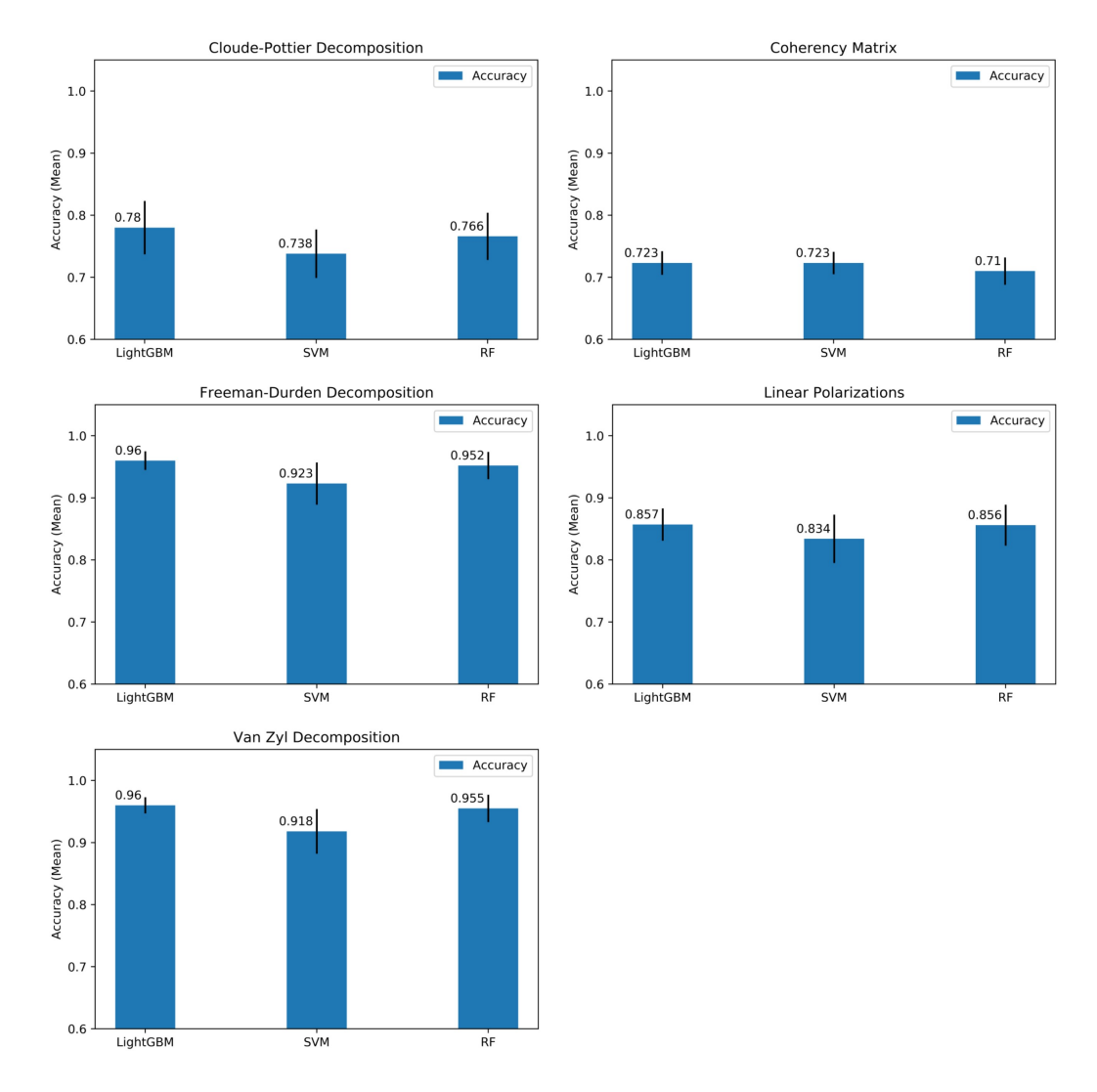


Figure 5.11 Accuracies with Standart Deviation

of the Cloude-Pottier decomposition. The robustness means here the low value of standard deviation. In other words, the classification results are not much affected from the different iteration during 5-fold cross validation. Among the features, the highest three values of standard deviation were received from Cloude-Pottier decomposition by LightGBM ( $\pm 0.043$ ), SVM ( $\pm 0.039$ ) and RF ( $\pm 0.038$ ). These values mean that the classifiers are more sensitive and much affected from the displacement of training data (during k-fold cross validation) when using the Cloude-Pottier decomposition than other features.

As similar to overall accuracy, the top five classification results are in the same order (ranking) in kappa coefficients for this experiment. Both Van Zyl decomposition and Freeman-Durden decomposition produced the highest overall classification accuracy (0.950) through LightGBM and followed by Van Zyl decomposition with RF (0.944), Freeman-Durden decomposition with RF (0.939) and Freeman-Durden decomposition with SVM (0.904). Figure 5.12 illustrates the (mean) kappa coefficients of five

different features for per classification model from multi-temporal data.

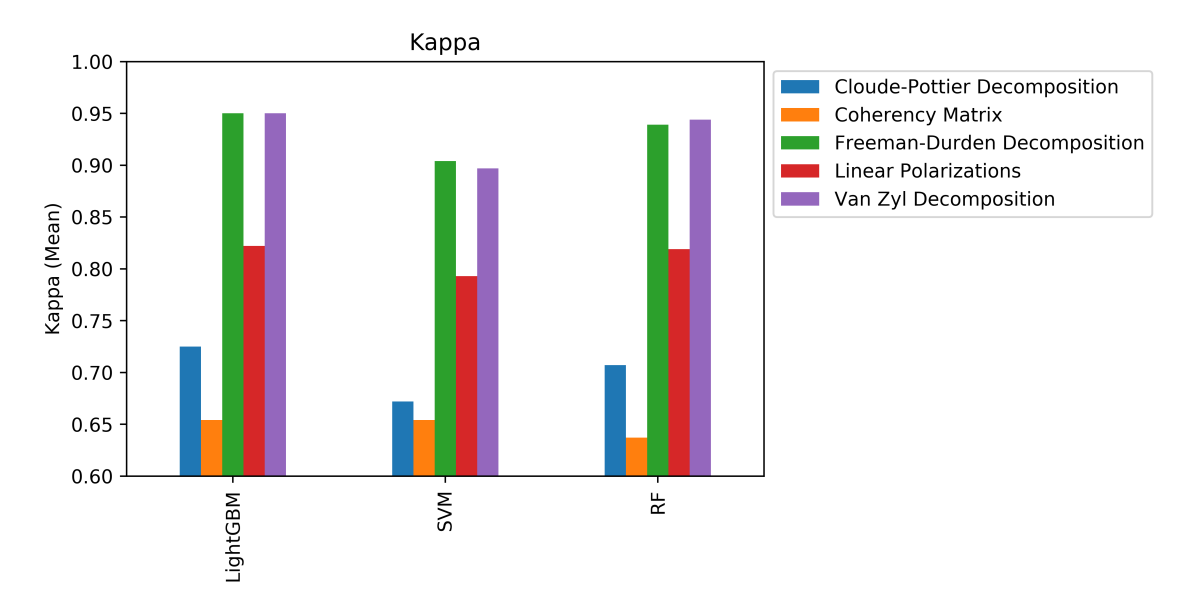


Figure 5.12 Kappa Coefficients

When kappa coefficients with standard deviation in Figure 5.13 were examined, it can be concluded that LightGBM is the most robust classification model with an exception of the Cloude-Pottier decomposition as similar to overall accuracies with standard deviation illustrated in Figure 5.11. Among the features, the highest three values of standard deviation were received from Cloude-Pottier decomposition by LightGBM ( $\pm 0.053$ ), SVM ( $\pm 0.049$ ) and RF ( $\pm 0.049$ ). These values mean that the classifiers are more sensitive and much affected from the displacement of training data when using the Cloude-Pottier decomposition than other features.

The McNemar's test results are presented in the tables in Appendix A to analyse the differences between two classification (in a case of where two classification produced competitive accuracies) in terms of statistical significance. Only in two cases, the differences between two classification are found statistically non-significant.

**Table 5.2** McNemar's Test  $(\chi^2)$  values

Classification	$\chi^2$ value
Coherency Matrix (LightGBM-SVM)	0.0002
Linear Polarizations (LightGBM-RF)	1.68

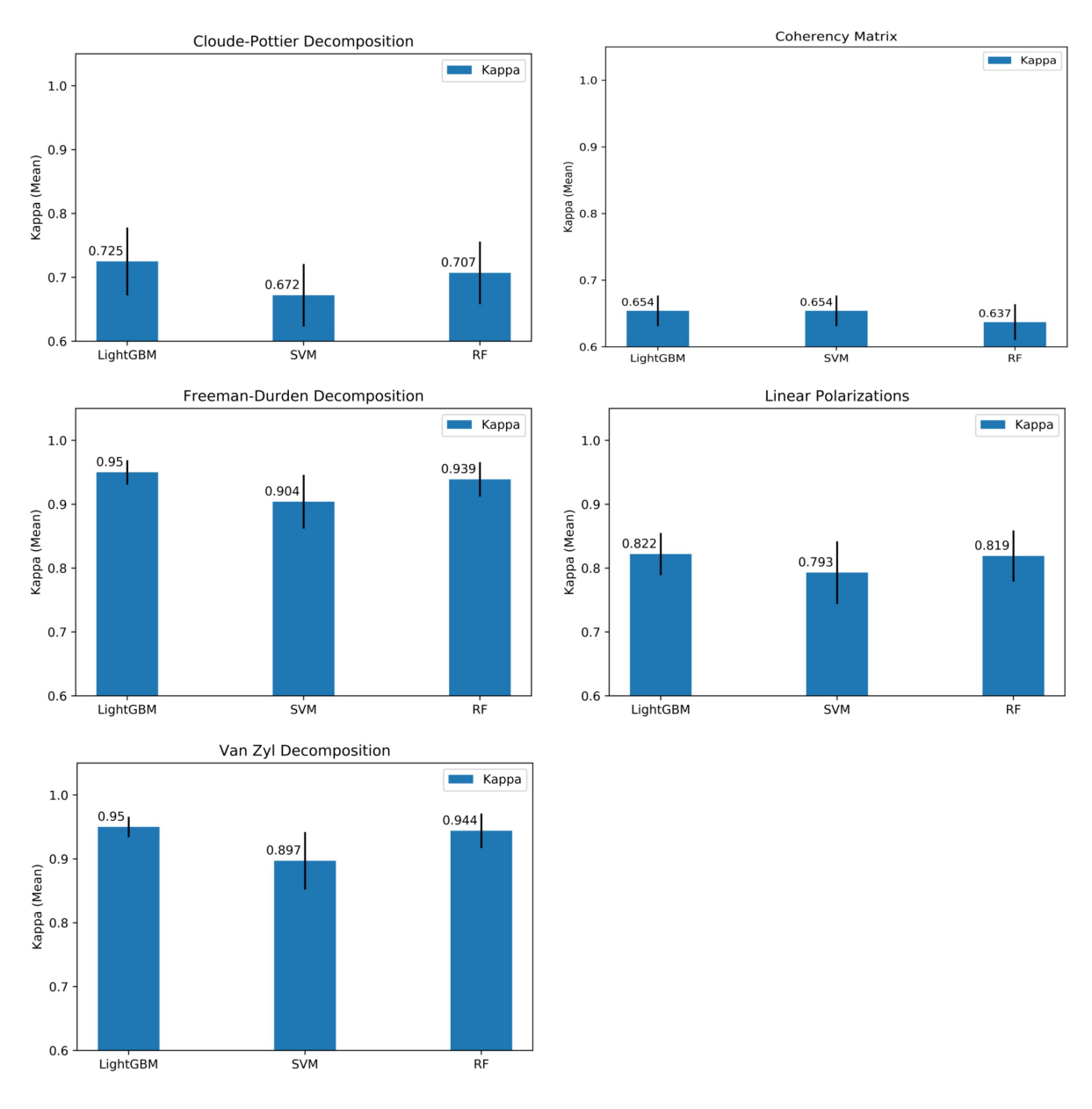


Figure 5.13 Kappa Coefficients with Standart Deviations

## 5.3 Evaluation of Computational Costs

Besides the comparison of overall accuracies, the computation times of the training process for models as well as features were calculated and compared with each other. Computational costs such as training speed or optimization of model parameters in machine learning are also another important criteria on to choose the classification model as well as to evaluate the classification performance. In some cases, there is a trade-off computational efficiency and overall performance (accuracy). In fact, the computation time for machine learning algorithms in terms of classification and regression is heavily depending on how the algorithm is well-adapted (how well of train data represent the land cover) to the input imagery as well as the characteristic features of the classification model (i.e. ensemble learning, max-margin based models, decision tree based models etc.). All experiments were performed on Python 3.6.4 in a computer whose technical specifications are provided in Table 5.3. Table 5.4 demonstrates the training times (in seconds) for LightGBM, RF and SVM for per feature.

**Table 5.3** Computer Specifications

Specifications	Details
Processor	Intel(R) Core(TM) i7-7700K
RAM	64 GB
Processor Base Frequency	4.20 GHz
Operating System	Windows Server 2016 (64-Bit)

**Table 5.4** CPU running times for training process (in seconds)

	LightGBM	SVM	RF
Linear Polarizations	3.32	31.04	31.20
Coherency Matrix	3.89	16.17	65.30
Cloude-Pottier Decomposition	2.87	42.04	28.17
Freeman-Durden Decomposition	1.87	1.44	19.17
Van Zyl Decomposition	1.91	1.32	20.23

For linear polarizations, coherency matrix and Cloude-Pottier decomposition, the LightGBM is much faster (almost ten times) than RF and SVM, which is as expected. However for the Freeman-Durden and Van Zyl decomposition, SVM is slightly faster than LightGBM in terms of training time (in the milliseconds level).

# 5.4 F-scores for per model

In this subsection, the F-scores of classes for per classification model are presented in Fig 5.14, Fig 5.15 and Fig 5.16 for LightGBM, RF and SVM, respectively.

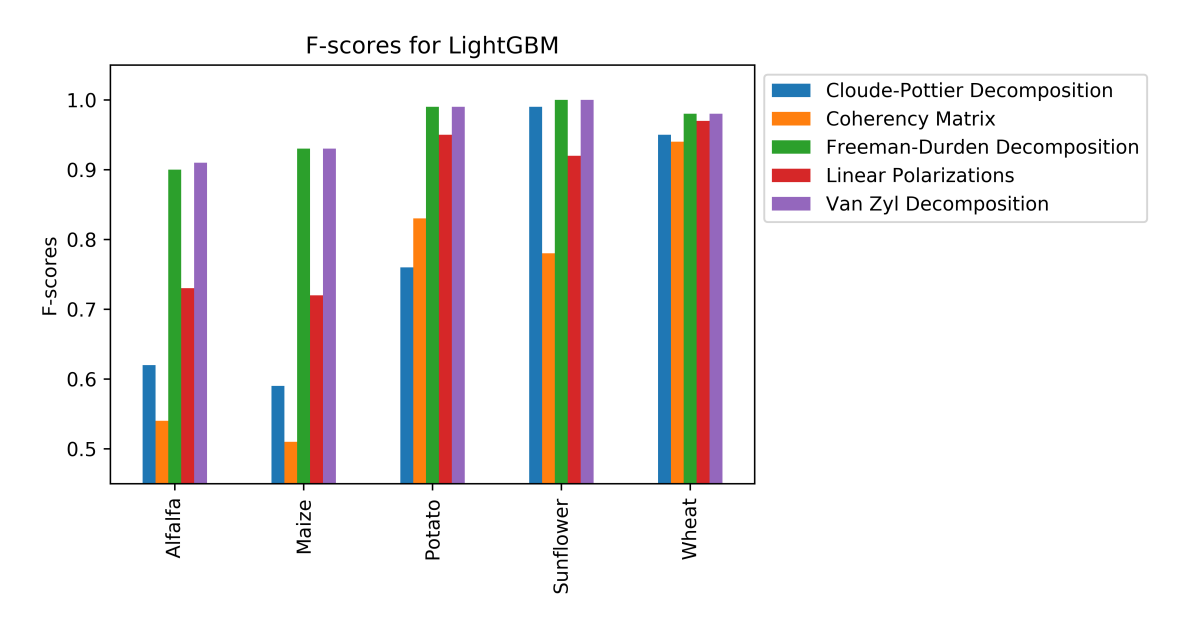


Figure 5.14 F-scores for LightGBM

Freeman-Durden and Van Zyl decomposition with LightGBM classified every class with higher than 0.90, as illustrated in Figure 5.14. The highest score was received for the sunflower as 1.00 from Freeman-Durden and Van Zyl. This is because sunflower has high scattering values in surface, double-bounce and volume scattering as well as sharp changes in surface scattering from leaf development stage to heading stage.

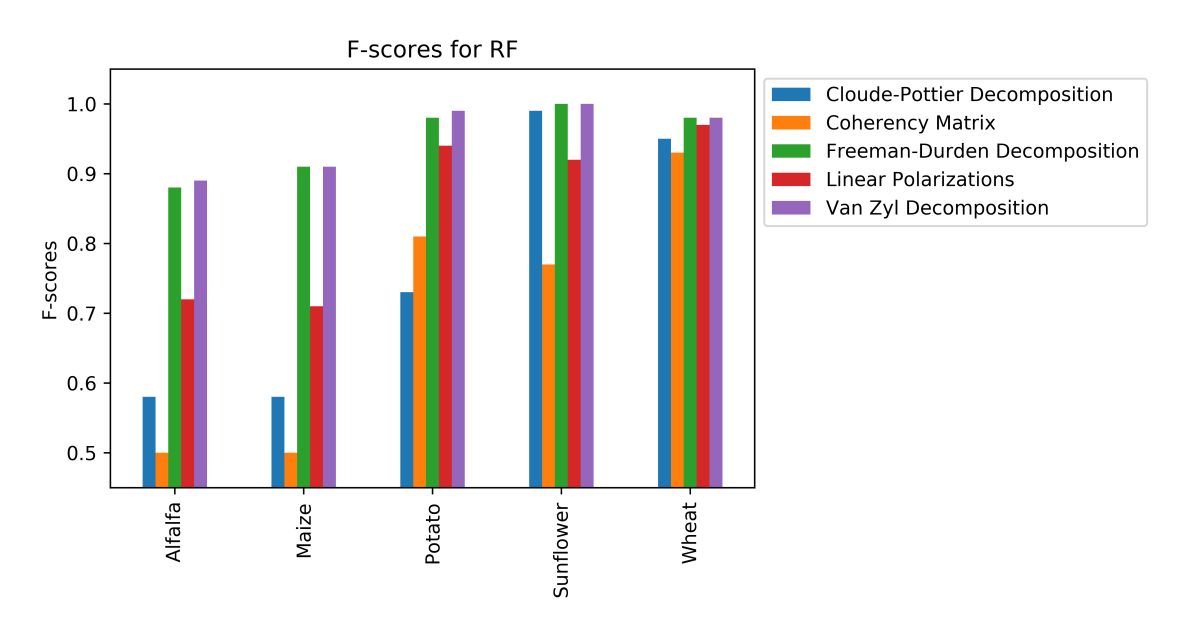


Figure 5.15 F-scores for RF

Such differences compared to other crops lead to higher F-score for sunflower than

others for LightGBM, which also applies for SVM and RF as well. The coherency matrix produced the lowest scores for maize as 0.51 and for alfalfa as 0.54 by LightGBM where maize was misclassified as alfalfa and vice versa.

As similar to LightGBM, Freeman-Durden and Van Zyl decomposition with RF classified every class with higher than 0.90 with an exception of alfalfa. The highest score was received by Freeman-Durden and Van Zyl as 1.00 for sunflower while lowest score was produced by coherency matrix as 0.50 for maize and alfalfa, as illustrated in Figure 5.15

SVM also showed similar tendency to RF for all classes, as illustrated in Figure 5.16.

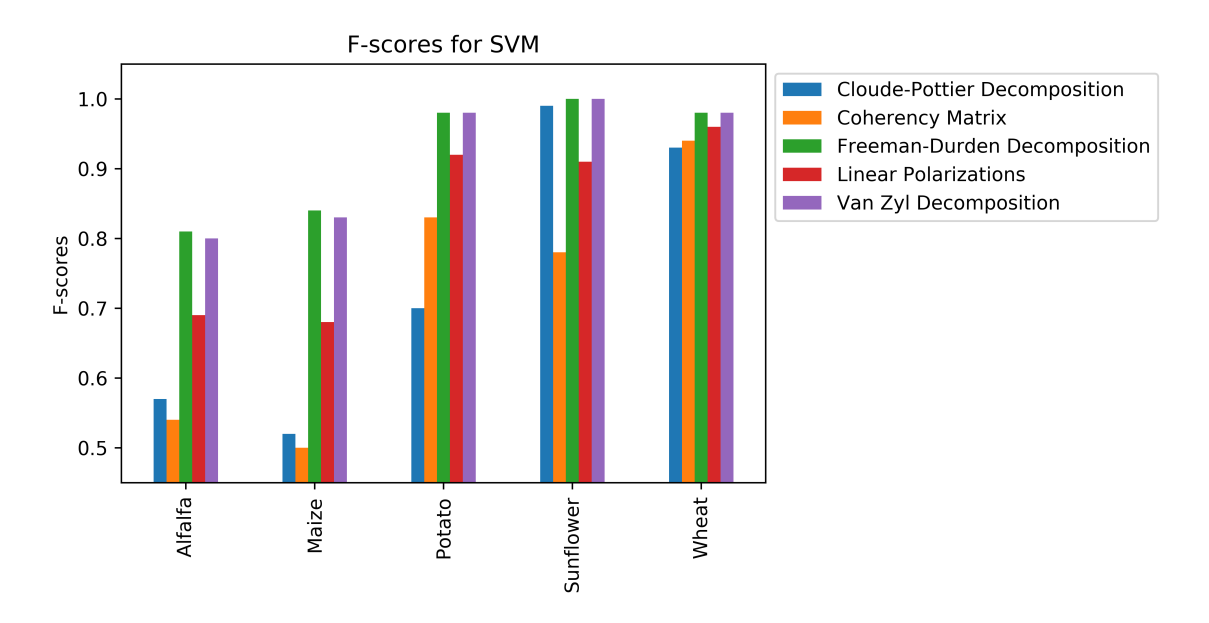


Figure 5.16 F-scores for SVM

## 5.5 Class-based Accuracy Assessment

The class-based performance was assessed using F-score which is the harmonic mean of precision and recall values. In the following subsections, the F-scores were presented for per crop category as well as for each features. All comparison regarding class-based performances will be based on F-score in the following subsections.

### 5.5.1 Alfalfa

For all features as well as for each classification model, alfalfa was classified higher than 0.49 F-scores. Van Zyl decomposition with LightGBM produced the highest score (0.91) while Coherency matrix by RF produced the lowest score (0.50) for alfalfa, as illustrated in Figure 5.17.

Alfalfa has not much critical changes on surface scattering in temporal domain and obviously be distinguished from others, as illustrated in Figure 5.7. However for double-bounce and volume scattering, alfalfa is crossed with maize and this leads to class confusion between maize and alfalfa.

Van Zyl decomposition with LightGBM produced the highest score (0.91) and followed by Freeman-Durden decomposition with LightGBM (0.90), Van Zyl decomposition with RF (0.89), Freeman-Durden decomposition with RF (0.88) and Freeman-Durden decomposition with SVM (0.81). The alfalfa was mixed with maize for per feature and therefore, in some percentage, incorrectly classified as maize, listed in confusion matrices in Appendix-A.

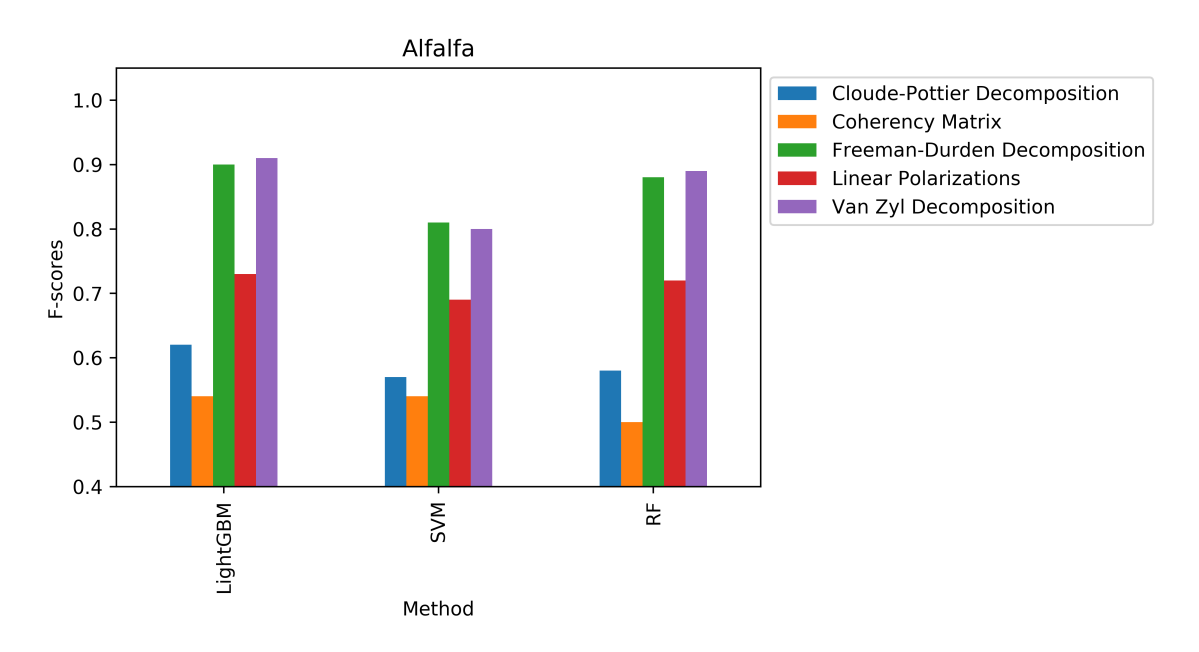


Figure 5.17 F-scores for Alfalfa

When Figure 5.17 was examined, it can be deduced that polarimetric features with an exception of Cloude-Pottier decomposition produced higher score than original features (i.e. coherency matrix and linear polarizations) for the identification of alfalfa. When Figure 5.1 was examined, it can be obviously seen that Maize and Potato in flowering stage have similar (very close) Entropy values to alfalfa. Such close values between alfalfa and maize leads to class confusion for Cloude-Pottier decomposition.

Among inter-comparison of decomposition methods in terms of F-score for alfalfa, Van Zyl decomposition outperformed Cloude-Pottier and Freeman-Durden decomposition with an exception of SVM where Freeman-Durden decomposition achieved the score as 0.81.

#### **5.5.2** Maize

Maize was classified higher than 0.49 F-scores for all features. Van Zyl decomposition and Freeman-Durden decomposition with LightGBM produced the highest score (0.93) while Coherency matrix by RF and SVM produced the lowest score (0.50) for maize, as illustrated in Figure 5.18. Van Zyl decomposition with LightGBM and Freeman-Durden decomposition with LightGBM produced the highest score (0.93) and followed by Van Zyl decomposition with RF (0.91), Freeman-Durden decomposition with RF (0.91) and Freeman-Durden decomposition with SVM (0.81).

When Figure 5.1 was examined, it can be obviously seen that Maize and Potato in flowering stage have similar (very close) Entropy values to alfalfa. Such close values between maize and alfalfa leads to class confusion for Cloude-Pottier decomposition. The maize was mixed with alfalfa for per feature and therefore, in some percentage incorrectly classified as alfalfa, listed in confusion matrices in Appendix-A as well as illustrated in Figure 5.1, Figure 5.3 and Figure 5.6

When Figure 5.18 was examined, it can be seen that polarimetric features with an exception of Cloude-Pottier decomposition produced higher score than original features (i.e. coherency matrix and linear polarizations) for the identification/classification of maize. The underlying reason of this exception for Cloude-Pottier decomposition was explained in previous paragraph. Within intercomparison of decomposition methods in terms of F-score for maize, Van Zyl decomposition produced the equal scores with Freeman-Durden decomposition with an exception of SVM. Coherency matrix produced lowest scores for maize among decomposition methods.

## **5.5.3** Potato

Potato was classified higher than 0.69 F-scores for all features. Van Zyl and Freeman-Durden decomposition with LightGBM and Van Zyl decomposition with RF produced the highest score (0.99) while Cloude-Pottier decomposition with SVM produced the lowest score (0.70) for potato, as illustrated in Figure 5.19. Van Zyl and Freeman-Durden decomposition with LightGBM and Van Zyl decomposition with RF produced the highest score (0.99) and followed by Freeman-Durden decomposition with RF (0.98) and Van Zyl decomposition with SVM (0.98).

Potato has the critical changes (sharp decline) in volume scattering and distinguishable trend in temporal domain for surface scattering, that lead to good separation of potato from other crops, as illustrated in Figure 5.9 and Figure 5.7, respectively.

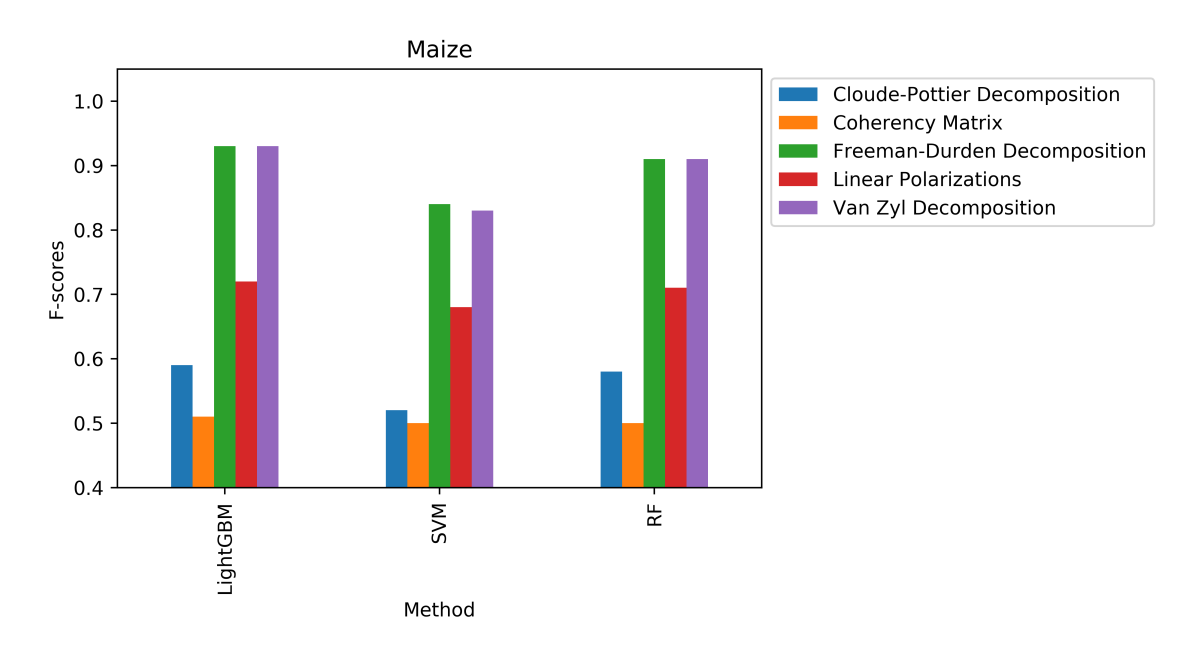


Figure 5.18 F-scores for Maize

When Figure 5.19 was examined, it can be seen that polarimetric features with an exception of Cloude-Pottier decomposition produced higher score than original features (i.e. coherency matrix and linear polarizations) for the identification/classification of potato. The underlying reason of this exception could be that the temporal line for potato has crossed with wheat in Entropy (Figure 5.1) and the alpha angle values of potato is very close (similar) to maize (Figure 5.3). Within intercomparison of decomposition methods in terms of F-score for maize, Van Zyl decomposition produced the very similar scores with Freeman-Durden decomposition. Cloude-Pottier decomposition produced lowest scores for potato among decomposition methods as well as all features. Different from the classes of maize and alfalfa, Coherency matrix outperformed Cloude-Pottier decomposition in terms of F-scores for potato

## 5.5.4 Sunflower

Van Zyl and Freeman-Durden decomposition with each model produced the highest score (1.0) while Coherency matrix by RF produced the lowest score (0.77) for sunflower, as illustrated in Figure 5.20. Van Zyl and Freeman-Durden decomposition with each model produced the equal and highest score (1.00) and followed by Cloude Pottier decomposition with per model (0.99), Linear polarizations with LightGBM (0.92) and Linear polarizations with SVM (0.91)

Sunflower has sharp changes in surface scattering from leaf development stage to heading stage (Figure 5.7) and in volume scattering (Figure 5.9) from stem elongation

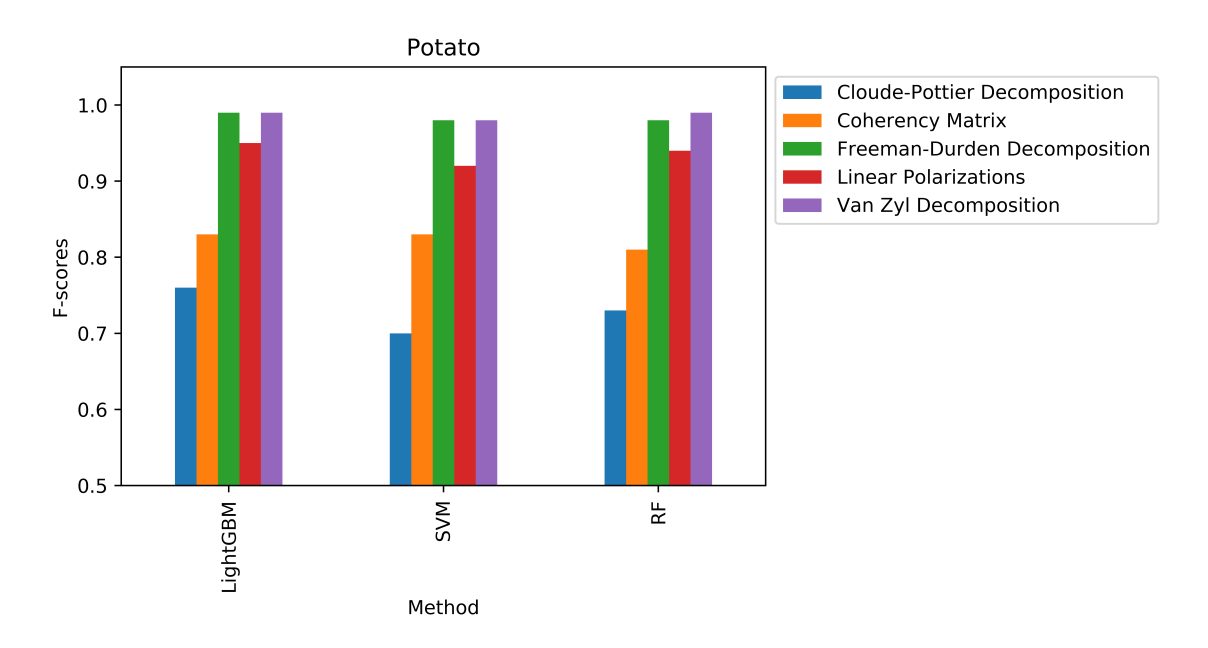


Figure 5.19 F-scores for Potato

stage to heading stage, that provide the good separation of sunflower from other classes. This might be the underlying reason of how Van Zyl and Freeman-Durden decomposition with per classification model produced the highest F-score (1.00).

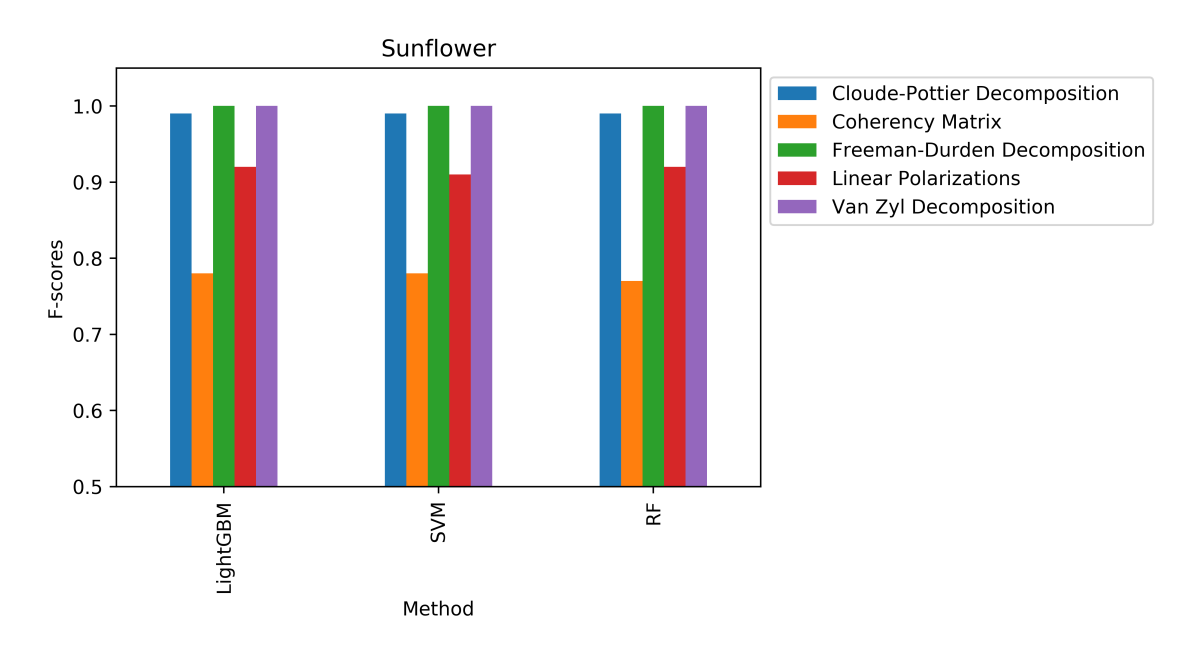


Figure 5.20 F-scores for Sunflower

When Figure 5.20 was examined, it can be deduced that polarimetric features produced higher score than original features (i.e.coherency matrix and linear polarizations) for the identification/classification of sunflower. Among intercomparison of decomposition methods in terms of F-score for sunflower, there is not any difference between Van Zyl decomposition and Freeman-Durden

decomposition as either decomposition achieved 1.00 F-score for all classification method.

#### 5.5.5 Wheat

As similar manner to sunflower, Van Zyl and Freeman-Durden decomposition with each model produced the highest score (0.98) while Coherency matrix by RF produced the lowest score (0.93) for wheat, as illustrated in Figure 5.21. Wheat was classified higher than 0.90 F-scores for all features per classification model.

Wheat has the critical changes (i.e sharp decline) in double-bounce scattering (Figure 5.8) and low scattering compared to other crops in volume scattering (Figure 5.9), which lead to greater separation of wheat from other crops. These key differences enabled that Van Zyl and Freeman-Durden decomposition with per model produced the highest F-score (0.98)

Van Zyl and Freeman-Durden decomposition with per model produced the equal and highest score (0.98) and followed by Linear polarizations with LightGBM (0.97), Linear polarizations with SVM (0.96) and Cloude-Pottier decomposition with LightGBM (0.95).

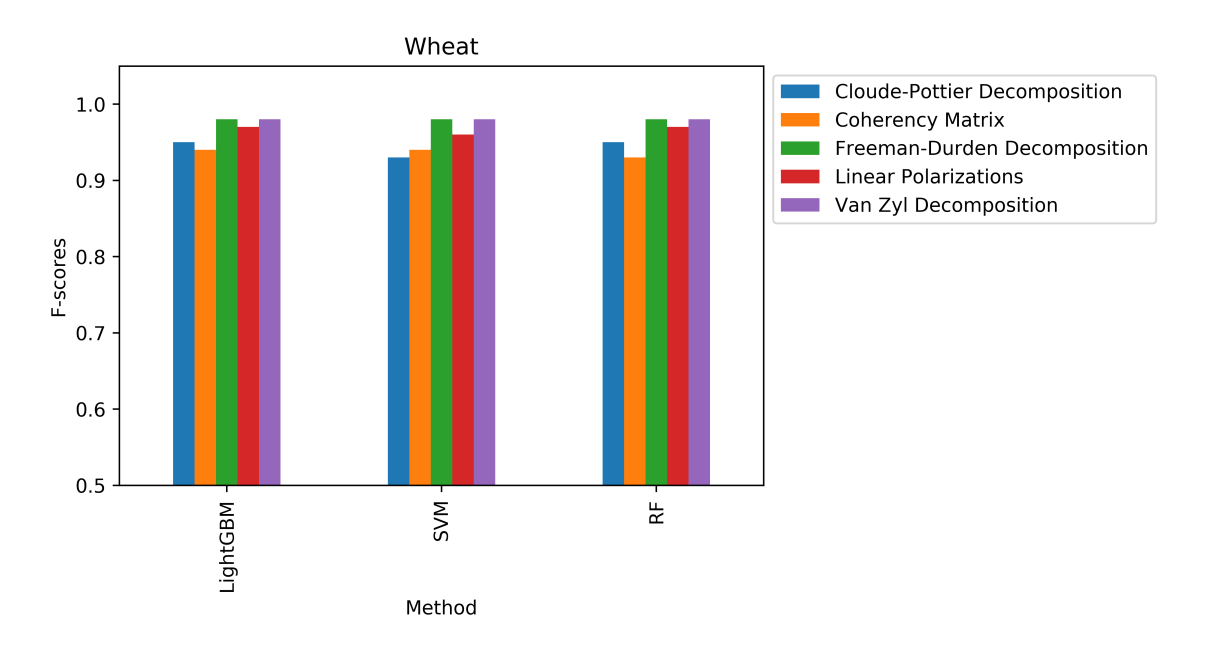


**Figure 5.21** F-scores for Wheat

When Figure 5.21 was examined, it can be seen that polarimetric features with an exception of Cloude-Pottier decomposition produced higher score than original features (i.e. coherency matrix and linear polarizations) for the identification/classification of wheat. Within intercomparison of decomposition

methods in terms of F-score for maize, Van Zyl decomposition produced the equal scores with Freeman-Durden decomposition (0.98). Linear polarizations achieved higher scores than Coherency Matrix and Cloude-Pottier decomposition for wheat.

## 5.6 Conclusion

In this thesis, the performance of original and polarimetric features from the multi-temporal PolSAR data was investigated and the usability of multi-temporal PolSAR data for the crop pattern identification was evaluated using three different machine learning algorithms.

The experimental results highlights the superior performance of LightGBM compared to RF and SVM in terms of overall accuracy and computational cost. There is no statistically significance (up to McNemar's test) between the overall accuracies of LightGBM and SVM for coherency matrix as well as LightGBM and RF for linear polarizations. However LightGBM is much faster (almost ten times) than RF and SVM, when compared the CPU running times for training process. RF produced higher classification accuracy than SVM for all features with an exception of coherency matrix where LightGBM and SVM yielded the same accuracy score and outperformed RF (0.723 vs 0.710).

The highest classification accuracy (0.96) were received by Van Zyl decomposition and Freeman-Durden through LightGBM. Even though these two decomposition produced same accuracy and kappa score for LightGBM, Freeman-Durden outperformed Van Zyl for SVM however Van Zyl yielded higher score than Freeman-Durden for RF on the contrary. This diversity is due to class signatures have different impact on the training process of the machine learning algorithms at their decision making process. Compared to Cloude-Pottier decomposition in terms of classification performance, Van Zyl decomposition as another eigenvector-based decomposition method yielded higher accuracy in all classification model. The possible reason should be of all the parameters of Cloude-Pottier decomposition are relative to power and do not have the power (intensity) information. Furthermore, Cloude-Pottier demonstrated greater performance than coherency matrix in all classification model with an exception of linear polarizations.

For linear polarizations, coherency matrix and Cloude-Pottier decomposition, the LightGBM is much faster (almost ten times) than RF and SVM. However for the Freeman-Durden and Van Zyl decomposition, SVM is slightly faster than LightGBM in terms of training time (in the milliseconds level). This is probably because SVM was able to define the optimal hyperplane between the classes in a simple way, where the

scattering was provided based upon the three fundamental scattering type (surface, dihedral and volume).

This thesis proved the benefits of model based and hybrid based decomposition about obtaining higher performance compared to original features for crop pattern classification. Also the efficiency of LightGBM, a novel ensemble learning algorithm, was explored for crop classification from multi-temporal PolSAR data.

- [1] I. H. Woodhouse, Introduction to Microwave Remote Sensing. CRC press, 2017.
- [2] H. McNairn J. Shang, "A review of Multitemporal Synthetic Aperture Radar (SAR) for crop monitoring," in *Multitemporal Remote Sensing*, Springer, 2016, pp. 317–340.
- [3] A. Larrañaga J. Álvarez-Mozos, "On the added value of quad-pol data in a multi-temporal crop classification framework based on RADARSAT-2 imagery," *Remote Sensing*, vol. 8, no. 4, p. 335, 2016.
- [4] H. McNairn B. Brisco, "The application of c-band polarimetric sar for agriculture: A review," *Canadian Journal of Remote Sensing*, vol. 30, no. 3, pp. 525–542, 2004.
- [5] X. Jiao, J. M. Kovacs, J. Shang, H. McNairn, D. Walters, B. Ma, X. Geng, "Object-oriented crop mapping and monitoring using multi-temporal polarimetric RADARSAT-2 data," *ISPRS Journal of Photogrammetry and Remote Sensing*, vol. 96, pp. 38–46, 2014.
- [6] H. Skriver, F. Mattia, G. Satalino, A. Balenzano, V. R. Pauwels, N. E. Verhoest, M. Davidson, "Crop classification using short-revisit multitemporal sar data," *IEEE Journal of Selected Topics in Applied Earth Observations and Remote Sensing*, vol. 4, no. 2, pp. 423–431, 2011.
- [7] J.-S. Lee E. Pottier, *Polarimetric radar imaging: from basics to applications*. CRC press, 2009.
- [8] H. Tamiminia, S. Homayouni, H. McNairn, A. Safari, "A particle swarm optimized kernel-based clustering method for crop mapping from multi-temporal polarimetric l-band SAR observations," *International journal of applied earth observation and geoinformation*, vol. 58, pp. 201–212, 2017.
- [9] Q. Xie, J. Wang, C. Liao, J. Shang, J. M. Lopez-Sanchez, H. Fu, X. Liu, "On the use of neumann decomposition for crop classification using multi-temporal RADARSAT-2 polarimetric SAR data," *Remote Sensing*, vol. 11, no. 7, p. 776, 2019.
- [10] A. Moreira, P. Prats-Iraola, M. Younis, G. Krieger, I. Hajnsek, K. P. Papathanassiou, "A tutorial on Synthetic Aperture Radar," *IEEE Geoscience and remote sensing magazine*, vol. 1, no. 1, pp. 6–43, 2013.
- [11] A. Marino, S. R. Cloude, J. M. Lopez-Sanchez, "A new polarimetric change detector in radar imagery," *IEEE Transactions on Geoscience and Remote Sensing*, vol. 51, no. 5, pp. 2986–3000, 2012.

- [12] S.-W. Chen, Y.-Z. Li, X.-S. Wang, S.-P. Xiao, M. Sato, "Modeling and interpretation of scattering mechanisms in polarimetric synthetic aperture radar: Advances and perspectives," *IEEE Signal Processing Magazine*, vol. 31, no. 4, pp. 79–89, 2014.
- [13] Y. X. Lim, M. S. Burgin, J. J. van Zyl, "An optimal nonnegative eigenvalue decomposition for the freeman and durden three-component scattering model," *IEEE Transactions on Geoscience and Remote Sensing*, vol. 55, no. 4, pp. 2167–2176, 2017.
- [14] C. Liao, J. Wang, X. Huang, J. Shang, "Contribution of minimum noise fraction transformation of multi-temporal RADARSAT-2 polarimetric SAR data to cropland classification," *Canadian Journal of Remote Sensing*, vol. 44, no. 3, pp. 215–231, 2018.
- [15] H. McNairn, J. Shang, X. Jiao, C. Champagne, "The contribution of alos palsar multipolarization and polarimetric data to crop classification," *IEEE Transactions on Geoscience and Remote Sensing*, vol. 47, no. 12, pp. 3981–3992, 2009.
- [16] T. Whelen P. Siqueira, "Use of time-series l-band uavsar data for the classification of agricultural fields in the san joaquin valley," *Remote sensing of environment*, vol. 193, pp. 216–224, 2017.
- [17] S. Hariharan, D. Mandal, S. Tirodkar, V. Kumar, A. Bhattacharya, J. M. Lopez-Sanchez, "A novel phenology based feature subset selection technique using random forest for multitemporal polsar crop classification," *IEEE Journal of Selected Topics in Applied Earth Observations and Remote Sensing*, vol. 11, no. 11, pp. 4244–4258, 2018.
- [18] I. Khosravi S. K. Alavipanah, "A random forest-based framework for crop mapping using temporal, spectral, textural and polarimetric observations," *International Journal of Remote Sensing*, vol. 40, no. 18, pp. 7221–7251, 2019.
- [19] H. Li, C. Zhang, S. Zhang, P. M. Atkinson, "Full year crop monitoring and separability assessment with fully-polarimetric l-band uavsar: A case study in the sacramento valley, california," *International Journal of Applied Earth Observation and Geoinformation*, vol. 74, pp. 45–56, 2019.
- [20] K. Li, B. Brisco, S. Yun, R. Touzi, "Polarimetric decomposition with RADARSAT-2 for rice mapping and monitoring," *Canadian Journal of Remote Sensing*, vol. 38, no. 2, pp. 169–179, 2012.
- [21] Q. Ma, J. Wang, J. Shang, P. Wang, "Assessment of multi-temporal RADARSAT-2 polarimetric SAR data for crop classification in an urban/rural fringe area," in *2013 Second International Conference on Agro-Geoinformatics* (Agro-Geoinformatics), IEEE, 2013, pp. 314–319.
- [22] H. H. Zeyada, M. M. Ezz, A. H. Nasr, M. Shokr, H. M. Harb, "Evaluation of the discrimination capability of full polarimetric SAR data for crop classification," *International Journal of Remote Sensing*, vol. 37, no. 11, pp. 2585–2603, 2016.
- [23] P. Srikanth, K. Ramana, U. Deepika, P. K. Chakravarthi, M. S. Sai, "Comparison of various polarimetric decomposition techniques for crop classification," *Journal of the Indian Society of Remote Sensing*, vol. 44, no. 4, pp. 635–642, 2016.

- [24] G. Shuai, J. Zhang, B. Basso, Y. Pan, X. Zhu, S. Zhu, H. Liu, "Multi-temporal RADARSAT-2 polarimetric SAR for maize mapping supported by segmentations from high-resolution optical image," *International Journal of Applied Earth Observation and Geoinformation*, vol. 74, pp. 1–15, 2019.
- [25] M. Ustuner F. Balik Sanli, "Polarimetric target decompositions and light gradient boosting machine for crop classification: A comparative evaluation," *ISPRS International Journal of Geo-Information*, vol. 8, no. 2, p. 97, 2019.
- [26] J. R. Jensen, *Remote sensing of the environment: An earth resource perspective 2/e.* Pearson Education India, 2009.
- [27] J. J. van Zyl, *Synthetic Aperture Radar Polarimetry*. John Wiley & Sons, 2011, vol. 2.
- [28] T. Lillesand, R. W. Kiefer, J. Chipman, *Remote sensing and image interpretation*. John Wiley & Sons, 2015.
- [29] M. Schmitt, "Reconstruction of urban surface models from multi-aspect and multi-baseline interferometric sar," PhD thesis, Technische Universität München, 2014.
- [30] C. Schmullius, C. Thiel, C. Pathe, M. Santoro, "Radar time series for land cover and forest mapping," in *Remote Sensing Time Series*, Springer, 2015, pp. 323–356.
- [31] F. T. Ulaby, R. K. Moore, A. K. Fung, "Microwave remote sensing: Active and passive. volume 3-from theory to applications," 1986.
- [32] N. R. Canada, Fundamentals of Remote Sensing. Natural Resources Canada.
- [33] S. Cloude, *Polarisation: Applications in Remote Sensing*. Oxford University Press, 2010.
- [34] Radar polarimetry-introduction to polarization. [Online]. Available: https://www.nrcan.gc.ca/maps-tools-publications/satellite-imagery-air-photos/remote-sensing-tutorials/microwave-remote-sensing/radar-polarimetry/9275 (visited on 02/01/2020).
- [35] C. Lopez-Martinez, E. Pottier, S. R. Cloude, "Statistical assessment of eigenvector-based target decomposition theorems in radar polarimetry," *IEEE Transactions on Geoscience and Remote Sensing*, vol. 43, no. 9, pp. 2058–2074, 2005.
- [36] C. López-Martinez X. Fabregas, "Polarimetric sar speckle noise model," *IEEE Transactions on Geoscience and Remote Sensing*, vol. 41, no. 10, pp. 2232–2242, 2003.
- [37] L. Mascolo, "Polarimetric SAR for the monitoring of agricultural crops," *Ph. D. Thesis, Università degli Studi di Cagliari, Italy*, 2015.
- [38] J. HUYNEN, "Phenomenological theory of radar targets," *Ph. D. Thesis, Technical University Delft, Netherlands*, 1970.
- [39] S. R. Cloude E. Pottier, "A review of target decomposition theorems in radar polarimetry," *IEEE Transactions on Geoscience and Remote Sensing*, vol. 34, no. 2, pp. 498–518, 1996.

- [40] A. Freeman S. L. Durden, "A three-component scattering model for polarimetric SAR data," *IEEE Transactions on Geoscience and Remote Sensing*, vol. 36, no. 3, pp. 963–973, 1998.
- [41] J. J. Van Zyl, M. Arii, Y. Kim, "Model-based decomposition of polarimetric SAR covariance matrices constrained for nonnegative eigenvalues," *IEEE Transactions on Geoscience and Remote Sensing*, vol. 49, no. 9, pp. 3452–3459, 2011.
- [42] W. A. Holm R. M. Barnes, "On radar polarization mixed target state decomposition techniques," *Proceedings of the 1988 IEEE National Radar Conference*, pp. 249–254, 1988.
- [43] J. Yang, Y.-N. Peng, Y. Yamaguchi, H. Yamada, "On huynen's decomposition of a kennaugh matrix," *IEEE Geoscience and Remote Sensing Letters*, vol. 3, no. 3, pp. 369–372, Jul. 2006.
- [44] S. R. Cloude, "Radar target decomposition theorems," *Electronics letters*, vol. 21, no. 1, pp. 22–24, 1985.
- [45] J. J. van Zyl, "Application of cloude's target decomposition theorem to polarimetric imaging radar data," in *Radar polarimetry*, International Society for Optics and Photonics, vol. 1748, 1993, pp. 184–191.
- [46] S. R. Cloude E. Pottier, "An entropy based classification scheme for land applications of polarimetric SAR," *IEEE Transactions on Geoscience and Remote Sensing*, vol. 35, no. 1, pp. 68–78, 1997.
- [47] Y. Yamaguchi, T. Moriyama, M. Ishido, H. Yamada, "Four-component scattering model for polarimetric SAR image decomposition," *IEEE Transactions on Geoscience and Remote Sensing*, vol. 43, no. 8, pp. 1699–1706, 2005.
- [48] Y. Dong, B. C. Forster, C. Ticehurst, "A new decomposition of radar polarization signatures," *IEEE transactions on geoscience and remote sensing*, vol. 36, no. 3, pp. 933–939, 1998.
- [49] E. Krogager A. Freeman, "Three component break-downs of scattering matrices for radar target identification and classification," *Proc. PIERS'94*, p. 391, 1994.
- [50] W. L. Cameron L. K. Leung, "Feature motivated polarization scattering matrix decomposition," in *IEEE International Conference on Radar*, IEEE, 1990, pp. 549–557.
- [51] R. Touzi F. Charbonneau, "Characterization of target symmetric scattering using polarimetric SARs," *IEEE Trans. Geoscience and Remote Sensing*, vol. 40, pp. 2507–2516, 2002.
- [52] M. Mahdianpari, B. Salehi, F. Mohammadimanesh, B. Brisco, S. Mahdavi, M. Amani, J. E. Granger, "Fisher linear discriminant analysis of coherency matrix for wetland classification using PolSAR imagery," *Remote Sensing of Environment*, vol. 206, pp. 300–317, 2018.
- [53] S.-E. Park, "The effect of topography on target decomposition of polarimetric SAR data," *Remote Sensing*, vol. 7, no. 5, pp. 4997–5011, 2015.
- [54] Y.-Q. Jin F. Xu, *Polarimetric scattering and SAR information retrieval*. John Wiley & Sons, 2013.

- [55] P. M. Mather M. Koch, Computer processing of remotely-sensed images: an introduction. John Wiley & Sons, 2011.
- [56] D. Lu Q. Weng, "A survey of image classification methods and techniques for improving classification performance," *International journal of Remote sensing*, vol. 28, no. 5, pp. 823–870, 2007.
- [57] G. M. Foody, A. Mathur, C. Sanchez-Hernandez, D. S. Boyd, "Training set size requirements for the classification of a specific class," *Remote Sensing of Environment*, vol. 104, no. 1, pp. 1–14, 2006.
- [58] M. Pal, "Advanced algorithms for land use and cover classification," *Advances in mapping from remote sensor imagery*, pp. 70–82, 2012.
- [59] R. Khatami, G. Mountrakis, S. V. Stehman, "A meta-analysis of remote sensing research on supervised pixel-based land-cover image classification processes: General guidelines for practitioners and future research," *Remote Sensing of Environment*, vol. 177, pp. 89–100, 2016.
- [60] T. Kavzoglu, "Increasing the accuracy of neural network classification using refined training data," *Environmental Modelling & Software*, vol. 24, no. 7, pp. 850–858, 2009.
- [61] P. Ghamisi, J. Plaza, Y. Chen, J. Li, A. J. Plaza, "Advanced spectral classifiers for hyperspectral images: A review," *IEEE Geoscience and Remote Sensing Magazine*, vol. 5, no. 1, pp. 8–32, 2017.
- [62] B. Waske M. Braun, "Classifier ensembles for land cover mapping using multitemporal SAR imagery," *ISPRS Journal of Photogrammetry and Remote Sensing*, vol. 64, no. 5, pp. 450–457, 2009.
- [63] T. Kavzoglu I. Colkesen, "An assessment of the effectiveness of a rotation forest ensemble for land-use and land-cover mapping," *International Journal of Remote Sensing*, vol. 34, no. 12, pp. 4224–4241, 2013.
- [64] J. Xia, P. Du, X. He, J. Chanussot, "Hyperspectral remote sensing image classification based on rotation forest," *IEEE Geoscience and Remote Sensing Letters*, vol. 11, no. 1, pp. 239–243, 2013.
- [65] A. Samat, P. Gamba, S. Liu, Z. Miao, E. Li, J. Abuduwaili, "Quad-polsar data classification using modified random forest algorithms to map halophytic plants in arid areas," *International journal of applied earth observation and geoinformation*, vol. 73, pp. 503–521, 2018.
- [66] A. Samat, C. Persello, S. Liu, E. Li, Z. Miao, J. Abuduwaili, "Classification of vhr multispectral images using extratrees and maximally stable extremal region-guided morphological profile," *IEEE Journal of Selected Topics in Applied Earth Observations and Remote Sensing*, vol. 11, no. 9, pp. 3179–3195, 2018.
- [67] T. Chen C. Guestrin, "Xgboost: A scalable tree boosting system," in *Proceedings* of the 22nd acm sigkdd international conference on knowledge discovery and data mining, ACM, 2016, pp. 785–794.
- [68] T. Rainforth F. Wood, "Canonical correlation forests," *arXiv preprint arXiv:1507.05444*, 2015.

- [69] A. Samat, S. Liu, C. Persello, E. Li, Z. Miao, J. Abuduwaili, "Evaluation of forestpa for vhr rs image classification using spectral and superpixel-guided morphological profiles," *European Journal of Remote Sensing*, vol. 52, no. 1, pp. 107–121, 2019.
- [70] G. Ke, Q. Meng, T. Finley, T. Wang, W. Chen, W. Ma, Q. Ye, T.-Y. Liu, "Lightgbm: A highly efficient gradient boosting decision tree," in *Advances in Neural Information Processing Systems*, 2017, pp. 3146–3154.
- [71] P. Du, A. Samat, B. Waske, S. Liu, Z. Li, "Random forest and rotation forest for fully polarized SAR image classification using polarimetric and spatial features," *ISPRS Journal of Photogrammetry and Remote Sensing*, vol. 105, pp. 38–53, 2015.
- [72] G. Mills G. Fotopoulos, "Rock surface classification in a mine drift using multiscale geometric features," *IEEE Geoscience and Remote Sensing Letters*, vol. 12, no. 6, pp. 1322–1326, 2015.
- [73] S. Georganos, T. Grippa, S. Vanhuysse, M. Lennert, M. Shimoni, E. Wolff, "Very high resolution object-based land use-land cover urban classification using extreme gradient boosting," *IEEE Geoscience and Remote Sensing Letters*, vol. 15, no. 4, pp. 607–611, 2018.
- [74] H. Dong, X. Xu, L. Wang, F. Pu, "Gaofen-3 PolSAR image classification via XGBoost and polarimetric spatial information," *Sensors*, vol. 18, no. 2, p. 611, 2018.
- [75] J. Xia, N. Yokoya, A. Iwasaki, "Hyperspectral image classification with canonical correlation forests," *IEEE Transactions on Geoscience and Remote Sensing*, vol. 55, no. 1, pp. 421–431, 2016.
- [76] I. Colkesen T. Kavzoglu, "Ensemble-based canonical correlation forest (ccf) for land use and land cover classification using sentinel-2 and landsat oli imagery," *Remote Sensing Letters*, vol. 8, no. 11, pp. 1082–1091, 2017.
- [77] F. Melgani L. Bruzzone, "Classification of hyperspectral remote sensing images with support vector machines," *IEEE Transactions on geoscience and remote sensing*, vol. 42, no. 8, pp. 1778–1790, 2004.
- [78] P. O. Gislason, J. A. Benediktsson, J. R. Sveinsson, "Random forests for land cover classification," *Pattern Recognition Letters*, vol. 27, no. 4, pp. 294–300, 2006.
- [79] C. Cortes V. Vapnik, "Support-vector networks," *Machine learning*, vol. 20, no. 3, pp. 273–297, 1995.
- [80] T. Kavzoglu I. Colkesen, "A kernel functions analysis for support vector machines for land cover classification," *International Journal of Applied Earth Observation and Geoinformation*, vol. 11, no. 5, pp. 352–359, 2009.
- [81] P. K. Srivastava, D. Han, M. A. Rico-Ramirez, M. Bray, T. Islam, "Selection of classification techniques for land use/land cover change investigation," *Advances in Space Research*, vol. 50, no. 9, pp. 1250–1265, 2012.
- [82] S. R. Joelsson, J. A. Benediktsson, J. R. Sveinsson, "Random forest classification of remote sensing data," in *Signal and Image Processing for Remote Sensing*, CRC Press, 2006, pp. 344–361.

- [83] V. F. Rodriguez-Galiano, B. Ghimire, J. Rogan, M. Chica-Olmo, J. P. Rigol-Sanchez, "An assessment of the effectiveness of a random forest classifier for land-cover classification," *ISPRS Journal of Photogrammetry and Remote Sensing*, vol. 67, pp. 93–104, 2012.
- [84] L. Breiman, "Bagging predictors," *Machine learning*, vol. 24, no. 2, pp. 123–140, 1996.
- [85] Y. Freund, R. Schapire, N. Abe, "A short introduction to boosting," *Journal-Japanese Society For Artificial Intelligence*, vol. 14, no. 771-780, p. 1612, 1999.
- [86] L. Breiman, "Random forests," *Machine learning*, vol. 45, no. 1, pp. 5–32, 2001.
- [87] J. J. Rodriguez, L. I. Kuncheva, C. J. Alonso, "Rotation forest: A new classifier ensemble method," *IEEE transactions on pattern analysis and machine intelligence*, vol. 28, no. 10, pp. 1619–1630, 2006.
- [88] P. Geurts, D. Ernst, L. Wehenkel, "Extremely randomized trees," *Machine learning*, vol. 63, no. 1, pp. 3–42, 2006.
- [89] J. H. Friedman, "Greedy function approximation: A gradient boosting machine," *Annals of statistics*, pp. 1189–1232, 2001.
- [90] J. Feng, Y. Yu, Z.-H. Zhou, "Multi-layered gradient boosting decision trees," in *Advances in neural information processing systems*, 2018, pp. 3551–3561.
- [91] A. V. Dorogush, V. Ershov, A. Gulin, "CatBoost: Gradient boosting with categorical features support," *arXiv preprint arXiv:1810.11363*, 2018.
- [92] Machine learning challenge winning solutions. [Online]. Available: https://github.com/microsoft/LightGBM/blob/master/examples/README.md#machine-learning-challenge-winning-solutions (visited on 10/20/2019).
- [93] J. Wang, J. Li, B. Yang, R. Xie, T. T. Marquez-Lago, A. Leier, M. Hayashida, T. Akutsu, Y. Zhang, K.-C. Chou, *et al.*, "Bastion3: A two-layer ensemble predictor of type iii secreted effectors," *Bioinformatics*, vol. 35, no. 12, pp. 2017–2028, 2018.
- [94] W. Li, S. Ding, Y. Chen, H. Wang, S. Yang, "Transfer learning-based default prediction model for consumer credit in china," *The Journal of Supercomputing*, vol. 75, no. 2, pp. 862–884, 2019.
- [95] Lightgbm python package. [Online]. Available: https://pypi.org/project/lightgbm/(visited on 10/20/2019).
- [96] Parameters. [Online]. Available: https://lightgbm.readthedocs.io/en/latest/Parameters.html (visited on 10/20/2019).
- [97] G. M. Foody, "Status of land cover classification accuracy assessment," *Remote sensing of environment*, vol. 80, no. 1, pp. 185–201, 2002.
- [98] J.-W. Chan, N. Laporte, R. Defries, "Texture classification of logged forests in tropical africa using machine-learning algorithms," *International Journal of Remote Sensing*, vol. 24, no. 6, pp. 1401–1407, 2003.
- [99] M. Pal, "Artificial immune-based supervised classifier for land-cover classification," *International Journal of Remote Sensing*, vol. 29, no. 8, pp. 2273–2291, 2008.

- [100] A. E. Maxwell, T. A. Warner, F. Fang, "Implementation of machine-learning classification in remote sensing: An applied review," *International Journal of Remote Sensing*, vol. 39, no. 9, pp. 2784–2817, 2018.
- [101] C. A Ramezan, T. A Warner, A. E Maxwell, "Evaluation of sampling and cross-validation tuning strategies for regional-scale machine learning classification," *Remote Sensing*, vol. 11, no. 2, p. 185, 2019.
- [102] M. Kuhn K. Johnson, Applied predictive modeling. Springer, 2013, vol. 26.
- [103] J. Zhang, G. S. Okin, B. Zhou, "Assimilating optical satellite remote sensing images and field data to predict surface indicators in the western us: Assessing error in satellite predictions based on large geographical datasets with the use of machine learning," *Remote Sensing of Environment*, vol. 233, p. 111 382, 2019.
- [104] R. Hänsch O. Hellwich, "Skipping the real world: Classification of polsar images without explicit feature extraction," *ISPRS Journal of Photogrammetry and Remote Sensing*, vol. 140, pp. 122–132, 2018.
- [105] F. Pedregosa, G. Varoquaux, A. Gramfort, V. Michel, B. Thirion, O. Grisel, M. Blondel, P. Prettenhofer, R. Weiss, V. Dubourg, J. Vanderplas, A. Passos, D. Cournapeau, M. Brucher, M. Perrot, E. Duchesnay, "Scikit-learn: Machine learning in Python," *Journal of Machine Learning Research*, vol. 12, pp. 2825–2830, 2011.
- [106] L. Buitinck, G. Louppe, M. Blondel, F. Pedregosa, A. Mueller, O. Grisel, V. Niculae, P. Prettenhofer, A. Gramfort, J. Grobler, R. Layton, J. VanderPlas, A. Joly, B. Holt, G. Varoquaux, "API design for machine learning software: Experiences from the scikit-learn project," in *ECML PKDD Workshop: Languages for Data Mining and Machine Learning*, 2013, pp. 108–122.
- [107] G. Hackeling, Mastering Machine Learning with scikit-learn. Packt Publishing Ltd, 2017.
- [108] Parameters tuning. [Online]. Available: https://lightgbm.readthedocs.io/en/latest/Parameters-Tuning.html (visited on 10/20/2019).

# Appendix 1

Normalized confusion matrices, McNemar's test results, F-scores for classes and overall classification accuracies are provided in Appendix A.

 Table A.1 Normalized Confusion Matrices for LightGBM

# **Linear Polarization**

	Alfalfa	Maize	Potato	Sunflower	Wheat	
Alfalfa	0.7	0.23	0.02	0.01	0.03	
Maize	0.17	0.73	0.03	0.06	0.0	
Potato	0.02	0.02	0.95	0.01	0.0	
Sunflower	0.01	0.06	0.01	0.92	0.0	
Wheat	0.03	0.0	0.0	0.0	0.97	
	Cloude	-Pottier	Decomp	osition		
Alfalfa	0.62	0.22	0.15	0.0	0.01	
Maize	0.24	0.58	0.13	0.01	0.04	
Potato	0.1	0.13	0.76	0.0	0.01	
Sunflower	0.0	0.01	0.0	0.99	0.0	
Wheat	0.01	0.03	0.0	0.0	0.96	
	(	Coheren	cy Matri	X		
Alfalfa	0.52	0.3	0.1	0.04	0.05	
Maize	0.25	0.51	0.09	0.14	0.01	
Potato	0.06	0.05	0.86	0.03	0.0	
Sunflower	0.03	0.15	0.05	0.78	0.0	
Wheat	0.06	0.0	0.0	0.0	0.94	
	Freemar	1-Durde	n Decom	position		
Alfalfa	0.88	0.08	0.01	0.0	0.02	
Maize	0.05	0.94	0.0	0.0	0.0	
Potato	0.0	0.01	0.99	0.0	0.0	
Sunflower	0.0	0.0	0.0	1.0	0.0	
Wheat	0.01	0.0	0.0	0.0	0.99	
Van Zyl Decomposition						
Alfalfa	0.89	0.08	0.01	0.0	0.02	
Maize	0.05	0.94	0.0	0.0	0.0	
Potato	0.0	0.01	0.99	0.0	0.0	
Sunflower	0.0	0.0	0.0	1.0	0.0	
Wheat	0.01	0.0	0.0	0.0	0.99	

 Table A.2 Normalized Confusion Matrices for RF

## **Linear Polarization**

	Alfalfa	Maize	Potato	Sunflower	Wheat	
Alfalfa	0.68	0.25	0.03	0.01	0.03	
Maize	0.16	0.74	0.04	0.06	0.0	
Potato	0.02	0.02	0.96	0.01	0.0	
Sunflower	0.0	0.07	0.01	0.92	0.0	
Wheat	0.03	0.0	0.0	0.0	0.97	
	Cloude	-Pottier	Decomp	osition		
Alfalfa	0.56	0.23	0.19	0.0	0.01	
Maize	0.24	0.56	0.15	0.01	0.04	
Potato	0.11	0.12	0.75	0.0	0.01	
Sunflower	0.0	0.01	0.0	0.99	0.0	
Wheat	0.02	0.02	0.0	0.0	0.96	
	(	Coheren	cy Matri	x		
Alfalfa	0.46	0.29	0.14	0.05	0.06	
Maize	0.23	0.49	0.12	0.14	0.01	
Potato	0.06	0.03	0.88	0.03	0.0	
Sunflower	0.02	0.15	0.06	0.76	0.0	
Wheat	0.07	0.0	0.0	0.0	0.93	
	Freemar	1-Durde	n Decom	position		
Alfalfa	0.85	0.11	0.01	0.0	0.02	
Maize	0.05	0.94	0.0	0.0	0.0	
Potato	0.01	0.01	0.99	0.0	0.0	
Sunflower	0.0	0.01	0.0	0.99	0.0	
Wheat	0.02	0.0	0.0	0.0	0.98	
Van Zyl Decomposition						
Alfalfa	0.87	0.11	0.01	0.0	0.02	
Maize	0.05	0.94	0.0	0.0	0.0	
Potato	0.01	0.01	0.99	0.0	0.0	
Sunflower	0.0	0.01	0.0	0.99	0.0	
Wheat	0.02	0.0	0.0	0.0	0.98	

 Table A.3 Normalized Confusion Matrices for SVM

## **Linear Polarization**

	Alfalfa	Maize	Potato	Sunflower	Wheat	
Alfalfa	0.71	0.23	0.03	0.01	0.03	
Maize	0.22	0.68	0.03	0.06	0.0	
Potato	0.06	0.03	0.91	0.01	0.0	
Sunflower	0.01	0.06	0.01	0.91	0.0	
Wheat	0.04	0.0	0.0	0.0	0.96	
	Cloude	-Pottier	Decomp	osition		
Alfalfa	0.6	0.21	0.16	0.0	0.02	
Maize	0.31	0.5	0.13	0.0	0.05	
Potato	0.17	0.15	0.68	0.0	0.01	
Sunflower	0.0	0.01	0.0	0.99	0.0	
Wheat	0.02	0.04	0.0	0.0	0.94	
	(	Coheren	cy Matri	X		
Alfalfa	0.53	0.28	0.08	0.04	0.07	
Maize	0.29	0.49	0.09	0.13	0.01	
Potato	0.07	0.05	0.85	0.04	0.0	
Sunflower	0.02	0.16	0.04	0.78	0.0	
Wheat	0.04	0.0	0.0	0.0	0.95	
	Freemar	ı-Durdeı	n Decom	position		
Alfalfa	0.78	0.18	0.01	0.0	0.02	
Maize	0.12	0.87	0.01	0.0	0.0	
Potato	0.0	0.01	0.98	0.0	0.0	
Sunflower	0.0	0.0	0.0	1.00	0.0	
Wheat	0.02	0.0	0.0	0.0	0.98	
Van Zyl Decomposition						
Alfalfa	0.77	0.2	0.01	0.0	0.02	
Maize	0.13	0.86	0.0	0.0	0.0	
Potato	0.0	0.01	0.98	0.0	0.0	
				1 00	0.0	
Sunflower	0.0	0.0	0.0	1.00	0.0	

Table A.4 McNemar's test results for Coherency Matrix

	LightGBM	RF	SVM
LightGBM	-	42.50	0.0002
RF		-	41.16
SVM			-

Table A.5 McNemar's test results for Linear Polarizations

	LightGBM	RF	SVM
LightGBM	-	1.68	160.25
RF		-	122.57
SVM			-

Table A.6 McNemar's test results for Cloude-Pottier Decomposition

	LightGBM	RF	SVM
LightGBM	-	68.64	335.92
RF		-	133.95
SVM			-

Table A.7 McNemar's test results for Freeman-Durden Decomposition

	LightGBM	RF	SVM
LightGBM	-	66.45	580.04
RF		-	385.27
SVM			-

Table A.8 McNemar's test results for Van Zyl Decomposition

	LightGBM	RF	SVM
LightGBM	-	30.37	746.79
RF		-	615.70
SVM			-

 Table A.9 Overall accuracy with standart deviation

	Accuracy: acc. (+/- std)					
Data Type	Light GBM	SVM	RF			
Coherency Matrix	0.723 (+/- 0.019)	0.723 (+/- 0.018)	0.710 (+/- 0.022)			
Linear Polarizations	0.857 (+/- 0.026)	0.834 (+/- 0.039)	0.856 (+/- 0.033)			
Cloude-Pottier Decom	0.780 (+/- 0.043)	0.738 (+/- 0.039)	0.766 (+/- 0.038)			
Freeman-Durden Decom	0.960 (+/- 0.015)	0.923 (+/- 0.034)	0.952 (+/- 0.022)			
Van Zyl Decom	0.960 (+/- 0.013)	0.918 (+/- 0.036)	0.955 (+/- 0.022)			

 Table A.10 Kappa Coefficients with standart deviation

Kappa: kappa. (+/- std)					
Data Type	Light GBM	SVM	RF		
Coherency Matrix	0.654 (+/- 0.023)	0.654 (+/- 0.023)	0.637 (+/- 0.027)		
Linear Polarizations	0.822 (+/- 0.033)	0.793 (+/- 0.049)	0.819 (+/- 0.040)		
Cloude-Pottier Decom	0.725 (+/- 0.053)	0.672 (+/- 0.049)	0.707 (+/- 0.049)		
Freeman-Durden Decom	0.950 (+/- 0.019)	0.904 (+/- 0.042)	0.939 (+/- 0.027)		
Van Zyl Decom	0.950 (+/- 0.016)	0.897 (+/- 0.045)	0.944 (+/- 0.027)		

 Table A.11 F-scores for Alfalfa

F-scores			
Data Type	Light GBM	SVM	RF
Coherency Matrix	0.54	0.54	0.50
Linear Polarizations	0.73	0.69	0.72
Cloude-Pottier Decom	0.62	0.57	0.58
Freeman-Durden Decom	0.90	0.81	0.88
Van Zyl Decom	0.91	0.80	0.89

**Table A.12** F-scores for Maize

F-scores			
Data Type	Light GBM	SVM	RF
Coherency Matrix	0.51	0.50	0.50
Linear Polarizations	0.72	0.68	0.71
Cloude-Pottier Decom	0.59	0.52	0.58
Freeman-Durden Decom	0.93	0.84	0.91
Van Zyl Decom	0.93	0.83	0.91

 Table A.13 F-scores for Potato

F-scores			
Data Type	Light GBM	SVM	RF
Coherency Matrix	0.83	0.83	0.81
Linear Polarizations	0.95	0.92	0.94
Cloude-Pottier Decom	0.76	0.70	0.73
Freeman-Durden Decom	0.99	0.98	0.98
Van Zyl Decom	0.99	0.98	0.99

**Table A.14** F-scores for Sunflower

F-scores			
Data Type	Light GBM	SVM	RF
Coherency Matrix	0.78	0.78	0.77
Linear Polarizations	0.92	0.91	0.92
Cloude-Pottier Decom	0.99	0.99	0.99
Freeman-Durden Decom	1.00	1.00	1.00
Van Zyl Decom	1.00	1.00	1.00

**Table A.15** F-scores for Wheat

F-scores			
Data Type	Light GBM	SVM	RF
Coherency Matrix	0.94	0.94	0.93
Linear Polarizations	0.97	0.96	0.97
Cloude-Pottier Decom	0.95	0.93	0.95
Freeman-Durden Decom	0.98	0.98	0.98
Van Zyl Decom	0.98	0.98	0.98

All comparison regarding class-based performances will be based on F-score in the following subsections.

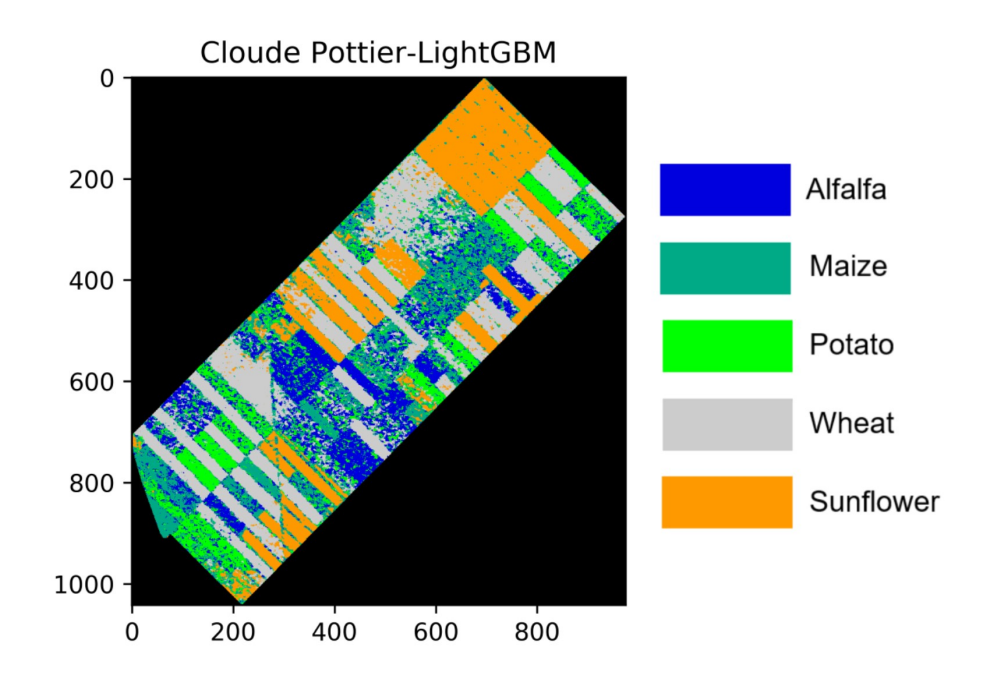


Figure B.1 Classified Image of Cloude-Pottier and LightGBM

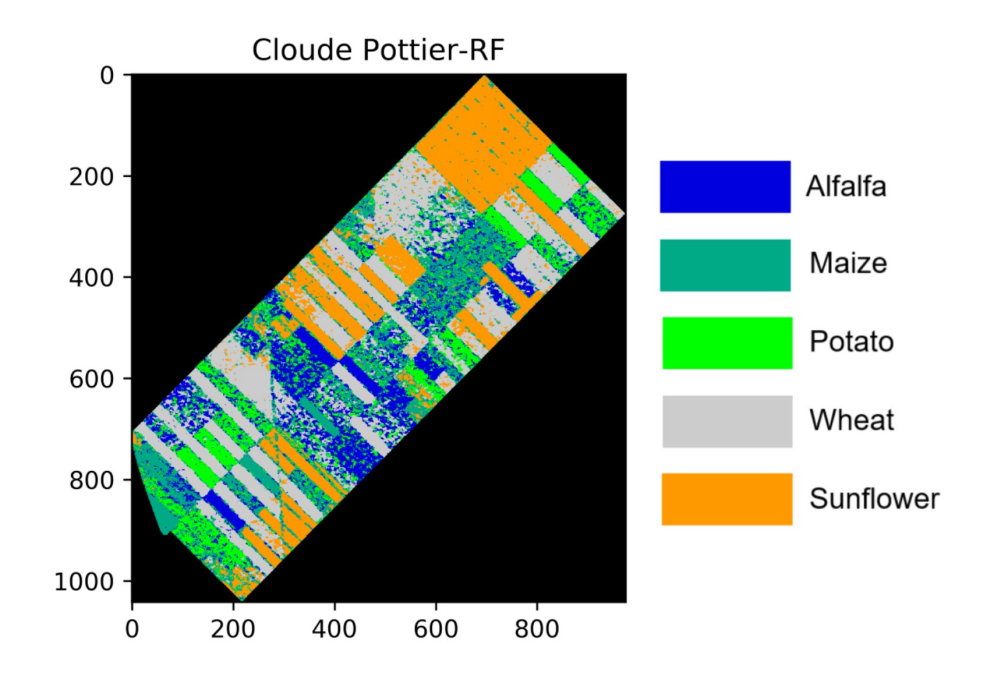


Figure B.2 Classified Image of Cloude-Pottier and RF

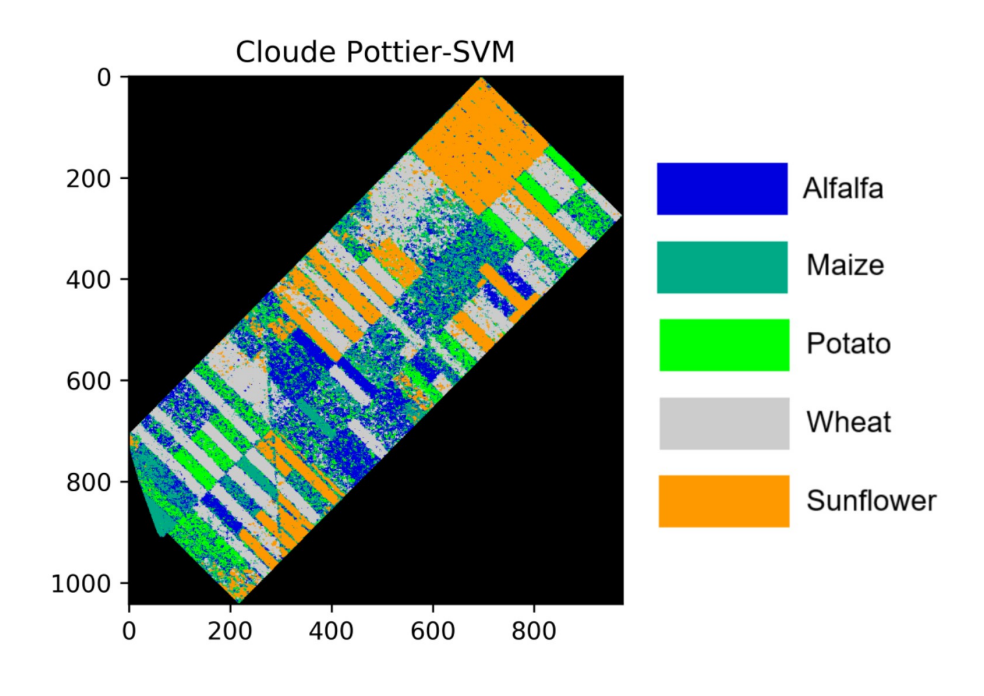


Figure B.3 Classified Image of Cloude-Pottier and SVM

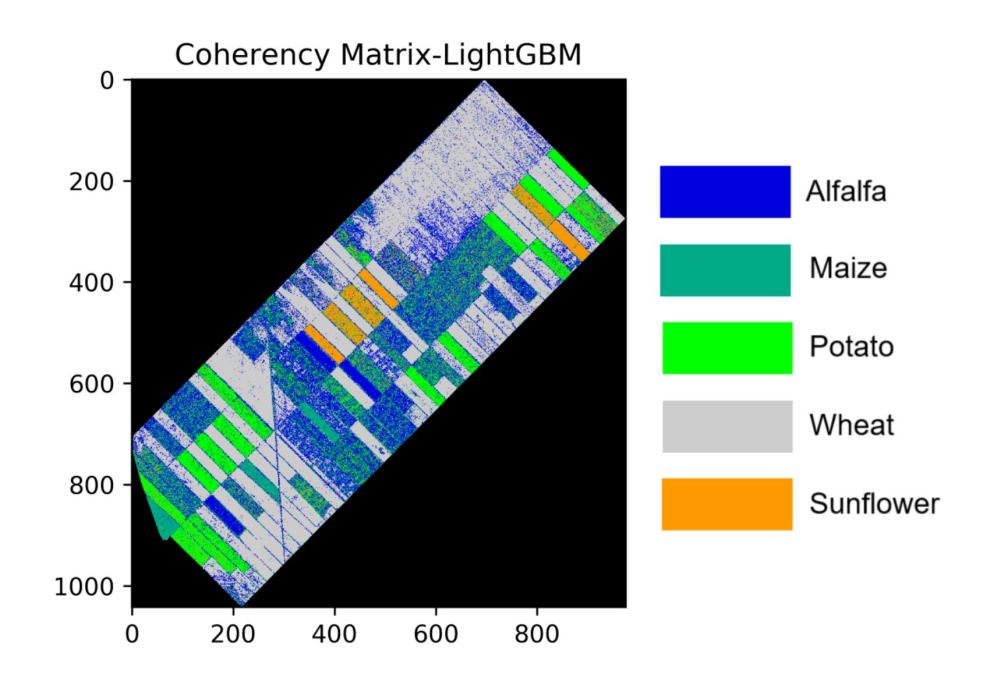


Figure B.4 Classified Image of Coherency Matrix and LightGBM

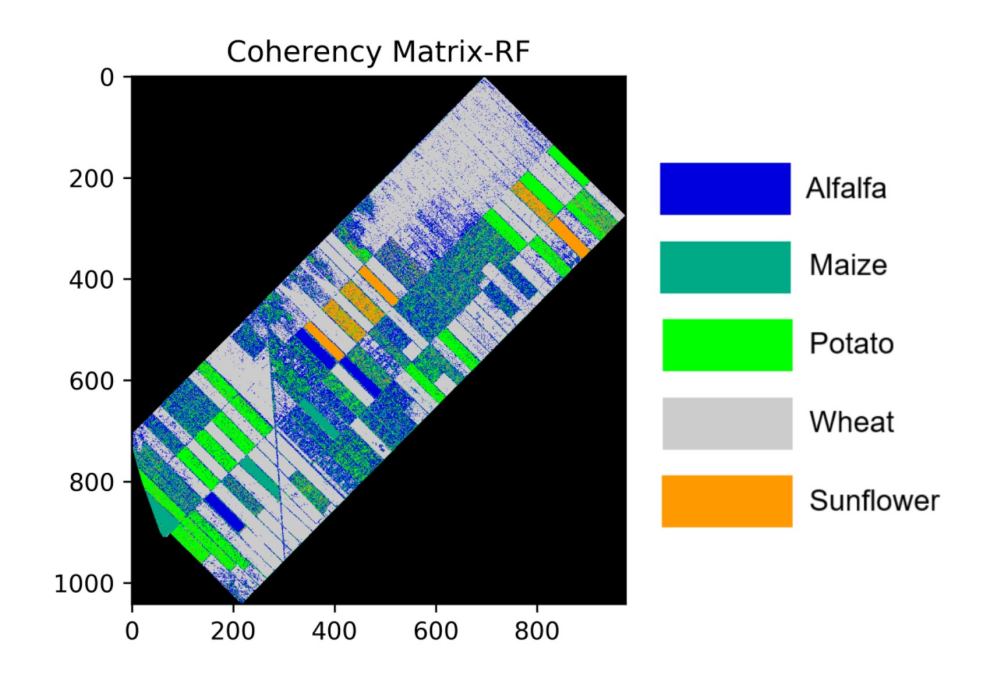


Figure B.5 Classified Image of Coherency Matrix and RF

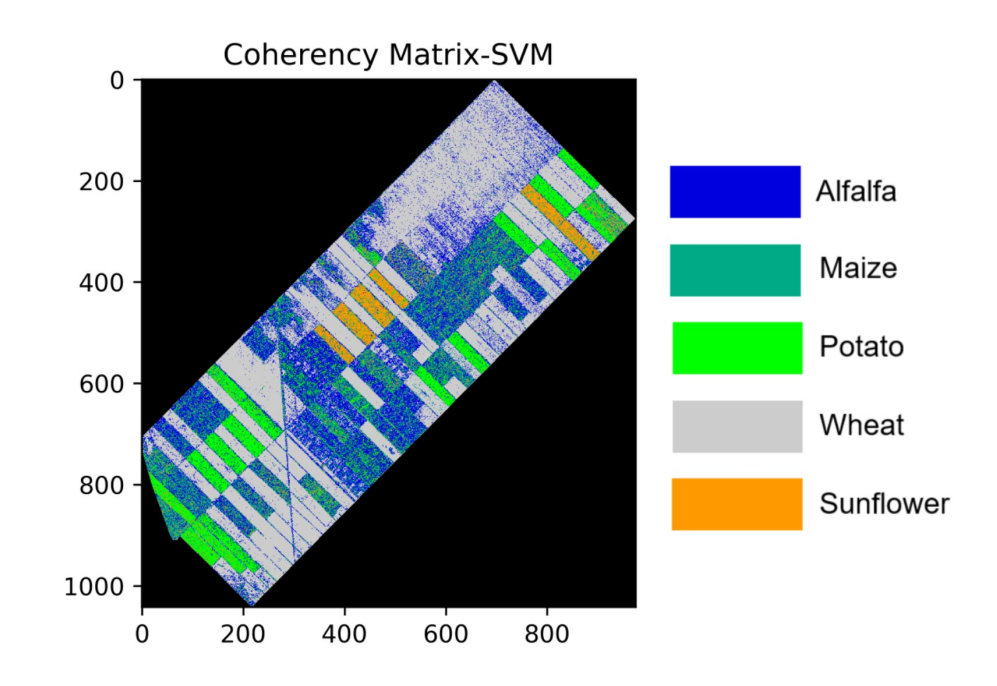


Figure B.6 Classified Image of Coherency Matrix and SVM

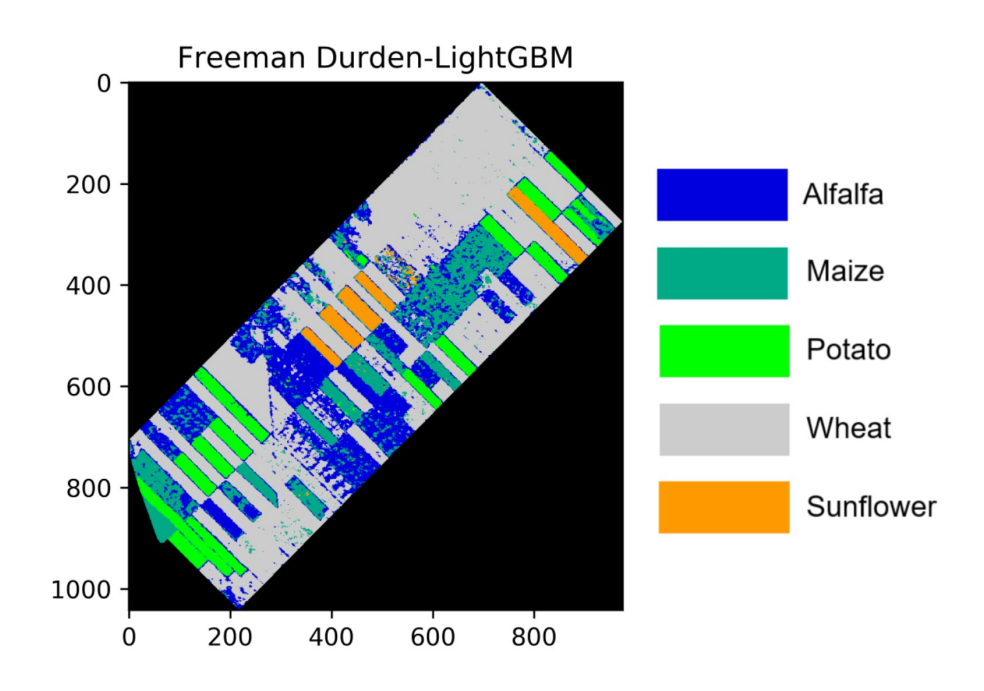


Figure B.7 Classified Image of Freeman-Durden Decomposition and LightGBM

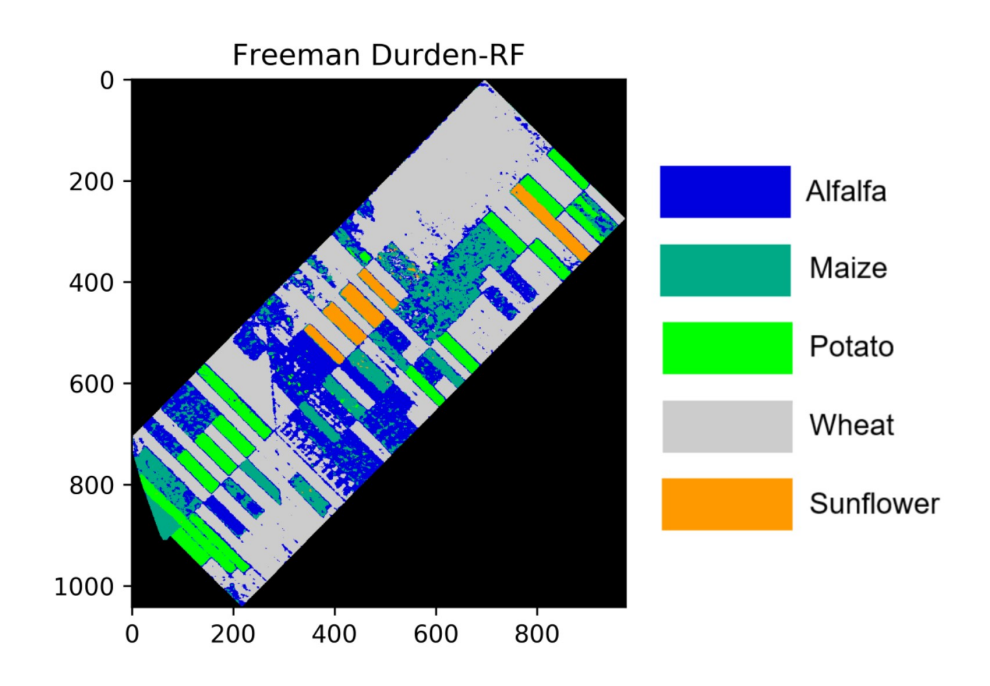


Figure B.8 Classified Image of Freeman-Durden Decomposition and RF

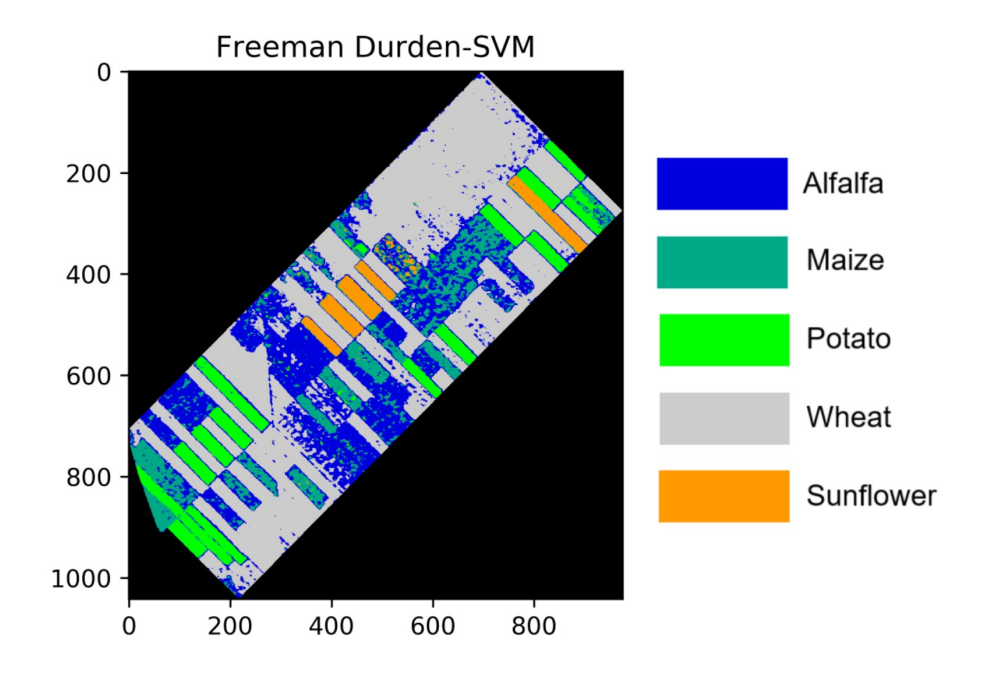


Figure B.9 Classified Image of Freeman-Durden Decomposition and SVM

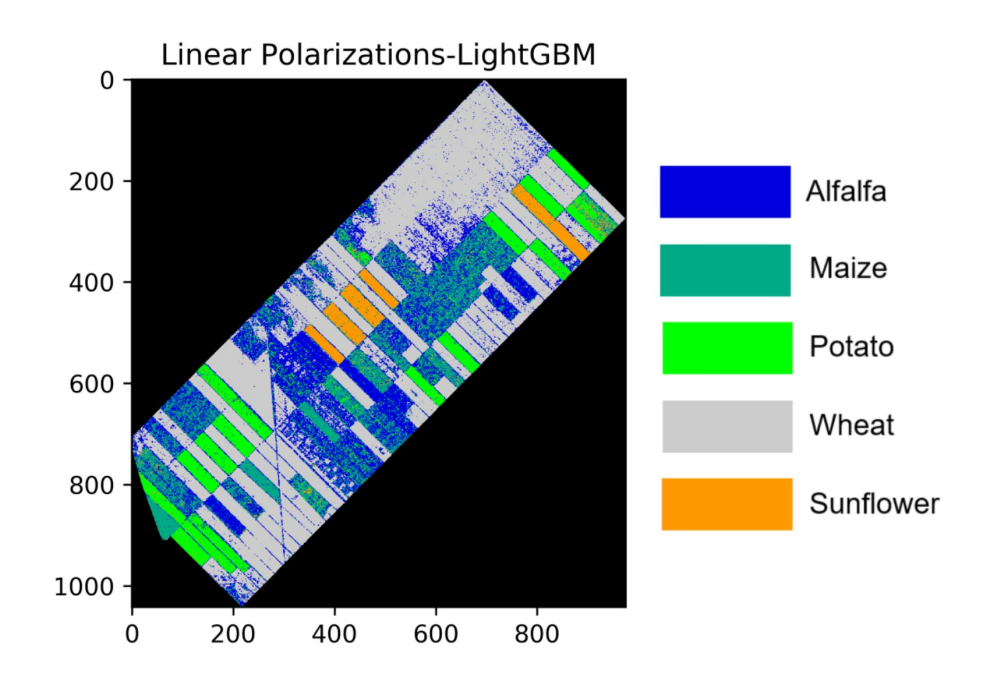


Figure B.10 Classified Image of Linear Polarizations and LightGBM

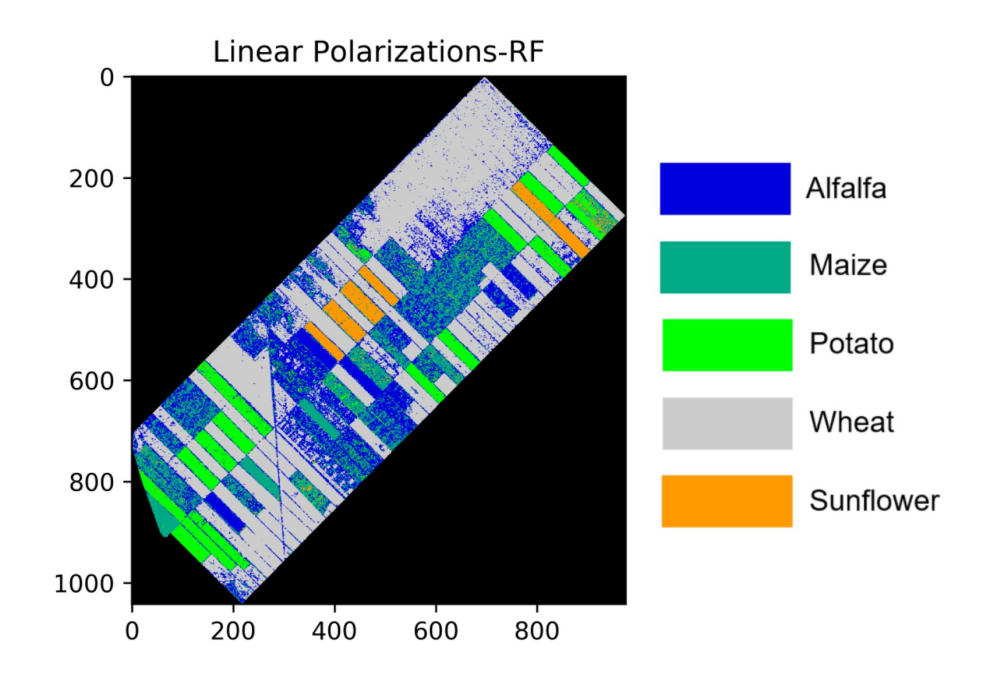


Figure B.11 Classified Image of Linear Polarizations and RF

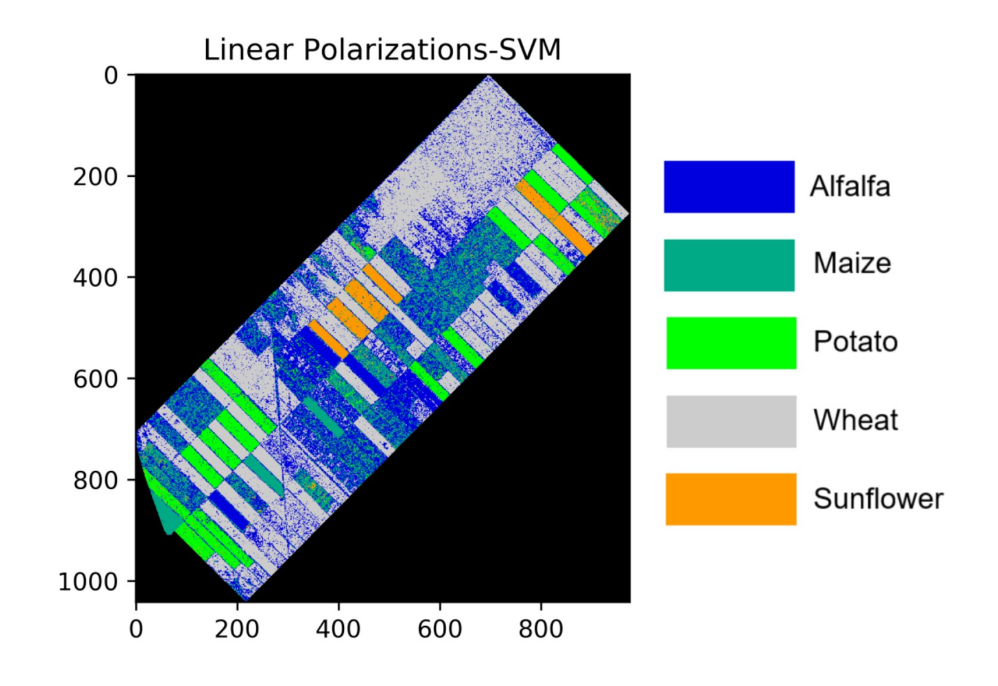


Figure B.12 Classified Image of Linear Polarizations and SVM

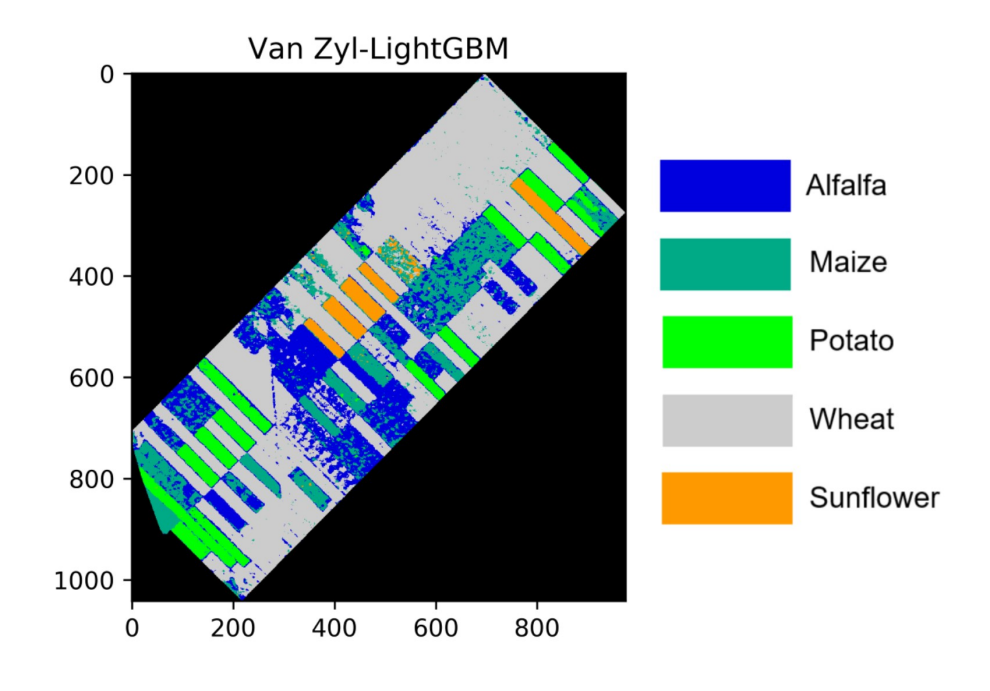


Figure B.13 Classified Image of Van Zyl Decomposition and LightGBM

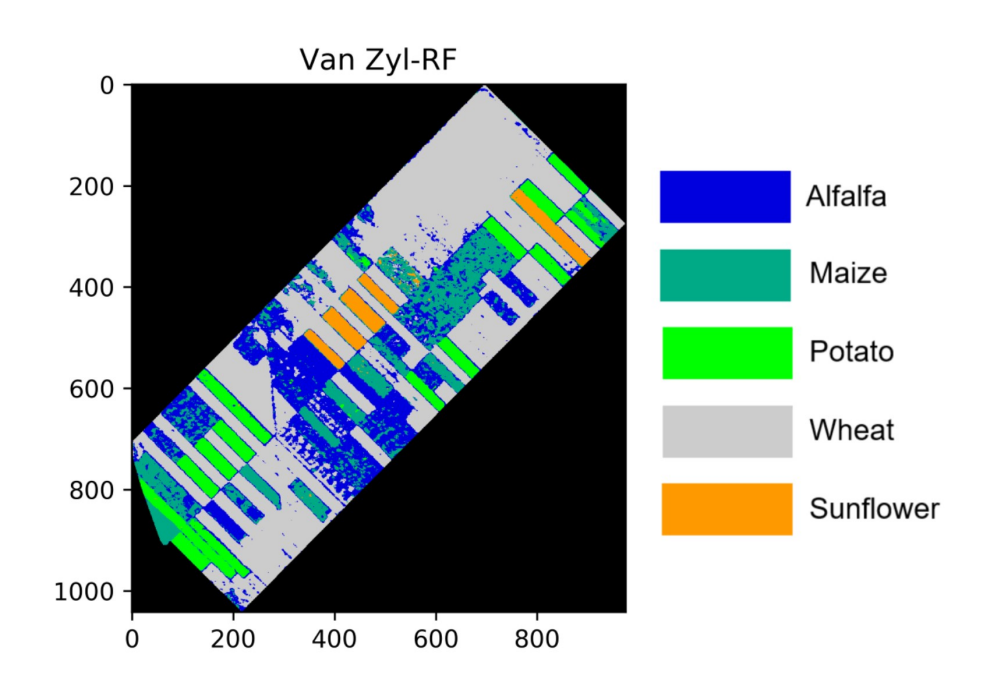


Figure B.14 Classified Image of Van Zyl Decomposition and RF

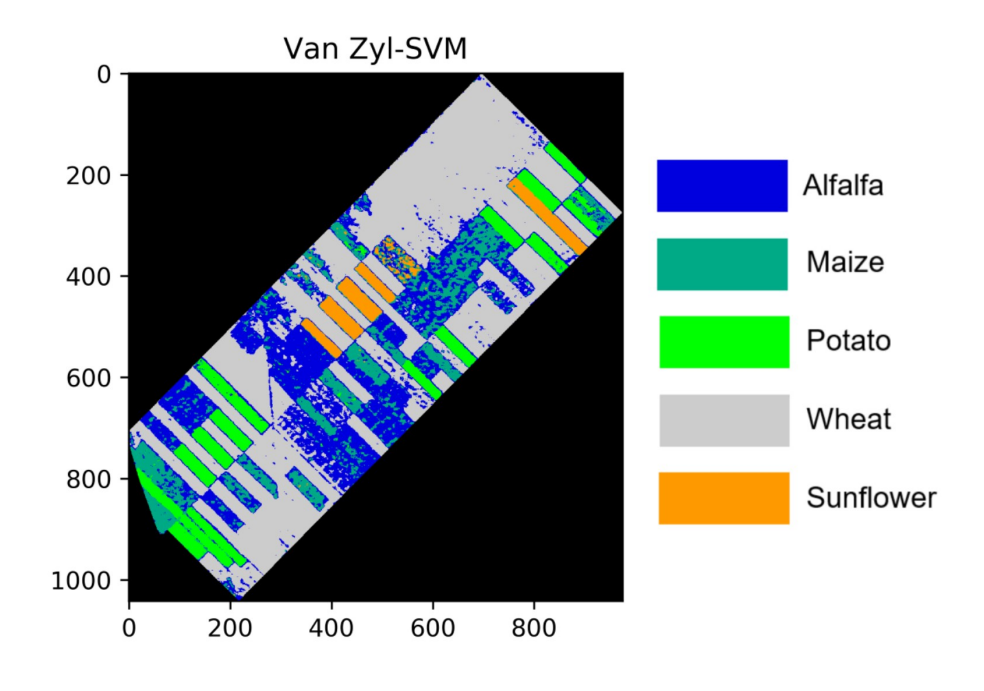


Figure B.15 Classified Image of Van Zyl Decomposition and SVM

# **Publications From the Thesis**

Contact Information: mustuner@yildiz.edu.tr

## **Papers**

- 1. **M. Ustuner** and F. Balik Sanli, "Polarimetric Target Decompositions and Light Gradient Boosting Machine for Crop Classification: A Comparative Evaluation," ISPRS International Journal of Geo-Information, vol. 8, p. 97, 2019.
- 2. **M. Ustuner** and F. Balik Sanli, "Çok zamanlı Polarimetrik SAR verileri ile tarımsal ürünlerin sınıflandırılması" Journal of Geodesy and Geoinformation, vol. x, p. 1-10, 2019.

# **Conference Papers**

- 1. **M. Ustuner** and F. Balik Sanli. "Regularized Greedy Forests for Polarimetric SAR Image Classification" In: *Abstract book of XXIX International Symposium on "Modern Technologies, Education and Professional Practice in Geodesy and Related Fields"*, Published in November, 2019. (Only abstract published)
- 2. **M. Ustuner**, F. Balik Sanli, S. Abdikan, G. Bilgin and C. Goksel. "A booster analysis of extreme gradient boosting for crop classification using PolSAR imagery" In: 8th International Conference on Agro-Geoinformatics, Agro-Geoinformatics 2019, July 16-19, 2019.
- 3. **M. Ustuner**, F. Balik Sanli, S. Abdikan, E. Erten and C. Lopez-Martinez. "Evaluating the Cloude-Pottier Decomposition for Crop Classification using Multi-Temporal Radarsat-2 Data" In: *POLinSAR 2019, 9th International Workshop on Science and Applications of SAR Polarimetry and Polarimetric Interferometry*, January 28-February 1, 2019 (Only extended abstract published)
- 4. **M. Ustuner**, F. Balik Sanli, S. Abdikan, and G. Bilgin. "An Application of Roll-invariant Polarimetric Features For Crop Classification From Multi-temporal RADARSAT-2 SAR Data" In: *Proceedings of the ISPRS TC I Midterm Symposium Innovative Sensing From Sensors to Methods and Applications*, October 10-12, 2018.